Implementacija i validacija modela propagiranja zvučnih valova

Azenić, Adam

UNIVERSITY OF ZAGREB
FACULTY OF MECHANICAL ENGINEERING AND NAVAL ARCHITECTURE

MASTER'S THESIS

Adam Azenić

Zagreb, 2016.

UNIVERSITY OF ZAGREB
FACULTY OF MECHANICAL ENGINEERING AND NAVAL ARCHITECTURE

MASTER'S THESIS

Supervisor: Student:

Prof. dr. sc. Hrvoje Jasak   Adam Azenić

Zagreb, 2016.

I hereby declare that this thesis is entirely the result of my own work except where otherwise indicated. I have fully cited all used sources and I have only used the ones given in the list of references.

SVEUČILIŠTE U ZAGREBU
FAKULTET STROJARSTVA I BRODOGRADNJE
Središnje povjerenstvo za završne i diplomske ispite
Povjerenstvo za diplomske ispite studija strojarstva za smjerove:
procesno-energetski, konstrukcijski, brodostrojarski i inženjersko modeliranje i računalne simulacije

Sveučilište u Zagrebu	
Fakultet strojarstva i brodogradnje	
Datum	Prilog
Klasa:	
Ur.broj:	

DIPLOMSKI ZADATAK

Student: **Adam Azenić**   Mat. br.: 0035184635

Naslov rada na
hrvatskom jeziku: **Implementacija i validacija modela propagiranja zvučnih valova**

Naslov rada na
engleskom jeziku: **Implementation and validation of Acoustic Wave Propagation Model**

Opis zadatka:

Problem propagacije zvučnih valova, njihove interakcije s poljem strujanja i procjena zagađenja bukom poprima sve veći značaj u inženjerskoj praksi. Standardne metode numeričke mehanike fluida nisu dovoljno točne da bi dozvolile detaljnu analizu ovog fenomena, djelomično iz razloga potrebne rezolucije proračunske mreže, a djelomično i zbog niskog nivoa tlačnog poremećaja iz kojeg proizlazi buka.

Simulacije akustičke propagacije se zato provode korištenjem lineariziranih Eulerovih jednadžbi, gdje izvor buke proizlazi iz polja strujanja ili vibracije mehaničkih komponenata, a propagacija valova se modelira lineariziranim modelom.

Kandidat će izvršiti sljedeće zadatke tokom izrade rada:

- izvršiti pregled literature vezane uz izvod i formulaciju matematičkog modela lineariziranih Eulerovih jednadžbi u proračunskoj mehanici fluida, u formulaciji koja je prikladna za simulaciju propagacije zvučnih valova;
- opisati svojstva i formulaciju izabranog modela lineariziranih Eulerovih jednadžbi, u prikladnom obliku;
- izvršiti implementaciju lineariziranih Eulerovih jednadžbi u softverskom paketu OpenFOAM;
- izvršiti validaciju implementacije na odgovarajućim primjerima s analitičkim ili referentnim numeričkim rješenjem;
- opisati i implementirati neke od metoda procjene izvora buke u turbulentnom strujanju u formi koja je prikladna za korištenje s lineariziranim modelom propagacije zvučnih valova;
- izvršiti pregled literature i opisati formulacije nereflektivnih rubnih uvjeta koji odgovaraju simulaciji propagacije zvučnih valova;
- po završenoj verifikaciji metode, izvršiti simulaciju propagacije zvučnih valova kod kanoničkih strujanja;
- opisati implementaciju i ostvarene rezultate u diplomskom radu.

U radu navesti korištenu literaturu i eventualno dobivenu pomoć.

Zadatak zadan: Rok predaje rada: Predviđeni datumi obrane:

14. siječnja 2016.   17. ožujka 2016.   23., 24. i 25. ožujka 2016.

Zadatak zadao: Predsjednica Povjerenstva:

Prof. dr. sc. Hrvoje Jasak

Prof. dr. sc. Tanja Jurčević Lulić

Contents

List of Figures

List of Tables

Nomenclature

Latin Characters

A	-	Jacobian matrix
a	m	Pulsating radius
a_0	m	Mean pulsating radius
$\hat{a}$	m	Pulsating radius amplitude
B	-	Jacobian matrix
C	-	Jacobian matrix
c	m/s	Speed of sound
c_p	J/(kg K)	Pressure-specific heat capacity
c_v	J/(kg K)	Volume-specific heat capacity
D	-	Jacobian matrix
D	m	Diameter
d	m	Diameter
$E(k)$	-	Energy spectrum
e	J/kg	Energy per unit mass
e	-	Euler number
F	-	Function which describes wave propagation in positive direction
f	Hz	Frequency
f	-	Function
f_i	N/kg	Force per unit mass
G	-	Function which describes wave propagation in negative direction
$H(f)$	-	Heaviside function
I	W/m^2	Sound intensity
I_{ref}	W/m^2	Reference sound intensity
IL	dB, Np	Sound intensity level
i	-	Imaginary unit
J_0	-	Bessel function of order 0
J_1	-	Bessel function of order 1
k	m^2/s^2	Turbulence kinetic energy

k	-	Wave number
$\mathbf{k}$	-	Wave number vector
k_η	-	Kolmogorov wave number
L_t	m	Turbulence length scale
l_j	-	Unit direction vector of the solid boundary
M	-	Mach number
$\mathbf{n}$	-	Unit vector
P	W	Sound power
P_{ij}	Pa	Compressive stress tensor
P_{ref}	W	Reference sound power
Pr	-	Prandtl number
PWL	dB, Np	Sound power level
p	Pa	Pressure
$\bar{p}$	Pa	Mean pressure
$\hat{p}'$	-	Dimensionless pressure fluctuation
p'	Pa	Sound pressure or pressure fluctuation
p_{ref}	Pa	Reference sound pressure
Q_w	W/m^3	Heat production per unit volume
q_i	W/m^2	Heat flux density
$\mathbf{R}$	-	Random vector
R	J/(kg K) or m	Specific gas constant or radius
$R_{acoustic}$	-	Reflection coefficient
Re	-	Reynolds number
r	m	Radius
SPL	dB, Np	Sound pressure level
s	J/kg	Entropy per unit mass
T	K	Thermodynamic temperature
T_{ij}	Pa	Lighthill stress tensor
t	s	Time
U_0, V_0	m/s	Artificial velocities
u	J/kg	Internal energy per unit mass

u_i, $\mathbf{v}$	m/s	Velocity
$\bar{u}_i$	m/s	Mean velocity
u'	m/s	Component of velocity fluctuation in x direction
$\hat{u}'$	-	Dimensionless x component of velocity fluctuation
V	m^3	Volume
v'	m/s	Component of velocity fluctuation in y direction
$\hat{v}'$	-	Dimensionless y component of velocity fluctuation
w'	m/s	Component of velocity fluctuation in z direction
x_i, $\mathbf{x}$	m	Position vector
x_1	m	Spatial coordinate
Δx, Δy	-	Dimensionless cell size
$\mathbf{y}$	m	Position vector

Greek Characters

$\delta_\omega(0)$	m	Shear layer thickness
δ_{ij}	-	Identity tensor
$\delta(f)$	-	Dirac delta function
γ	-	Heat capacity ratio
ε	m^2/s^3	Turbulence dissipation rate
Λ	-	Eigenvalue diagonal matrix
λ	W/(m K) or m	Conductivity or acoustic wavelength
ν	m^2/s	Kinematic viscosity
ω	rad/s	Angular frequency
ρ	kg/m^3	Density
$\bar{\rho}$	kg/m^3	Mean density
ρ'	kg/m^3	Density fluctuation
$\hat{\rho}'$	-	Dimensionless density fluctuation.
Σ_{ij}	Pa	Viscous stress tensor
σ_{ji}	Pa	Stress tensor
θ	rad	Angle

Superscripts

p'	Fluctuation quantity
$\bar{p}$	Mean quantity
$\hat{p}$	Dimensionless quantity.

Subscripts

x_i, x_j	Vector
Σ_{ij}	Tensor
p_0	Value at atmospheric conditions
p_{ref}	Reference value

Abbreviations

APE - Acoustic Perturbation Equations

CAA - Computational Aeroacoustics

CCM - Computational Continuum Mechnics

CFD - Computation Fluid Dynamics

DES - Detached Eddy Simulation

DMF - test case with Diagonal Mean Flow

DNS - Direct Numerical Simulation

FVM - Finite Volume Method

FW-H - Ffowcs Williams-Hawkings

HMF - test case with Horizontal Mean Flow

LEE - Linearised Euler Equations

LES - Large Eddy Simulation

PML - Perfectly Matched Layer

PCE - Perturbation Compressible Equations

RANS - Reynolds-Averaged Navier-Stokes equations

RW - test case with Reflective Wall

SATIN - Statistical Approach to Turbulence-Induced Noise

SNGR - Stochastic Noise Generation and Radiation

URANS - Unsteady Reynolds-Averaged Navier-Stokes equations

Abstract

Noise pollution negatively influences the quality of people's lives and the consequences on the health are often significant. Therefore, the problem of predicting the sound sources and propagation of acoustic waves is an everyday growing issue that the engineers and scientists encounter.

In this thesis the implementation, verification and validation of the Linearised Euler Equations (LEE), which govern the acoustic wave propagation, have been conducted. The LEEs have been implemented as a stand-alone solver, using OpenFOAM-extend C++ libraries. The system of LEEs has been discretised by using the conservative Finite Volume Method (FVM). Verification and validation of the solver have been carried out with three test cases, comparing the results with analytical solutions. The grid convergence study for the validation test cases has been carried out. The simplified method for the sound source prediction using RANS predicted turbulence data has been implemented and tested on the simulation of noise generated by 2D mixing layer.

Results have shown that the solutions obtained with the LEE solver converge towards the analytical solutions. Simulation of acoustic wave reflection off a wall has shown that the numerical predictions of the reflected and non-reflected wave give solutions of practically the same accuracy. Results for later time instants contain spurious waves, reflected off the open boundaries, due to inadequate boundary condition used in simulations.

It can be concluded that the implementation of sound propagation method has been successfully conducted, as evidenced by the results of three test cases. It is shown that the propagation of acoustic waves in an uniform mean flow can accurately be computed with the implemented solver. The method for the sound source generation needs improvements, what together with the implementation of a non-reflecting boundary condition remains a task for future research.

Key words: Linearised Euler Equations, acoustic wave propagation, OpenFOAM-extend, Finite Volume Method

Sažetak

Zagađenje bukom negativno utječe na živote ljudi te su posljedice utjecaja buke na njihovo zdravlje često značajne. Zbog toga je predviđanje izvora zvuka te propagacije zvučnih valova sve aktualnija tema inženjera i znanstvenika.

U ovome je radu provedena implementacija, verifikacija i validacija lineariziranih Eulerovih jednadžbi (eng. *Linearised Euler Equations*, skraćeno LEE), koje matematički opisuju propagaciju zvučnih valova. LEE su implementirane u jedinstveni rješavač (eng. *solver*), koristeći programski paket OpenFOAM-extend. Jednadžbe su riješene koristeći metodu kontrolnih volumena (eng. *Finite Volume Method*, skraćeno FVM). Verifikacija i validacija rješavača provedene su putem tri validacijska slučaja, uspoređujući s analitičkim rješenjima. Provedena je i studija kovergencija mreža kontrolnih volumena. Implementirana je pojednostavljena metoda za određivanje izvora zvuka koristeći podatke turbulencije iz RANS simulacije te je testirana na simulaciji dvodimenzionalnog vrtložnog sloja.

Rezultati su pokazali da rješenja dobivena LEE rješavačem konvergiraju prema analitičkim rješenjima. Simulacija odbijanja zvučnog vala od zida pokazala je da numerički proračuni reflektiranog i nereflektiranog vala daju rješenja praktički jednake točnosti. Rezultati kasnijih vremenskih trenutaka sadrže kontaminirajuće valove koji su reflektirani od otvorenih granica domene proračuna zbog neadekvatih rubnih uvjeta korištenih u simulacijama.

Može se zaključiti da je implementacija metode za propagaciju zvučnih valova uspješno provedena, što dokazuju rezultati tri validacijska slučaja. Pokazano je da se propagacija akustičnih valova u homegenom srednjem strujanju može s dovoljnom točnošću predvijeti koristeći implementirani rješavač. Metodu za generiranje izvora zvuka treba poboljšati, što zajedno s implementacijom nereflektirajućih rubnih uvjeta ostaje zadatak za buduća istraživanja.

Ključne riječi: linearizirane Eulerove jednadžbe, propagacija akustičnih valova, OpenFOAM-extend, metoda kontrolnih volumena

Prošireni sažetak

Zagađenje bukom negativno utječe na živote ljudi te su posljedice utjecaja buke na njihovo zdravlje često značajne. Primjerice, djelomičan ili potpun gubitak sluha te psihičke reakcije, poput povećanog krvnog tlaka, su česte pojave u slučaju dugotrajne izloženosti glasnim zvukovima. Zbog toga je predviđanje izvora zvuka te propagacije zvučnih valova sve aktualnija tema inženjera i znanstvenika.

Uvod u računalnu aeroakustiku

Ubrzanim razvojem računala u posljednjih nekoliko desetljeća je upotreba numeričkih metoda proračuna postala moguća. Tako je i primjena računalnih metoda u predviđanju izvora zvuka i propagiranju zvučnih valova, odnosno računalna aeroakustika (eng. *Computational Aeroacoustics*, skraćeno CAA) postala sve zastupljenija među znanstvenim djelatnostima. Današnji je koncept računalne aeroakustike temeljen na istraživanjima Sir Jamesa Lighthilla [3], početkom 1950-ih godina. On je predstavio zvuk kao razliku između stvarnog i osrednjenog toka fluida. J. E. Ffowcs Williams i D. L. Hawkings [4] su kasnije proširili Lighthillovu akustičnu teoriju na slučaj gibajućih površina koje se nalaze u fluidu.

Danas postoje različiti pristupi rješavanja problema računalne aeroakustike. Najizravniji pristup je direktna metoda, koja ne uključuje bilo kakvo modeliranje zvuka te se zbog toga ne javljaju problemi pogrešaka modeliranja. Glavni problem upotrebe direktnih metoda je potreba za vrlo velikim računalnim resursima što je u inženjeskoj primjeni neisplativo. Drugi pristup, danas najčešće korišten u CAA, je upotreba hibridnih metoda, koje su karakterizirane odvojenosti metode generiranja izvora zvuka od metode transporta, odnosno propagacije zvuka.

Matematičke i fizikalne osnove

U ovome je radu izvršena implementacija, verifikacija i validacija lineariziranih Eulerovih jednadžbi (eng. *Linearised Euler Equations*, skraćeno LEE), koje matematički opisuju propagiranje zvučnih valova. LEE su implementirane u rješavač (eng. solver), koristeći programski paket OpenFOAM-extend, napisan u C++ programskom jeziku. Izvod počinje od Navier-Stokesovih jedndžbi zanemarivanjem svih viskoznih članova, čime se dobivaju Eulerove jednadžbe, koje zapisane u konzervativnoj formi glase:

$$\frac{\partial \rho}{\partial t} + \frac{\partial (\rho u_j)}{\partial x_j} = 0, \tag{1}$$

$$\frac{\partial(\rho u_i)}{\partial t} + \frac{\partial(\rho u_i u_j + p\delta_{ij})}{\partial x_j} = 0, \qquad (2)$$

$$\frac{\partial(\rho e + \frac{1}{2}\rho u_i u_i)}{\partial t} + \frac{\partial(\rho e u_j + \frac{1}{2}\rho u_i u_i u_j + p u_j)}{\partial x_j} = 0, \qquad (3)$$

gdje ρ predstavlja gustoću, t vrijeme, u_j vektor brzine, x_j radij-vektor položaja, δ_{ij} Kronecke-rov delta simbol, e specifičnu unutarnju energiju te p hidrostatski tlak. Jednadžbe (1), (2) te (3) predstavljaju redom jednadžbe kozervacije mase, količine gibanja i energije.

Iz jednadžbe (3) se uvođenjem jednadžbe idealnog plina

$$p = \rho RT, \qquad (4)$$

gdje R predstavlja specifičnu plinsku konstantu, a T apsolutnu temperaturu, dobiva sljedeća jednadžba, izražena preko tlaka p glasi

$$\frac{\partial p}{\partial t} + \frac{\partial(pu_j + \gamma p u_j)}{\partial x_j} - p\frac{\partial u_j}{\partial x_j} - \gamma u_j \frac{\partial p}{\partial x_j} = 0, \qquad (5)$$

gdje γ označava izentropski eksponent.

Linearizacija jednadžbi (1), (2) i (5) počinje razlaganjem polja na osrednjeni i fluktuirajući (akustični) dio:

$$\begin{aligned}
\rho &= \bar{\rho} + \rho', \\
u_i &= \bar{u}_i + u_i', \\
p &= \bar{p} + p',
\end{aligned} \qquad (6)$$

gdje ρ', u_i' te p' redom predstavljaju fluktuirajuću gustoću, fluktuirajuću brzinu i fluktuirajući tlak, dok $\bar{\rho}$, $\bar{u}_i$ i $\bar{p}$ predstavljaju osrednjenu gustoću, brzinu i tlak.

Fluktuirajuće varijable predstavljaju poremećaje u osrednjenom toku fluida koje ljudsko uho registrira kao zvuk. Za male Machove brojeve strujanja fluida, fluktuirajuća akustična polja su za višestruke redove veličina manja od njihovih osrednjenih polja [1]. Primjerice, u slučaju Machovog broja $M = 0.1$, odnos snage zvuka i mehaničke snage koja ga uzrokuje je 10^{-9}, dok za slučaj putničkog zrakoplova ($M = 0.7$) odnos raste na tek 10^{-5}.

Uvrštavanjem jednadžbi (6) u jednadžbe (1), (2) i (5) dobivaju se globalne jednadžbe:

$$\frac{\partial \bar{\rho}}{\partial t} + \frac{\partial \rho'}{\partial t} + \frac{\partial}{\partial x_j}\left(\bar{\rho}\bar{u}_j + \bar{\rho}u_j' + \rho'\bar{u}_j + \rho'u_j'\right) = 0, \qquad (7)$$

$$\frac{\partial(\bar{\rho}\bar{u}_i)}{\partial t} + \frac{\partial(\bar{\rho}u_i')}{\partial t} + \frac{\partial(\rho'\bar{u}_i)}{\partial t} + \frac{\partial(\rho'u_i')}{\partial t} +$$

$$\frac{\partial}{\partial x_j}\left(\bar{\rho}\bar{u}_i\bar{u}_j + \bar{\rho}\bar{u}_i u_j' + \bar{\rho}u_i'\bar{u}_j + \bar{\rho}u_i'u_j' + \rho'\bar{u}_i\bar{u}_j + \rho'\bar{u}_i u_j' + \rho'u_i'\bar{u}_j + \rho'u_i'u_j' + \bar{p}\delta_{ij} + p'\delta_{ij}\right) = 0,$$

$$\tag{8}$$

$$\frac{\partial p'}{\partial t} + \frac{\partial}{\partial x_j}\left(p'\bar{u}_j + \bar{p}u_j' + \gamma\bar{p}u_j' + \gamma p'\bar{u}_j\right) - p'\frac{\partial \bar{u}_j}{\partial x_j} - \bar{p}\frac{\partial u_j'}{\partial x_j} - \gamma\bar{u}_j\frac{\partial p'}{\partial x_j} - \gamma u_j'\frac{\partial \bar{p}}{\partial x_j} = 0, \quad \tag{9}$$

gdje se mogu identificirati dva podskupa jednadžbi: osrednjene, koje sadrže samo osrednjene variable te akustične, koje sadrže samo fluktuirajuće članove, odnosno članove s jednom ili više fluktuirajućih varijabli. Ukoliko član sadrži jednu fluktuirajuću varijablu, to je fluktuirajući član prvog reda, ukoliko sadrži dvije, onda je drugog reda, itd. Kako bi se izolirale akustične jednadžbe, potrebno je oduzeti osrednjene od globalnih. Akustične jednadžbe su u tom obliku nelinearne jer sadrže fluktuirajuće članove različitih redova veličina. Uzimajući u obzir spomenute odnose fluktuirajućih i osrednjenih veličina, dozvoljeno je uvesti aproksimaciju u nelinearne akustične jednadžbe na način da se zanemaruju članovi drugog i višeg reda, jer su zanemarivi u odnosu na članove prvog reda. Opisana aproksimacija se zove *linearizacija*. Nakon linearizacije, dobivaju se linearizirane Eulerove jednadžbe, koje glase:

$$\frac{\partial \rho'}{\partial t} + \frac{\partial}{\partial x_j}\left(\bar{\rho}u_j' + \rho'\bar{u}_j\right) = 0, \tag{10}$$

$$\frac{\partial \bar{\rho}u_i'}{\partial t} + \frac{\partial}{\partial x_j}\left(\bar{\rho}\bar{u}_j u_i' + p'\delta_{ij}\right) + \underline{\left(\bar{\rho}u_j' + \rho'\bar{u}_j\right)\frac{\partial \bar{u}_i}{\partial x_j}} = 0, \tag{11}$$

$$\frac{\partial p'}{\partial t} + \frac{\partial}{\partial x_j}\left(p'\bar{u}_j + \gamma\bar{p}u_j'\right) + (\gamma - 1)\left(\underline{p'\frac{\partial \bar{u}_j}{\partial x_j} - u_j'\frac{\partial \bar{p}}{\partial x_j}}\right) = 0. \tag{12}$$

U sustavu lineariziranih Eulerovih jednadžbi (10), (11) i (12), podcrtani članovi sadrže prostorne derivacije osrednjenih veličina te su jednaki nuli, ukoliko je srednji tok homogen. Jednadžbe (10), (11) i (12) su implementirane u rješavač, čija je verifikacija i validacija prikazana u daljnjem tekstu.

Verifikacija i validacija

Metoda kontrolnih volumena (eng. *Finite Volume Method*, skraćeno FVM), implementirana u programskom paketu OpenFOAM-extend, korištena je za diskretizaciju lineariziranih Eulerovih jednadžbi.

Validacijski slučajevi korišteni u ovom radu su preuzeti iz [2], gdje se nalaze pod imenima Problem 1 i 2 u Kategoriji 3 te Problem 1 u Kategoriji 4. Zbog jednostavnosti prepoznavanja,

u ovome se radu validacijski slučajevi zovu slučaj s horizontalnim srednjim strujanjem, slučaj s dijagonalnim srednjim strujanjem i slučaj s reflektirajućim zidom.

Slučajevi s horizontalnim i dijagonalnim srednjim strujanjem

Validacijski slučajevi s horizontalnim i dijagonalnim srednjim strujanjem služe kako bi se testirali radijativni rubni uvjeti, propagacija zvučnog vala kroz domenu te izotropna svojstva računalnog algoritma. Koriste se bezdimenzijske varijable sa sljedećim skalama:

- Δx = skala duljine*,

- c_∞ (brzina zvuka) = skala brzine,

- $\frac{\Delta x}{a_\infty}$ = skala vremena,

- ρ_∞ = skala gustoće i

- $\rho_\infty a_\infty^2$ = skala tlaka.

Skala duljine je definirana duljinom ćelije najgrublje mreže, s 40 000 volumena.

Računalna domena je definirana s $-100 \leqslant x \leqslant 100$, $-100 \leqslant y \leqslant 100$ te se nalazi u slobodnom prostoru (vidi sliku 1).

Slučaj s horizontalnim srednjim strujanjem

Za zadane $M_x = 0.5$ i $M_y = 0$ treba riješiti problem početnih vrijednosti. Inicijalna polja bezdimenzijskih varijebli, fluktuacije tlaka $\hat{p}'$, gustoće $\hat{\rho}'$ i komponenti brzine $\hat{u}'$ i $\hat{v}'$, dana su u vremenu $\hat{t} = 0$ putem sljedećih jednadžbi:

$$\hat{p}' = \exp\left[-(\ln 2)\left(\frac{x^2 + y^2}{9}\right)\right], \tag{13}$$

$$\hat{\rho}' = \exp\left[-(\ln 2)\left(\frac{x^2 + y^2}{9}\right)\right] + 0.1 \exp\left[-(\ln 2)\left(\frac{(x-67)^2 + y^2}{25}\right)\right], \tag{14}$$

$$\hat{u}' = 0.04y \exp\left[-(\ln 2)\left(\frac{(x-67)^2 + y^2}{25}\right)\right], \tag{15}$$

$$\hat{v}' = -0.04(x-67) \exp\left[-(\ln 2)\left(\frac{(x-67)^2 + y^2}{25}\right)\right]. \tag{16}$$

Analitičko rješenje slučaja s horizontalnim srednjim strujanjem

Neka su $\alpha_1 = \frac{\ln 2}{9}$, $\alpha_2 = \frac{\ln 2}{25}$, $M = 0.5$ i $\eta = \left[(x-Mt)^2 + y^2\right]^{1/2}$. Analitička rješenja su definirana sljedećim jednadžbama:

$$\hat{u}' = \frac{x-Mt}{2\alpha_1 \eta} \int_0^\infty e^{\frac{-\xi^2}{4\alpha_1}} \sin(\xi t) J_1(\xi\eta)\xi d\xi + 0.04 y e^{-\alpha_2\left[(x-67-Mt)^2+y^2\right]}, \tag{17}$$

$$\hat{v}' = \frac{y}{2\alpha_1 \eta} \int_0^\infty e^{\frac{-\xi^2}{4\alpha_1}} \sin(\xi t) J_1(\xi\eta)\xi d\xi - 0.04(x-67-Mt) e^{-\alpha_2\left[(x-67-Mt)^2+y^2\right]}, \tag{18}$$

$$\hat{p}' = \frac{1}{2\alpha_1} \int_0^\infty e^{\frac{-\xi^2}{4\alpha_1}} \cos(\xi t) J_0(\xi\eta)\eta d\eta, \tag{19}$$

$$\hat{\rho}' = \hat{p}' + 0.1 e^{-\alpha_2\left[(x-67-Mt)^2+y^2\right]}, \tag{20}$$

gdje su $J_0(...)$ i $J_1(...)$ Besselove funkcije nultog i prvog reda.

Slučaj s dijagonalnim srednjim strujanjem

Za zadane $M_x = M_y = 0.5\cos\left(\frac{\pi}{4}\right)$ treba riješiti problem početnih vrijednosti. Inicijalna polja bezdimenzijskih varijabli $\hat{p}'$, $\hat{\rho}'$, $\hat{u}'$ i $\hat{v}'$ dana su u vremenu $\hat{t} = 0$ putem jednadžbi:

$$\hat{p}' = \exp\left[-(\ln 2)\left(\frac{x^2+y^2}{9}\right)\right], \tag{21}$$

$$\hat{\rho}' = \exp\left[-(\ln 2)\left(\frac{x^2+y^2}{9}\right)\right] + 0.1\exp\left[-(\ln 2)\left(\frac{(x-67)^2+(y-67)^2}{25}\right)\right], \tag{22}$$

$$\hat{u}' = 0.04(y-67)\exp\left[-(\ln 2)\left(\frac{(x-67)^2+(y-67)^2}{25}\right)\right], \tag{23}$$

$$\hat{v}' = -0.04(x-67)\exp\left[-(\ln 2)\left(\frac{(x-67)^2+(y-67)^2}{25}\right)\right]. \tag{24}$$

Iz jednadžbi (21) do (24) se može primjetiti da je osrednjeni tok usmjeren dijagonalno od proračunske domene.

Analitičko rješenje slučaja s dijagonalnim srednjim strujanjem

Neka su $\alpha_1 = \frac{\ln 2}{9}$, $\alpha_2 = \frac{\ln 2}{25}$, $M_x = M_y = 0.5\cos\left(\frac{\pi}{4}\right)$ i $\eta = \left[(x-M_x t)^2 + (y-M_y t)^2\right]^{1/2}$. Ana-

litička rješenja su dana putem sljedećih jednadžbi:

$$\hat{u}' = \frac{x - M_x t}{2\alpha_1 \eta} \int_0^\infty e^{\frac{-\xi^2}{4\alpha_1}} \sin(\xi t) J_1(\xi \eta) \xi d\xi + 0.04(y - M_y t)e^{-\alpha_2\left[(x-67-M_x t)^2 + (y-67-M_y t)^2\right]}, \quad (25)$$

$$\hat{v}' = \frac{y - m_y t}{2\alpha_1 \eta} \int_0^\infty e^{\frac{-\xi^2}{4\alpha_1}} \sin(\xi t) J_1(\xi \eta) \xi d\xi - 0.04(x - 67 - M_x t)e^{-\alpha_2\left[(x-67-M_x t)^2 + (y-67-M_y t)^2\right]},$$

$$(26)$$

$$\hat{p}' = \frac{1}{2\alpha_1} \int_0^\infty e^{\frac{-\xi^2}{4\alpha_1}} \cos(\xi t) J_0(\xi \eta) \eta d\eta, \qquad (27)$$

$$\hat{\rho}' = p + 0.1 e^{-\alpha_2\left[(x-67-M_x t)^2 + (y-67-M_y t)^2\right]}, \qquad (28)$$

gdje su $J_0(...)$ i $J_1(...)$ Besselove funkcije nultog i prvog reda.

U jednadžbama (13) do (16) te (21) do (24) se mogu prepoznati tri inicijalna pulsa: akustični, entropijski i vrtložni [18]. Akustični se puls sastoji od fluktuacija tlaka i gustoće (jednadžba (13) i prvi član jednadžbe (14)), entropijski puls od fluktuacije gustoće (drugi član u jednadžbi (14)), dok se vrtložni puls sastoji od fluktuacija brzine (jednadžbe (15) i (16)).

Slika 1 prikazuje polja $\hat{\rho}'$ za validacijske slučajeve s horizontalnim i dijagonalnim srednjim strujanjem, gdje su vidljivi samo akustični i entropijski puls. Vrtložni puls se ne vidi jer se ne sastoji od fluktuacije gustoće $\hat{\rho}'$.
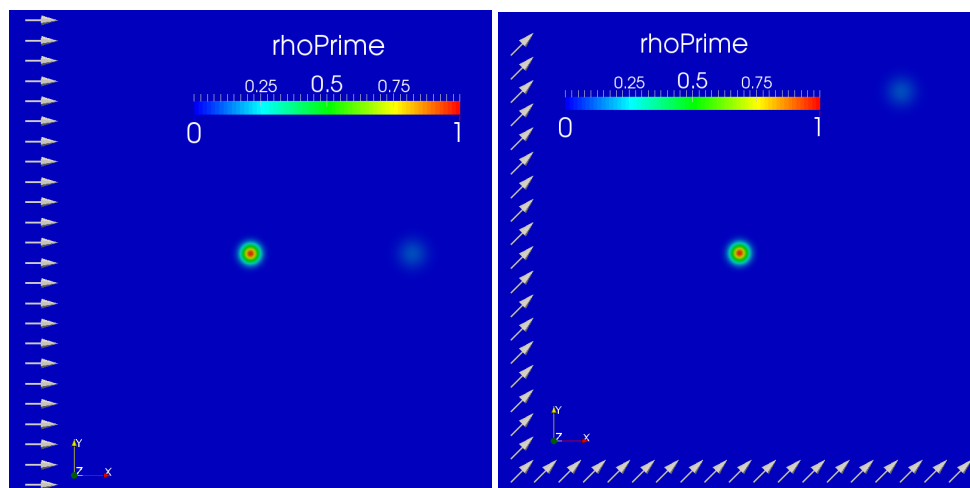
Slika 1: Inicijalno polje $\hat{\rho}'$ za validacijske slučajeve s horizontalnim srednjim strujanjem (lijevo) i s dijagonalnim srednjim strujanjem (desno); strelice pokazuju smjer osrednjenog polja brzine $\bar{u}$.

Slučaj s reflektirajućim zidom

Validacijski slučaj s reflektirajućim zidom je konstruiran u svrhu ispitivanja efektivnosti rubnog uvjeta zida za slučaj refleksije akustičkog vala te se koriste iste bezdimenzijske varijable kao i u prethodnim slučajevima. Slučaj s reflektirajućim zidom daje refleksiju akustičkog vala od zida u prisustvu homogenog osrednjenog toka fluida u polu-beskonačnom prostoru.

Proračunska domena je definirana s $-100 \leqslant x \leqslant 100$, $0 \leqslant y \leq 200$. Zid se nalazi na $y = 0$ (vidi sliku 2). Početni uvjet za $\hat{t} = 0$ je definiran putem jednadžbi:

$$\hat{u}' = \hat{v}' = 0, \tag{29}$$

$$\hat{p}' = \hat{\rho}' = \exp\left\{-(\ln 2)\left[\frac{x^2 + (y-25)^2}{25}\right]\right\}. \tag{30}$$
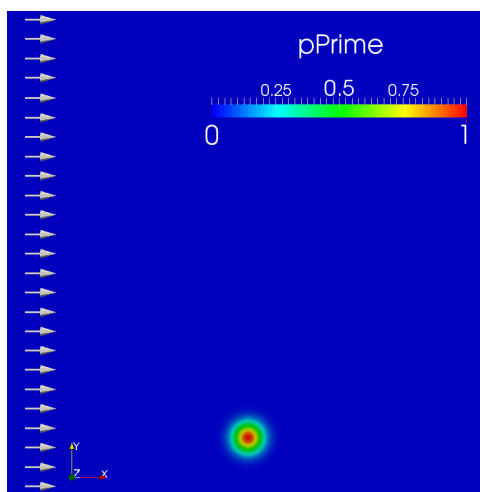
Slika 2: Inicijalno polje bezdimenzijske fluktuacije tlaka $\hat{p}'$ za validacijski slučaj s reflektirajućim zidom. Strelice pokazuju smjer osrednjenog toka $\bar{u}$. Donja granica označava zid.

Analitičko rješenje slučaja s reflektirajućim zidom

Sa $\alpha = \frac{\ln 2}{25}$, $\eta = \left[(x - Mt)^2 + (y - 25)^2\right]^{1/2}$ i $\zeta = \left[(x - Mt)^2 + (y + 25)^2\right]^{1/2}$ analitičko rješenje slučaja s reflektirajućim zidom je dano u sljedećoj formi [2]:

$$\hat{u}' = \frac{x - Mt}{2\alpha\eta}\int_0^\infty e^{-\frac{\xi^2}{4\alpha}}\sin(\xi t)J_1(\xi\eta)\xi d\xi + \frac{x - Mt}{2\alpha\zeta}\int_0^\infty e^{-\frac{\xi^2}{4\alpha}}\sin(\xi t)J_1(\xi\zeta)\xi d\xi, \tag{31}$$

$$\hat{v}' = \frac{y - 25}{2\alpha\eta}\int_0^\infty e^{-\frac{\xi^2}{4\alpha}}\sin(\xi t)J_1(\xi\eta)\xi d\xi + \frac{y + 25}{2\alpha\zeta}\int_0^\infty e^{-\frac{\xi^2}{4\alpha}}\sin(\xi t)J_1(\xi\zeta)\xi d\xi, \tag{32}$$

$$\hat{p}' = \hat{\rho}' = \frac{1}{2\alpha}\int_0^\infty e^{-\frac{\xi^2}{4\alpha}}\cos(\xi t)\left[J_0(\xi\eta) + J_0(\xi\zeta)\right]\xi d\xi. \tag{33}$$

Autor je primjetio da je faktor $\frac{y+25}{2\alpha\zeta}$ u jednadžbi (32) pogrešno napisan u [2] te glasi $\frac{y-25}{2\alpha\zeta}$.

Studija kovergencija mreža

Verifikacija numeričkog algoritma će se provesti putem Richardsonovih ekstrapolacija, u standardnoj i generaliziranoj formi, te izračunavanjem redova točnosti numeričkog algoritma. Indeks konvergencije mreže će se također koristiti.

Standardna Richardsonova ekstrapolacija [20], [21], kao što je citirano u [22], se izračunava iz rješenja na finoj mreži f_1 s korakom h_1 te iz rješenja na gruboj mreži f_2 s korakom h_2, čiji je odnos $h_2/h_1 = 2$. Jednadžba za izračunavanje glasi:

$$\tilde{f}_{exact} = f_1 + \frac{f_1 - f_2}{3},\tag{34}$$

gdje $\tilde{f}_{exact}$ označava (standardnu) Richardsonovu ekstrapolaciju. Činjenica je da je zahtjev za omjerom koraka fine i grube mreže $h_2/h_1 = 2$ često teško i računalno skupo ispuniti što je osobito slučaj s 3D mrežama (gdje bi se profinjavanjem mreže broj ćelija trebao uvećati 8 puta). Stoga je Roache [19] uveo generaliziranu proceduru za računanje Richardsonove ektrapolacije s proizvoljnim faktorom profinjavanja mreže r i redom točnosti p. Tako se generalizirana Richardsonova ekstrapolacija $\tilde{f}_{exact}$ računa prema izrazu:

$$\tilde{f}_{exact} = f_1 + \frac{f_1 - f_2}{r^p - 1}.\tag{35}$$

Red točnosti se ne može izračunati iz samo 2 rješenja, već je potrebno i treće, f_3, dobiveno iz najgrublje mreže. Za proizvoljni i varijabilni faktor profinjavanja mreže, izraz za red točnosti glasi

$$p = \frac{\ln\left(\frac{\varepsilon_{32}}{\varepsilon_{21}}\right) + \ln\left(\frac{r_{21}^p - 1}{r_{32}^p - 1}\right)}{\ln r_{21}},\tag{36}$$

gsje su $\varepsilon_{21} = f_2 - f_1$, $\varepsilon_{32} = f_3 - f_2$, $r_{21} = h_2/h_1$ te $r_{32} = h_3/h_2$. Jednadžba (36) je transcedentna u p te je potreban iterativni postupak rješavanja. U slučaju konstantnog faktora profinjavanja mreže, jednadžba (36) se svodi na

$$p = \frac{\ln(\varepsilon_{32}/\varepsilon_{21})}{\ln r}.\tag{37}$$

Indeks konvergencije mreže (eng. *Grid Convergence Index*, skraćeno GCI) je mjera za određivanje koliko je izračunata vrijednost daleko od vrijednosti asimptotskog numeričkog

rješenja, često izražena u postocima [26]. Izrazi za izračunavanje GCI glase:

$$GCI_{21} = \frac{F_s |e_{21}|}{r_{21}^p - 1}, \tag{38}$$

$$GCI_{32} = \frac{F_s |e_{32}|}{r_{32}^p - 1}, \tag{39}$$

gdje se GCI_{21} i GCI_{32} redom odnose na procjenu pogreške srednje, odnosno fine mreže. e_{21} i e_{32} su relativne pogreške te se računaju prena izrazima $e_{21} = (f_2 - f_1)/f_1$ i $e_{32} = (f_3 - f_2)/f_2$. F_s predstavlja faktor sigurnosti te se preporuča uzeti $F_s = 3$ za slučaj analize s dvije mreže, odnosno $F_s = 1.25$ za slučaj s 3 ili više mreža, što je i slučaj u ovome radu.

Prostorna i vremenska diskretizacija

Svi validacijski slučajevi su izračunati koristeći pet uniformnih i strukturiranih dvodimenzionalnih mreža, čije detalje prikazuje tablica 5. Bezdimenzionalni vremenski korak je isti za sve slučajeve, $\Delta \hat{t} = 0.05$.

Ime mreže	Broj ćelija	Veličina ćelije ($\Delta x = \Delta y$)
40K	40 000 (200×200)	1
160K	160 000 (400×400)	0.5
360K	360 000 (600×600)	0.333
640K	640 000 (800×800)	0.25
1M	1 000 000 (1000×1000)	0.2

Tablica 5: Lista mreža kontrolnih volumena korištenih u simulacijama za sve validacijske slučajeve.

Rezultati

Rezultati svih validacijskih slučajeva će se usporediti s obzirom na različite vremenske trenutke, različite mreže u trenutku $\hat{t} = 50$ te će biti prezentirani rezultati analize konvergencija mreža. Na kraju će biti dani rezultati simulacije vrtložnog sloja.

Rezultati za trenutak t = 50

Na slikama 3 i 4 su za validacijski slučaj s horizontalnim srednjim tokom prikazana rješenja polja fluktuacije magnitude brzine $|\hat{\mathbf{U}}'| = \sqrt{\hat{u}'^2 + \hat{v}'^2}$ u gornjem redu, i fluktuacije gustoće $\hat{\rho}'$

u donjem redu. Svaki stupac na slici predstavlja drugi vremenski trenutak, definiran na vrhu svakog stupca. Akustični i entropijski val su prikazani poljem fluktuacije gustoće $\hat{\rho}'$, dok je vrtložni val prikazan poljem fluktuacije magnitude brzine $|\hat{\mathbf{U}}'|$. Na slici se primjećuje propagacija akustičnog vala te konvekcija entropijskog i vrložnog vala kroz proračunsku domenu. Valna fronta akustičnog vala se širi radijalno, no zbog srednjeg toka se također translatira nizvodno. Entropijski i vrtložni val se translatiraju zbog srednjeg toka, no bez promjene njihovog oblika ili amplitude.

Zadnji stupac na slici 3 te slika 4 prikazuju polja u vremenskim trenucima nakon što valovi stignu do granice proračunske domene. Na slici 4 se vide valovi odbijeni od otvorene granice domene, što predstavlja kontaminaciju rješenja. Primjećeno je u trenutku $\hat{t} = 280$ da kontaminacijski valovi odbijeni po drugi puta sadrže veće vrijednosti rješenja od onih koji su odbijeni jedanput. Polja u trenutku $\hat{t} = 600$ sadrže vrijednosti kontaminacijskih valova koja su višestruko veća od onih u trenutku $\hat{t} = 280$, što se može objasniti na sljedeći način: Kako se valovi šire, njihova zakrivljenost postaje manja te kako se upadni kut valova na granice domene približava nuli, odbijeni val zauzima položaj koji je gotovo jednak upadnome te se oni zbrajaju.

Polja za različite vremenske korake za validacijski slučaj s dijagonalnim srednjim strujanjem nisu prikazana jer kvalitativno ne daju dodatne informacije, pored onih opisanih za slučaj s horizontalnim srednjim strujanjem.
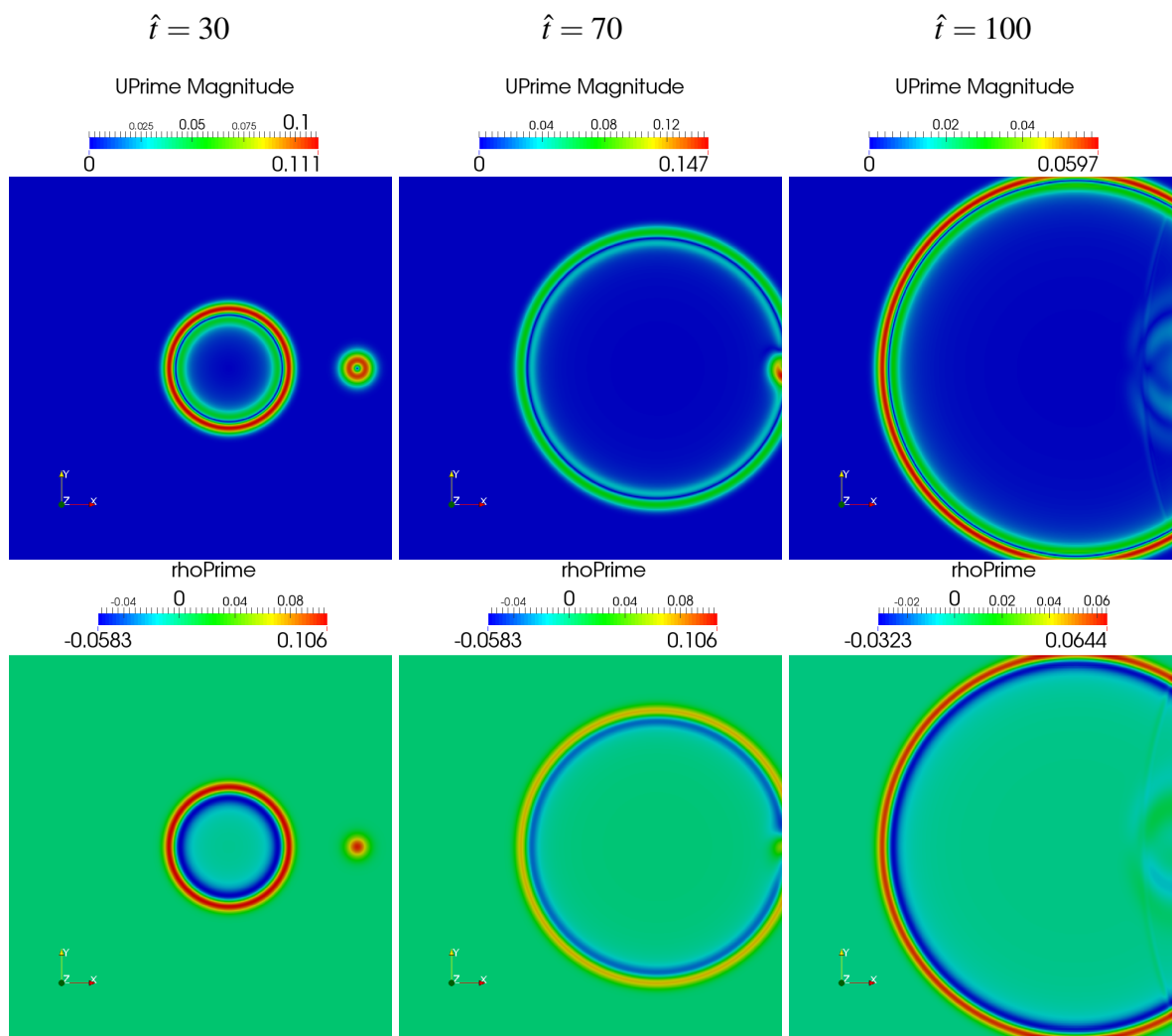
Slika 3: Slučaj s horizontalnim srednjim strujanjem: Polja fluktuacije magnitude brzine, $|\hat{\mathbf{U}}'|$ (gornji red) i fluktuacije gustoće, $\hat{\rho}'$ (donji red), mreža 1M.
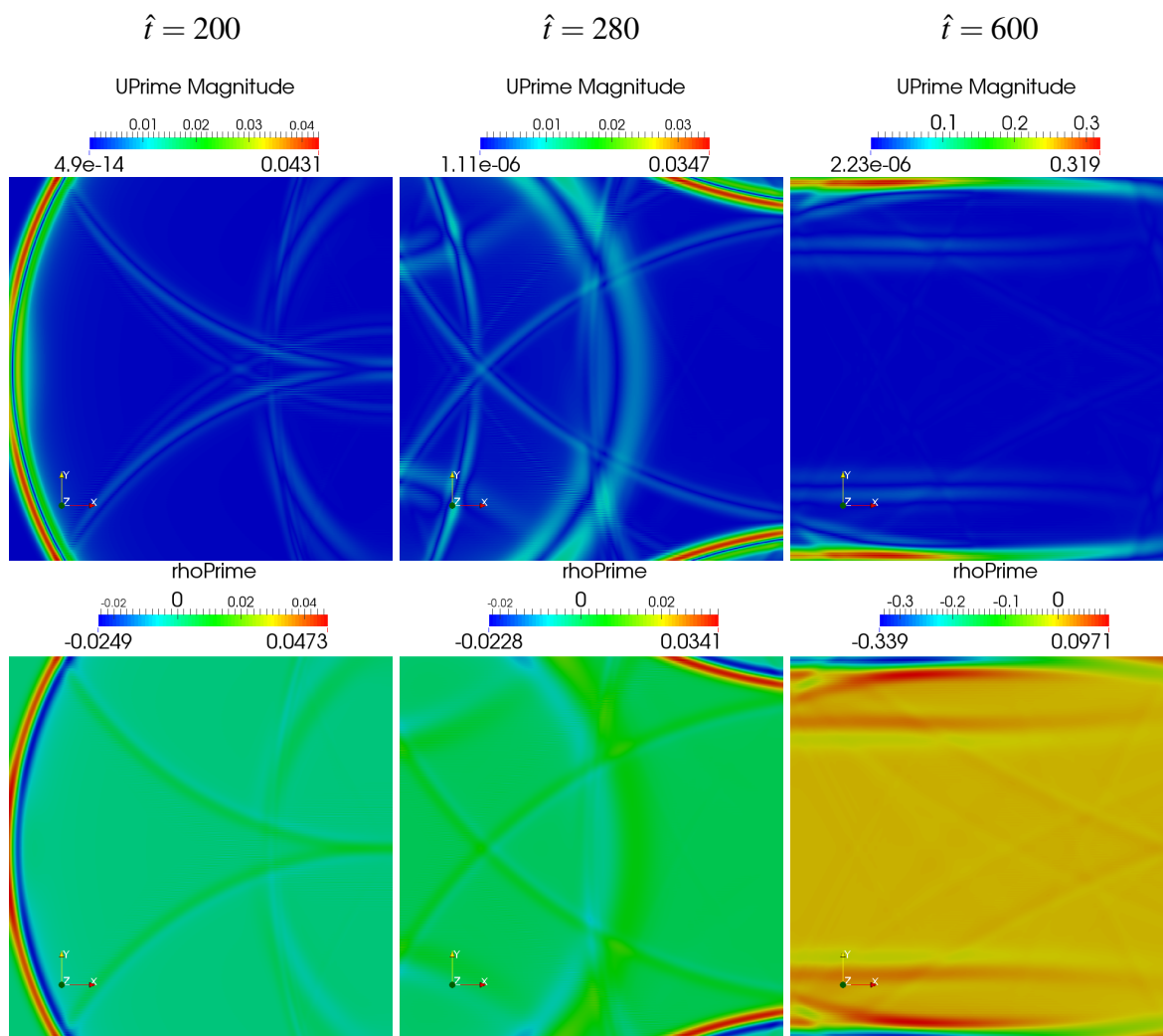
Slika 4: Slučaj s horizontalnim srednjim strujanjem: Polja fluktuacije magnitude brzine, $|\hat{\mathbf{U}}'|$ (gornji red) i fluktuacije gustoće, $\hat{\rho}'$ (donji red), mreža 1M.

Budući da validacijski slučaj s reflektirajućim zidom ne sadrži entropijske i vrtložne valove, umjesto polja $\hat{\rho}'$, na slici 5 je prikazivano polje fluktuacije tlaka $\hat{p}'$. Slika prikazuje širenje akustičkog vala, njegovu konvekciju srednjim tokom, odbijanje od zida te na kraju (trenuci $\hat{t} = 70$ i $\hat{t} = 150$) i odbijanje od otvorene granice domene ($\hat{t} = 150$). Osim polja $|\hat{\mathbf{U}}'|$ i $\hat{p}'$, donjem je redu prikazano i polje razlika između analitičkog i numeričkog rješenja, kako bi se dobila informacija o kvaliteti odbijanja vala od zida. Iz polja razlika se vidi da numeričko rješenje naizgled jednako kvalitetno opisuje neodbijeni val i val odbijen od zida.
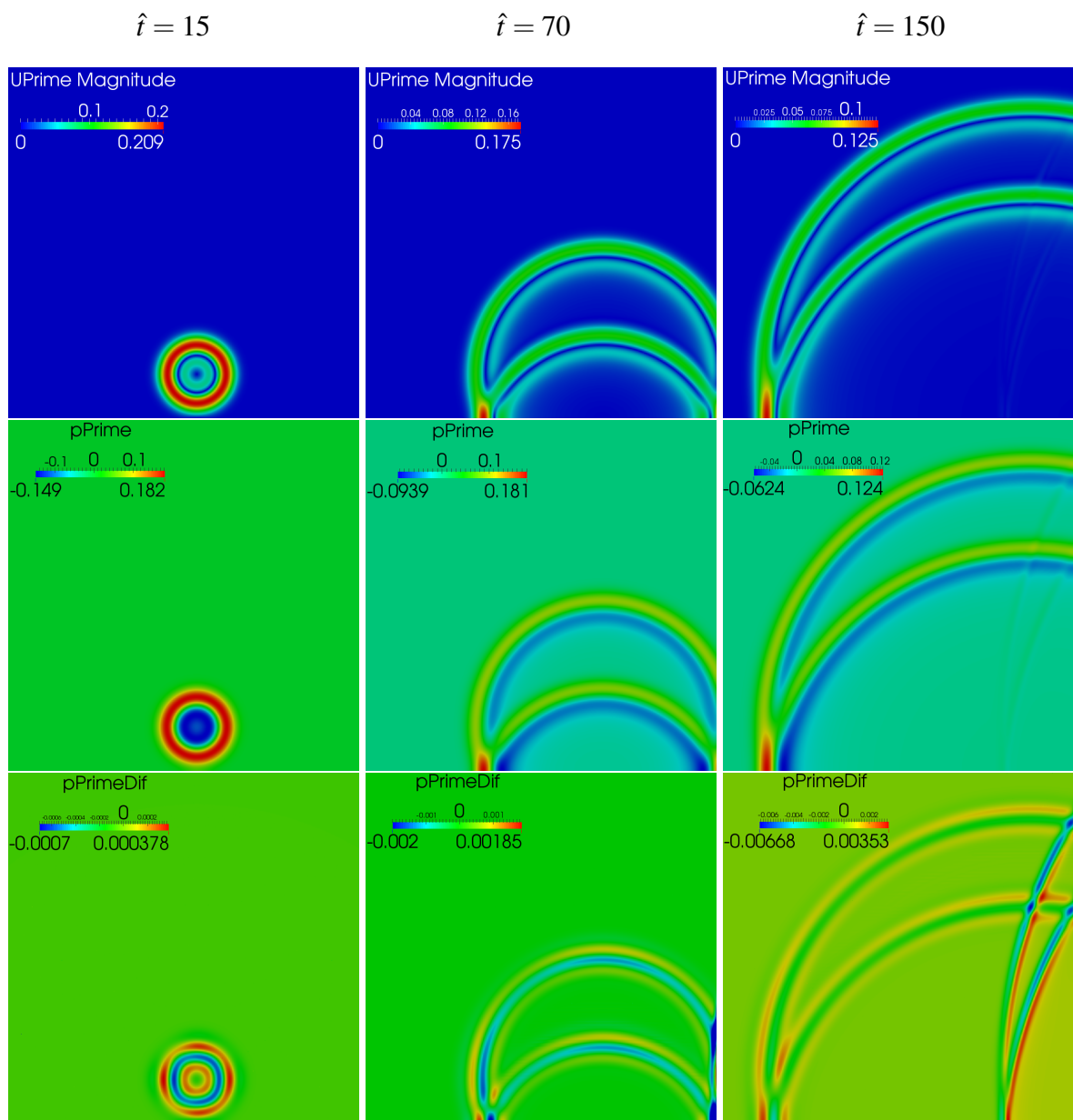
Slika 5: Slučaj s reflektirajućim zidom: Polja fluktuacije magnitude brzine, $|\hat{\mathbf{U}}'|$ (gornji red), fluktuacije tlaka, $\hat{p}'$ (srednji red), razlike između analitičnog i numeričkog rješenja za $\hat{p}'$, mreža 1M.

Rezultati za trenutak t = 50

Za slučajeve s horizontalnim i dijagonalnim srednjim strujanjem, trenutak $\hat{t} = 50$ je odabran jer valovi do tada još nisu stigli do otvorenih granica te da se analizira samo radijacija i konvekcija valova, bez kontaminacije odbijenih valova. U slučaju s reflektirajućim zidom, refleksija od zida se u $\hat{t} = 50$ već dogodila, no uvjet da se odbijanje od otvorene granice ne dogodi ostaje zadovoljen.

Slike 6, 7 i 8 prikazuju vrijednosti polja fluktuacije tlaka $\hat{p}'$, gustoće $\hat{\rho}'$ i komponenata brzine $\hat{u}'$ i $\hat{v}'$ za slučaj s horizontalnim srednjim strujanjem, dobivene numerički koristeći mreže 40K, 360K i 1M. Rješenja na spomenutim slikama su uzeta iz horizontalnog presjeka, na $y = 0$. Rezultati dobiveni koristeći mreže 160K i 640K nisu prikazani jer su za sljedeće razmatranje dovoljni rezultati prikazani na slikama 6, 7 i 8. Na tim su slikama analitička rješenja prikazana plavom linijom, numerička rješenja crvenom linijom, a razlike između analitičkih i numeričkih rješenja su prikazane crnom crtkanom linijom.

Sa slika se jasno vidi da se razlike između analitičkih i numeričkih rješenja smanjuju povećanjem rezolucije mreže. Razlike se generiraju zbog numeričke disperzije i disipacije. Numerička disperzija se prepoznaje zbog postojanja valova koji nisu u fazi s analitičkim rješenjima, dok se numerička disipacija prepoznaje u smanjenoj amplitudi numeričkih rješenja. Numerička disperzija i disipacija se najviše prepoznaju na rješenjima dobivenih najgrubljom mrežom 40K. Razlika generirana numeričkom disperzijom, odnosno malim pomakom u fazi, veća je od one generirane razlikom amplituda analitičkog i numeričkog rješenja. Po autorovom mišljenu se te razlike ne bi smjele uspoređivati, zbog čega je u analizi konvergencija mreža, čiji će rezultati kasnije biti predtavljeni, u obzir uzeta samo numerička disipacija, odnosno vršne vrijednosti fluktuacije tlaka $\hat{p}'$.

Rezultati slučaja s dijagonalnim srednjim strujanjem po presjeku $x = y$ nisu predstavljeni jer kvalitativno nijedna razlika nije uočena u odnosu na rezultate za slučaj s horizontalnim srednjim strujanjem (slike 6, 7 i 8).
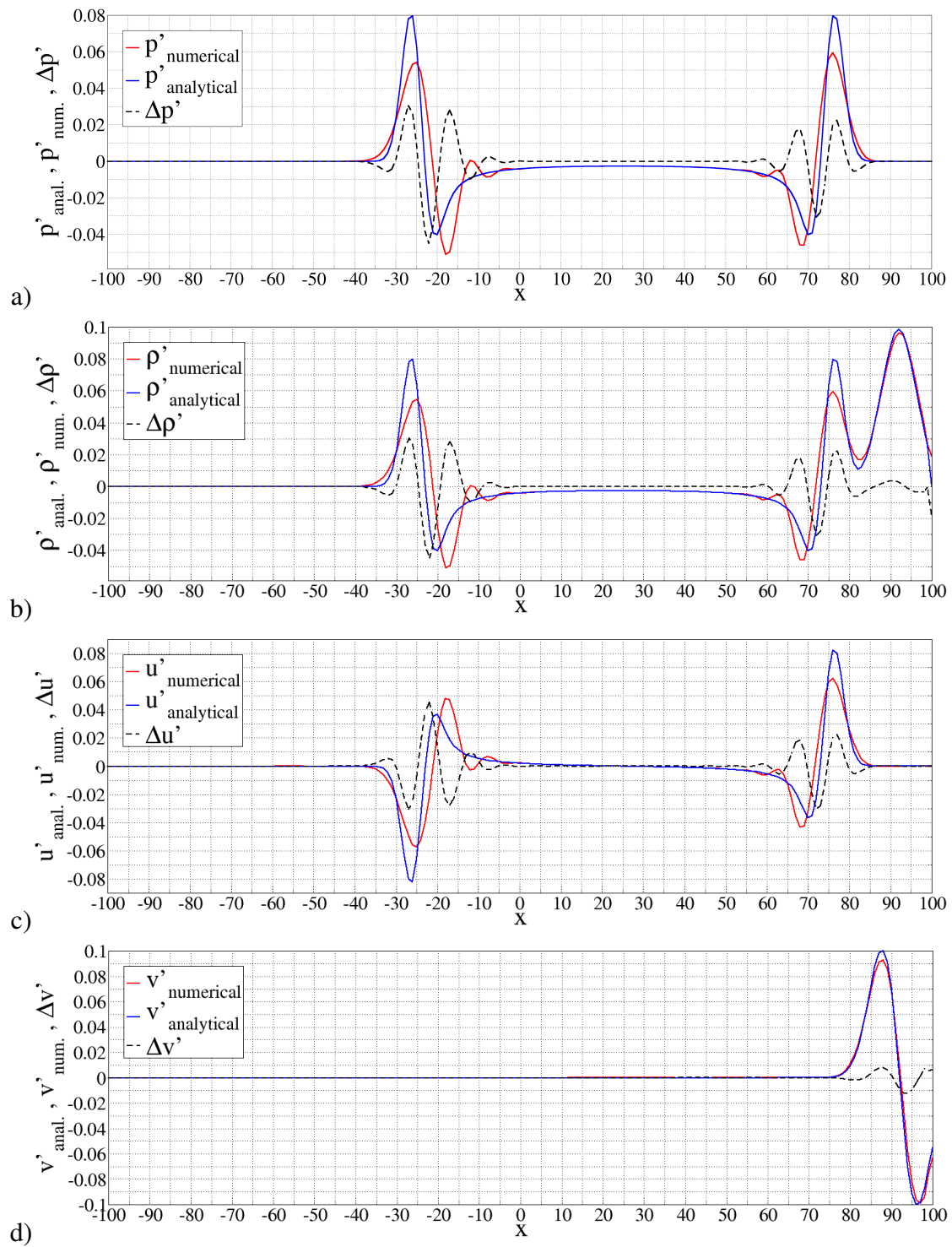
Slika 6: Akustična polja fluktuacije: a) tlaka $\hat{p}'$, b) gustoće $\hat{\rho}'$ i komponentata brzine c) $\hat{u}'$ i d) $\hat{v}'$ u trenutku $\hat{t} = 50$, $y = 0$, mreža 40K.
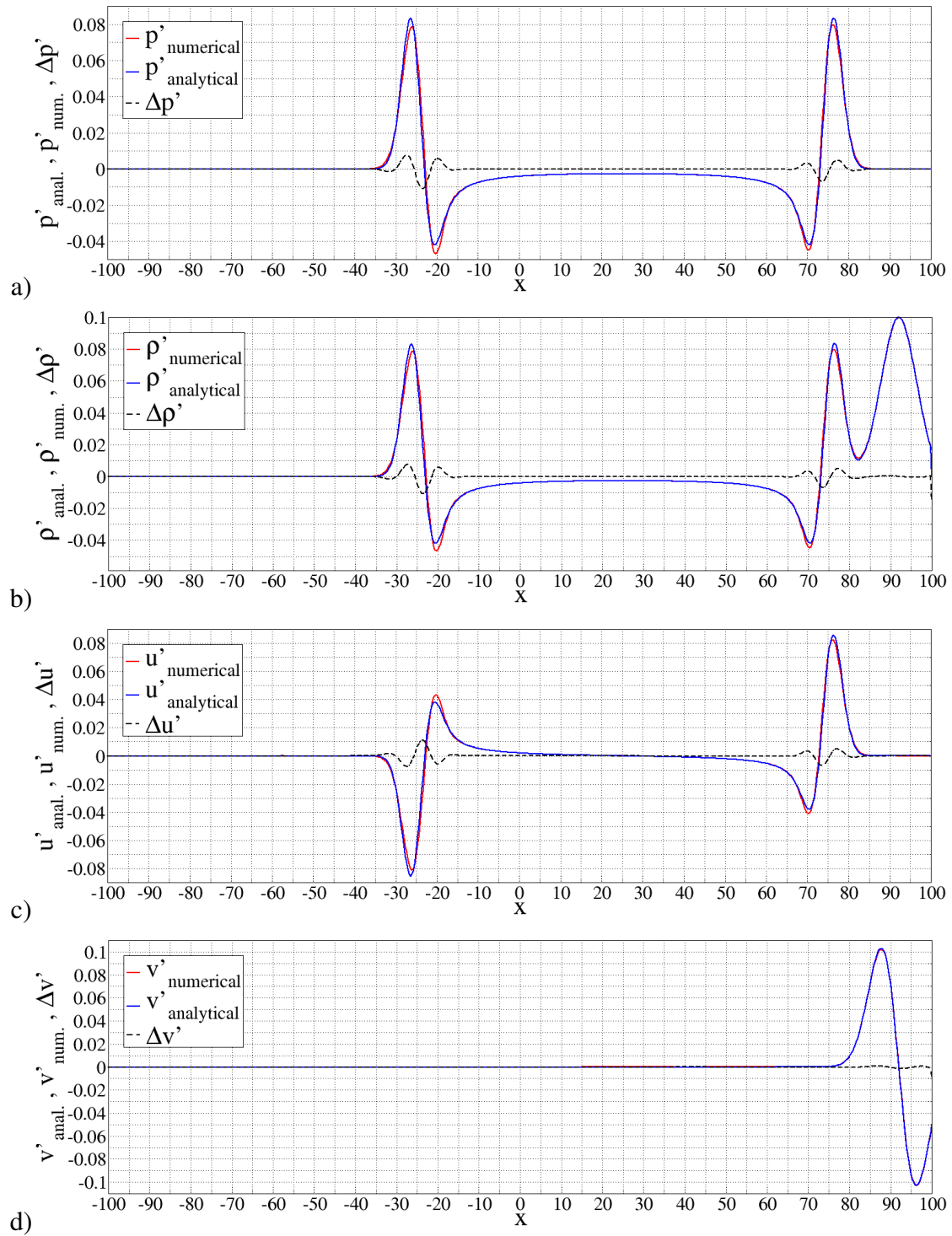
Slika 7: Akustična polja fluktuacije: a) tlaka $\hat{p}'$, b) gustoće $\hat{\rho}'$ i komponentata brzine c) $\hat{u}'$ i d) $\hat{v}'$ u trenutku $\hat{t} = 50$, $y = 0$, mreža 360K.
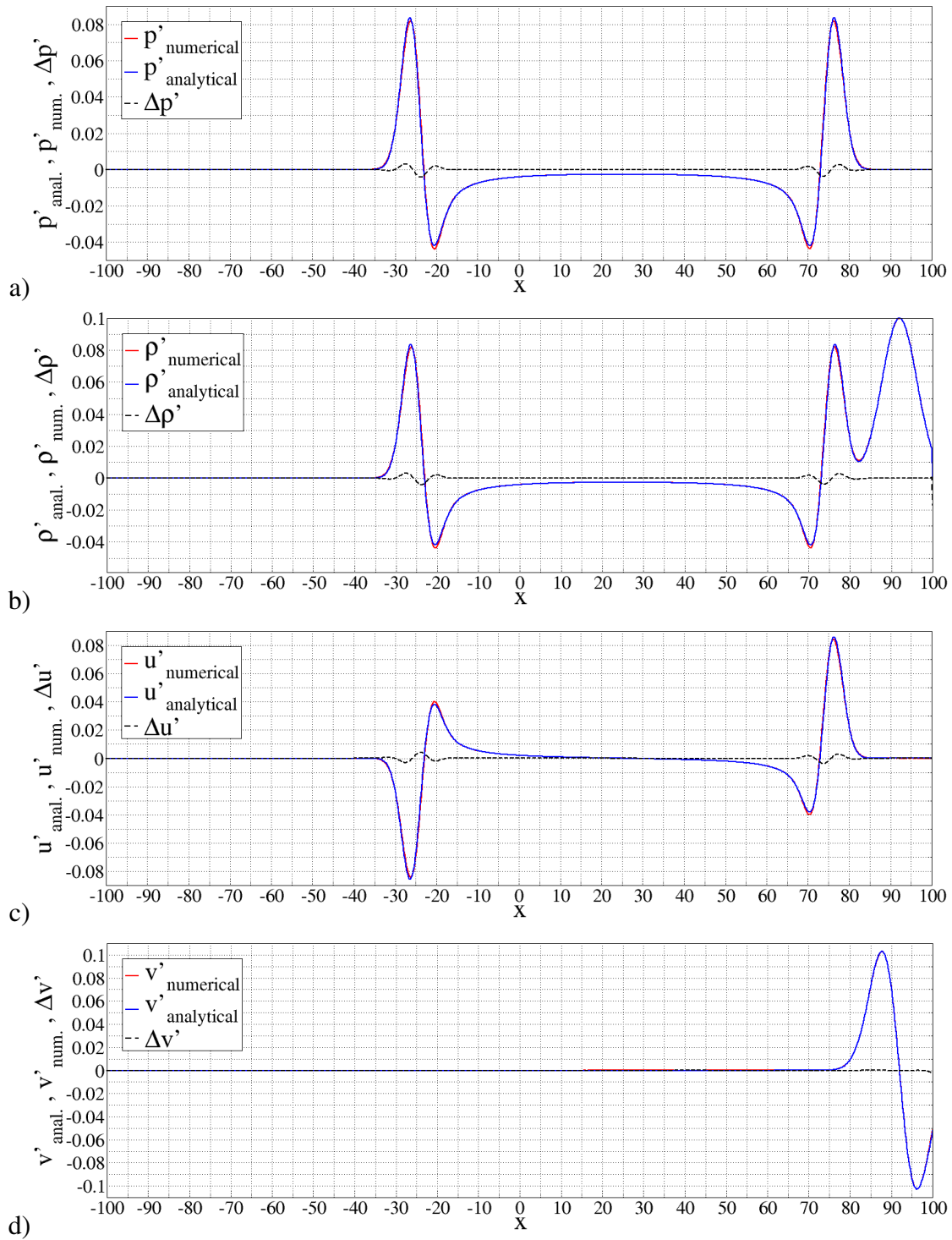
Slika 8: Akustična polja fluktuacije: a) tlaka $\hat{p}'$, b) gustoće $\hat{\rho}'$ i komponentata brzine c) $\hat{u}'$ i d) $\hat{v}'$ u trenutku $\hat{t} = 50$, $y = 0$, mreža 1M.

Kako validacijski slučaj s reflektirajućim zidom sadrži samo akustični val, polje fluktuacije tlaka $\hat{p}'$ će biti prikazano. U slučaju su rezultati u trenutku $\hat{t} = 50$ uzeti iz presjeka $x = 25$, koji prolazi centrom akustičkog vala. Sa slike 9 je vidljivo da profinjavanjem mreže rezultati konvergiraju najbrže, u odnosu na slučajeve s horizontalnim i dijagonalnim srednjim strujanjem, a rezultati finijih mreža nisu niti prikazani, jer ne donose nove informacije. Razlog najbržoj konvergenciji rješenja leži u činjenici da je inicijalno polje fluktuacije tlaka bilo šire u odnosu na inicijalna polja ostalih slučajeva, odnosno gradijenti akustičnih polja su u slučaju s reflektirajućim zidom manji nego u prva dva slučaja.
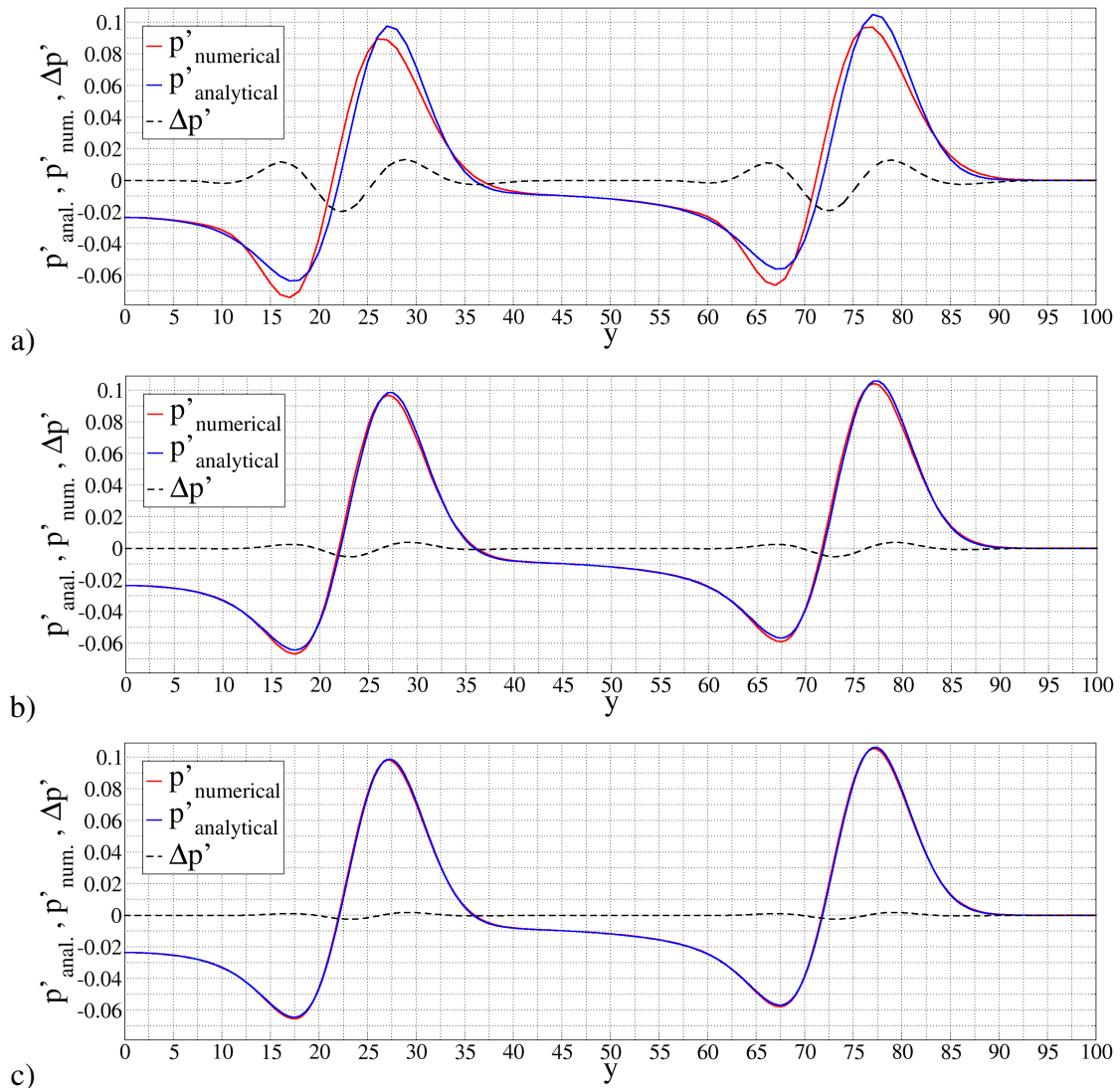
Slika 9: Fluktuacija tlaka $\hat{p}'$ dobivena na mrežama: a) 40K, b) 160K, c) 360K u trenutku $\hat{t} = 50$, $x = 25$.

Analiza konvergencija mreža

Za slučajeve s horizontalnim i dijagonalnim srednjim strujanjem je analiza konvergencija mreža provedena uzimajući u obzir vršne fluktuacije tlaka $\hat{p}'_{loc.max.}$ (lokalni maksimumi) u akustičkoj valnoj fronti koja propagira uzvodno (lijevi val na presjecima $y = 0$ u slučaju s horizontalnim i $x = y$ u slučaju s dijagonalnim srednjim strujanjem). Taj je val izabran zbog činjenice da su odstupanja numeričkih rješenja od analitičkih veća nego u slučaju uzvodno propagirajuće valne fronte. Analiza je vršena uzimajući u obzir i razlike između lokalnog minimuma i lokalnog maksimuma na spomenutom valu, no to u proširenom sažetku neće biti prikazano. Ispitivanje konvergencija mreža se za slučajeve s horizontalnim i dijagonalnim srednjim strujanjem radilo uzimajući u obzir dvije kombinacije mreža: grubu kombinaciju (mreže 40K, 160K, 640K) i finu kombinaciju (360K, 640K, 1M). Može se primjetiti da je profinjavanje mreža u gruboj kombinaciji provedeno s konstantnim faktorom profinjavanja $r = 2$.

Tablice 6 i 7 prikazuju vrijednosti $\hat{p}'_{loc.max.}$ za odgovarajuće mreže. Red točnosti p_G je izračunat koristeći jednadžbu (37) u slučaju kombinacije grubih mreža (tablica 6, konstantni r) te koristeći jednadžbu (36) u slučaju kombinacije finih mreža (tablica 7, promjenjiv r: $r_{32} = 1.333$, $r_{21} = 1.25$). Za obje tablice su Richardsonove ektrapolacije računate u generaliziranoj formi (jednadžba (35)) kako bi rezultati bili usporedivi.

Ime mreže	Veličina ćelije	$\hat{p}'_{loc.max.}$	$\tilde{f}_{exact}$	$f_{anal.}$	GCI (%)	$\frac{GCI_{32}}{r^p GCI_{21}}$	p_G
40K	1	0.05425	-		-	-	
160K	0.5	0.07256	0.08742	0.0835	$GCI_{32} = 25.62$	1.11	1.158
640K	0.25	0.08076			$GCI_{21} = 10.32$		

Tablica 6: Analiza konvergencija mreža: kombinacija grubih mreža, slučaj s horizontalnim srednjim strujanjem.

Analogno analizi konvergencija mreža za slučaj s horizontalnim srednjim strujanjem, provode se analize i za slučajeve s dijagonalnim srednjim strujanjem i s reflektirajućim zidom. Tablice 8 i 9 prikazuju podatke dobivene kobinacijom grubih i finih mreža za slučaj s dijagonalnim srednjim strujanjem, dok tablice 10 i 11 prikazuju podatke za slučaj s reflektirajučim zidom za nereflektirani i reflektirani val od zida dobivene kombinacijom samo grubih mreža.

Ime mreže	Veličina ćelije	$\hat{p}'_{loc.max.}$	$\tilde{f}_{exact}$	$f_{anal.}$	GCI (%)	$\frac{GCI_{32}}{r^p GCI_{21}}$	p_G
360K	0.333	0.078518	-		-	-	
640K	0.25	0.08076	0.083757	0.0835	$GCI_{32} = 4.73$	0.97	1.944
1M	0.2	0.081816			$GCI_{21} = 2.96$		

Tablica 7: Analiza konvergencija mreža: kombinacija finih mreža, slučaj s horizontalnim srednjim strujanjem.

Ime mreže	Veličina ćelije	$\hat{p}'_{loc.max.}$	$\tilde{f}_{exact}$	$f_{anal.}$	GCI^{fine} (%)	$\frac{GCI_{32}}{r^p GCI_{21}}$	p_G
40K	1	0.06717	-		-	-	
160K	0.5	0.07885	0.0841	0.0835	$GCI_{32} = 8.32$	1.04	1.689
640K	0.25	0.082473			$GCI_{21} = 2.46$		

Tablica 8: Analiza konvergencija mreža: kombinacija grubih mreža, slučaj s dijagonalnim srednjim strujanjem.

Ime mreže	Veličina ćelije	$\hat{p}'_{loc.max.}$	$\tilde{f}_{exact}$	$f_{anal.}$	GCI^{fine} (%)	$\frac{GCI_{32}}{r^p GCI_{21}}$	p_G
360K	0.333	0.0813	-		-	-	
640K	0.25	0.08247	0.08356	0.0835	$GCI_{32} = 1.64$	0.925	2.545
1M	0.2	0.08294			$GCI_{21} = 0.92$		

Tablica 9: Analiza konvergencija mreža: kombinacija finih mreža, slučaj s horizontalnim srednjim strujanjem.

Uzimajući u obzir tablice 8 i 9, odnosno redove točnosti p_G, jasno je da slučaj s dijagonalnim srednjim strujanjem (DSS) (na presjeku $x = y$) daje točnija numerička rješenja nego slučaj s horizontalnim srednjim strujanjem (HSS) (na presjeku $y = 0$). Ispitivanjem numeričkih rezultata slučaja s HSS na dijagonalnom presjeku (s ishodištem u $x = 25$, $y = 0$, odnosno u

Ime mreže	Veličina ćelije	$\hat{p}'_{loc.max.}$	$\tilde{f}_{exact}$	$f_{anal.}$	GCI^{fine} (%)	$\frac{GCI_{32}}{r^p GCI_{21}}$	p_G
40K	1	0.09691	-		-	-	
160K	0.5	0.10429		0.1064	GCI$_{32}$ = 2.45		2.205
640K	0.25	0.10589	0.10633		GCI$_{21}$ = 0.52	1.015	

Tablica 10: Analiza konvergencija mreža: kombinacija grubih mreža, slučaj s reflektirajućim zidom, nereflektirani val.

Ime mreže	Veličina ćelije	$\hat{p}'_{loc.max.}$	$\tilde{f}_{exact}$	$f_{anal.}$	GCI^{fine} (%)	$\frac{GCI_{32}}{r^p GCI_{21}}$	p_G
40K	1	0.08836	-		-	-	
160K	0.5	0.09691		0.0989	GCI$_{32}$ = 2.49		2.439
640K	0.25	0.098484	0.09884		GCI$_{21}$ = 0.45	1.016	

Tablica 11: Analiza konvergencija mreža: kombinacija grubih mreža, slučaj s reflektirajućim zidom, reflektirani val.

centru akustičkog vala), koji je jednake orjentacije kao presjek u slučaju s DSS, dobivaju se rješenja koja se zanemarivo različita od rješenja slučaja s DSS. Tako se može zaključiti da razlika između redova točnosti rješenja slučajeva s HSS i DSS nije posljedica različitog srednjeg toka, već različitog smjera propagacije akustičkog vala, s obzirom na orjentaciju mreže.

Podaci iz tablica 10 i 11 potvrđuju da numerička rješenja slučaja s reflektirajućim zidom (RZ) konvergiraju s najvišim redom točnosti. Razlog leži u činjenici da je širina inicijalne distribucije akustičnih polja $\hat{p}'$, $\hat{\rho}'$ u slučaju s RZ veća nego u slučajevima s HSS i DSS.

Simulacija buke generirane vrtložnim slojem

Prateći metode stohastičkog generiranja i širenja buke (eng. *Stochastic Sound Generation and Radiation*, skraćeno SNGR) iz poglavlja 3.4, no u pojednostavljenom obliku, neuspješno je provedena simulacija dvodimenzionalnog vrtložnog sloja.

Rubni uvjet brzine na ulazu je definiran sljedećim izrazom:

$$U(y) = \frac{U_1 + U_2}{2} + \frac{U_1 - U_2}{2} \tanh\left(\frac{2y}{\delta_\omega(0)}\right),$$ (40)

gdje je $\delta_\omega(0) = 0.02$ m početna debljina vrtložnog sloja. Slika 10 prikazuje domenu proračuna s profilom brzine na ulaznoj granici. Slika 11
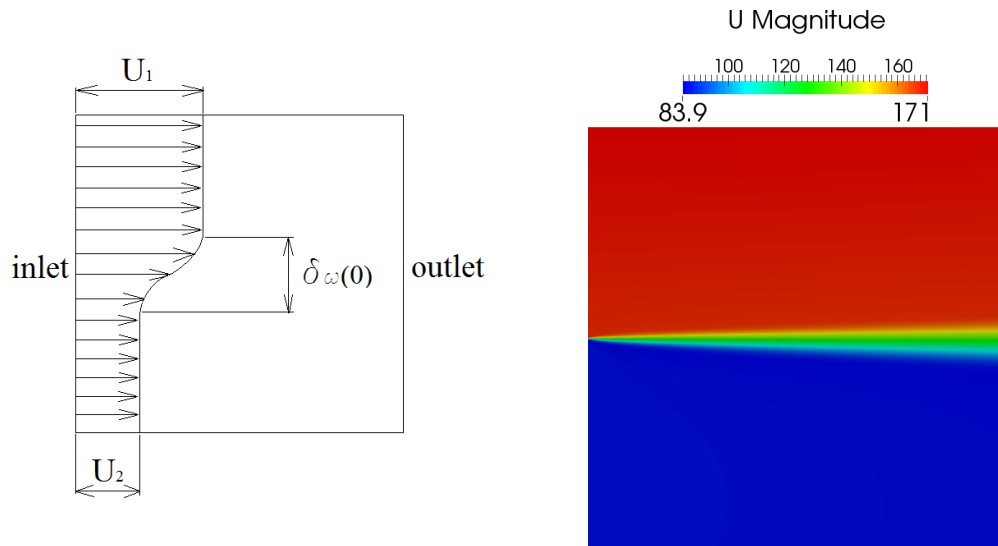
Slika 10: Domena proračuna s prikazanim profilom brzine na ulaznoj granici.

Slika 11: RANS rješenje simulacije vrtložnog sloja (prikazana je apsolutna vrijednost osrednjene brzine $\bar{u}$).

Slika 11 prikazuje polje osrednjene brzine dobivene RANS simulacijom. Sintetizirano polje turbulentne brzine je izračunato u pojednostavljenom obliku:

$$u_t = \sqrt{\frac{2}{3}k}\mathbf{R},$$ (41)

gdje u_t predstavlja sintetizirano polje turbulentne brzine, k predstavlja turbulentnu kinetičku energiju i $\mathbf{R}$ predstavlja vektor nasumične orijentacije, čija norma iznosi $|\mathbf{R}| = 1$.

Generiranje akustičnih polja, odnosno zvuka se odvija preko računanja nehomogenih lineariziranih Eulerovih jednadžbi, donosno preko izvorskog člana na dasnoj strani jednadžbe količine gibanja (11) koji glasi:

$$S_{acoustic} = -\frac{\partial}{\partial x_j}\left(\bar{\rho}u'_{ti}u'_{tj} - \overline{\rho u'_{ti}u'_{tj}}\right),$$ (42)

kao što je opisan u [24].
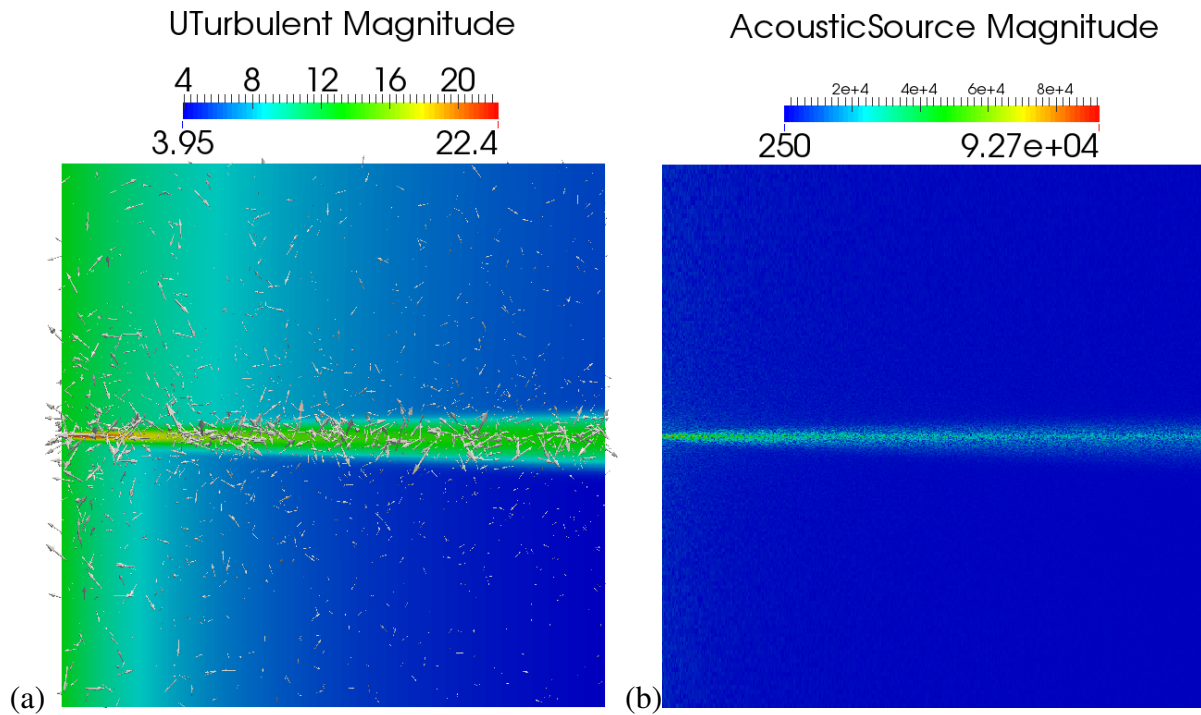
Slika 12: (a) Sintetizirano polje turbulentne brzine s nasumičnim orijentacijama, (b) polje akustičnog izvora $S_{acoustic}$.

Numeričko rješenje nehomogenih LEE nije prikazano jer je simulacija bila nestabilna te su vrijednosti polja brzo divergirale. Uzrok nestabilnosti je u velikim iznosima polja akustičnog izvora, koja su vjerojatno nefizikalna, što se vidi u rasponu vrijednosti podataka na slici 12 (b).

Prema autorovom mišljenju, najveću ulogu u generiranju nefizikalnog izvorskog polja igra gruba metoda izračunavanja turbulentnog akustičnog polja. Druga mogućnost leži u potencijalnoj grešci u dijelu računalnog koda koji je povezan s nehomogenim srednjim tokom.

Zaključak

U ovome je radu provedena implementacija, verifikacija i validacija lineariziranih Eulerovih jednadžbi (eng. *Linearised Euler Equations*, skraćeno LEE), koje matematički opisuju propagaciju zvučnih valova. LEE su riješene metodom kontrolnih volumena, koristeći programski paket OpenFOAM-extend. Implementirane LEE su u konzervativnoj formi, koja je pogodna za diskretizaciju kontrolnim volumenima.

Verifikacija i validacija LEE rješavača (eng. *solver*) su provedene koristeći tri validacijska slučaja, koji su definirani u [2] kao problemi 1 i 2 kategorije 3 te problem 1 kategorije 4. Vali-

dacija je provedena uz analitička rješenja koja su također definirana u [2]. Validacijski slučajevi se sastoje od inicijalne distribucije akustičnih veličina, koje predtavljaju problem početnih vrijednosti, koji pak se treba numerički riješiti koristeći LEE. Propagacija akustičnog vala te rubni uvjeti zida i otvorene granice su verificirani i validirani rješavanjem LEE i uspoređivanjem numeričkih i analitičkih rješenja. Studija konvergencija mreža je također provedena.

Rezultati validacijskih slučajeva su uspoređeni za različite vremenske vrenutke i različite rezolucije mreža kontrolnih volumena. Numerička rješenja su u skladu s analitičkim rješenjima sve dok akustični, entropijski i vrtložni valovi ne stignu do otvorene granice domene. Studija konvergencija mreža je pokazala da rješenja akustičnih veličina konvergiraju prema asimptotskim numeričkim rješenjima, koja su blizu analitičkih rješenja. Zaključeno je da razlika između redova točnosti rješenja za slučajeve 1 i 2 nije posljedica različitog srednjeg toka, već različitog smjera propagiranja valne fronte, uspoređujući s orjentiranosti mreže.

Red točnosti rješenja je najviši kod slučaja 3 zbog činjenice da je inicijalna distribucija akustičnih polja šira kod slučaja 3, uspoređujući sa slučajevima 1 i 2. Zaključeno je da veličina gradijenata akustičnih polja uvelike utječe na točnost numeričkog algoritma. Uzimajući u obzir da su ispitani i nereflektirani i reflektirani val od zida, zaključuje se da je numerički algoritam daje rješenja jednake točnosti za reflektirani i nereflektirani val.

Nakon što valovi napuste domenu, određen dio se odbije nazad u domenu koji kontaminira rješenja. Poslije nekoliko refleksija od otvorene granice, valovi rastu u amplitudi zbog međusobne superpozicije. Kontaminacijski valovi se javljaju zbog toga što je korišten neadekvatan von Neumannov rubni uvjet, u nedostatku boljeg.

Simulacija buke generirane vrtložnim slojem je neuspješto provedena zbog njene nestabilnosti. Prema autorovom mišljenju, razlog leži u gruboj metodi računanja polja turbulentne brzine, ili u mogućoj grešci u dijelu računalnog koda koji je povezan s nehomogenim srednjim tokom.

U konačnici se može zaključiti da je implementacija lineariziranih Eulerovih jednadžbi provedena uspješno. Rezultati triju validacijskih slučajeva dokazuju da se propagacija zvučnih valova može s dovoljnom točnošću računati koristeći implementirani solver, kao i valjanost rubnog uvjeta zida.

U budućim istraživanjima i radovima, trebalo bi implementirati i testirati nereflektirajući rubni uvjet, kako bi se izbjegla kontaminacija rješenja reflektiranim valovima. Također bi tre-

balo implementirati i validirati bolju metodu za sintezu polja turbulente brzine, kao i njenu vremensku ovisnost.

Chapter 1

Introduction

1.1 Background

There are different aspects of acoustics that affect the quality of our lives. The useful and positive side are the sounds that help us orient ourselves: sound of wind and rain, sounds of road traffic, information exchange between people or music that stimulates our emotions. Negative aspect of acoustics is noise. Quality of life is often influenced by presence of noise. Hence, in the last few decades many studies have been conducted in order to minimize noise pollution.

Very loud sounds clearly have negative impact on health. Long-term exposure to high noise level can result in permanent hearing loss. There are even non-auditory effects on health known, such as psychological reactions: increased blood pressure, heart rate, etc. Exposure to high noise levels during pregnancy can result in high frequency hearing loss in newborns. Besides physical damage, there are also negative impacts on psychological health of person [1].

Most sources of noise that the studies deal with are man-made (e.g., road traffic, trains or aircraft). There are several physical mechanisms that produce noise [1]:

- Solid-body friction noise (e.g. gearbox)

- Solid-body vibration (e.g. excentered rotation mechanisms)

- Combustion noise (e.g. piston engines, combustion chambers)

- Shocks (e.g. explosions)

- Flow-induced noise (e.g. vortex-structure interaction)

Flow-induced noise (e.g. aerodynamic noise) is one of the biggest sources of noise emission. There are several examples of aerodynamically induced noise: external and internal vehicle noise emission, aircraft noise (due to free-jet flow or air flow around wings, flaps and landing gear), bow collector noise at high-speed trains or wind turbine noise (either due to blade-tower interaction for large wind turbines with lower rotational velocities or due to vortex-blade interaction for smaller, fast rotating turbines).

Computational Aeroacoustics (CAA) deals with simulations of sound generated by unsteady flows and is a rapidly growing area due to increased availability of computational resources [1].

In this thesis the implementation of the model for the propagation of acoustic waves has been conducted. The model consists of the linearised Euler equations which have been implemented in OpenFOAM-extend software, an open-source C++ Computational Continuum Mechnics (CCM) libraries [27]. Verification and validation have been made on three benchmark cases [2], where the analytical solutions are given. A grid convergence study has also been conducted. In the end, the mixing layer CAA simulation has been preformed.

The thesis is organized as follows: The first chapter gives introduction to acoustics in general, as well as the introduction to the Computational Aeroacoustics (CAA), along with the methodology, approaches and common techniques in the CAA. The second chapter deals with the governing equations of fluid dynamics, order of magnitudes in the free-space acoustics, wave equation with elementary solutions and aeroacoustic analogies. In the third chapter the linearised Euler equations, which are implemented in the code, are derived. In the same chapter the non-reflecting boundary conditions in CAA are described, as well as the method for generation of sound sources. In the fourth chapter numerical methodology, benchmark cases with corresponding analytical solutions and the equations for the grid convergence error analysis are given. The fifth chapter gives the computational parameters, specifically the finite volume grids, numerical schemes and boundary conditions used in this thesis. The sixth chapter presents the results of three benchmark cases, as well as the grid convergence analysis. At the end of that chapter, the results obtained from the mixing layer simulation are presented. Lastly, the conclusion to this thesis is given.

1.2   Computational Aeroacoustics

In recent years aeroacoustics has come into focus of research of many scientists. The reason lies in big advances in computer technology that allow application of numerical methods in prediction of acoustic fields. The approach to predicting sound field using numerical methods is called Computational Aeroacoustics (CAA). Before the current computer era, when numerical approaches were not feasible, there was a long period of time when engineers's work was mostly based on analytical and experimental studies.

Today's concept of CAA rests in the research of Sir James Lighthill [3] in early 1950s. He introduced the idea of representing sound as the difference between the actual flow and the reference flow, usually a quiescent medium. Lighthill has named his acoustic theory an *analogy*. J. E. Ffowcs Williams and D. L. Hawkings [4] have extended Lighthill's acoustic analogy to the case of moving surfaces that are immersed in the flow in late 1960s. Mostly, the studies of that time have been focused on sounds emitted from jets, the reason being their simple geometry (no solid walls), and also because this sound source presented a major problem of jet engines developed back then.

1.2.1   Aerodynamically Induced Sound Sources

In practice aerodynamic noise occurs because of three basically different phenomena [1].

1. The first noise mechanism is *Impulsive* noise, which occurs as a result of moving surfaces or when a surface is immersed in nonuniform flow conditions. This kind of noise is relatively easy to calculate because required resolution in space and time in the prediction of an acoustic field is similar to the demands from the Computational Fluid Dynamics (CFD) calculation. Impulsive noise can be obtained from unsteady aerodynamic calculations. There are several examples of impulsive noise: helicopter rotors, wind turbines, turbine engine fans, ventilators, etc.

2. The second noise mechanism is the result of turbulence in fluid flows and it is present in almost every engineering application. Unlike the case with impulsive noise where tonal noise can be dominant, turbulence generates noise with broad frequency spectrum because of its stochastic nature. For example, mixing region of a jet flow is a big sound

generator because of the shear layer (i.e. the zone with significant viscous shear stresses) that produces turbulence.

3. The third mechanism that produces noise is combustion where chemical reactions introduce energy into the flow.

Most of aerodynamic noise is broadband (turbulence) noise that is augmented by tonal components produced by impulsive noise sources. As is the case in CFD, noise generated by turbulence is difficult to calculate because the turbulence often has to be modeled, either via Reynolds-Averaged Navier-Stokes (RANS) approach or via Large Eddy Simulation (LES). In addition to this, the direct numerical simulation (DNS) can be carried out to solve the turbulence fully, without modeling, but at a prohibitive computational cost.

1.2.2   Different Approaches to Solving Computational Aeroacoustics

There has not been defined a clear path to follow for obtaining reliable acoustical information for every application yet. There are many different methods, but each works well in a specific area and fails in others.

The most straightforward approach in CAA is the direct method. It does not include any modeling of sound, hence does not suffer from approximation errors. Using the direct method, fully coupled compressible Euler or Navier-Stokes equations are solved from aerodynamic effective area to the observer [1]. There are two major issues related to the use of the direct method. First, it requires enormous amount of computational resources and second, even if the computational resources were available, standard CFD discretisation schemes are not suitable for CAA applications because of their dispersion and diffusion errors.

There is a big disproportion in properties between CFD and CAA. CFD is designed to solve a near-field problem (because perturbations from the mean flow vanish quickly), whereas the CAA deals with far-field problems. Furthermore, the flow in the near-field zone is usually non-linear and quasi-stationary, while in the far-field, outside aerodynamic active area, the perturbations are usually small and, therefore, linearisation of equations can be considered to introduce an acceptable level of modelling error.

Taking into account considerations presented above, one can conclude that the specifically designed methods for specific set of problems will be more superior to general ones that would

have to take care of all the different properties of CFD and CAA.

Nowadays, the CAA methods are mostly of hybrid type with **sound generation methods** decoupled from sound transport methods. Sound generation methods are:

- **CFD sources**, which refer to direct coupling mechanism from CFD data to sound data. That kind of acoustic source is more applicable than the direct method mentioned above, because the dispersion and diffusion errors need to be kept low in the transport only up to the boundaries of the coupling region (surface or volume that contains sound sources).

- **Semi-empirical sources**, where CFD data can also provide data for sound sources by using information from turbulent quantities. Steady RANS computation provides information about turbulent length and time scales that can be translated by empirical relations into sound-source information. These methods are fast but also depend on validation of empirical relations.

There are also two alternatives in **sound transport methods**:

- **Computational transport methods**: These methods are similar to computation in CFD because they solve partial differential equations in the entire field. They do not simulate fluid dynamics as is the case of direct methods, but only the acoustic field. Computational transport methods solve simplified equations (such as linearized Euler equations or wave equation) and, therefore, discretization schemes can be tuned to reach the desired level of dispersion and diffusion errors. CFD solution is used as a boundary condition for the CAA computation at the boundaries between CFD and CAA domains of computation. The difficulty of the computational transport methods is in defining of transmission conditions from source region to acoustic domain, because of the change in discretization, resolution and equations.

- **Analytical transport methods**: These methods contain integrated form of acoustic propagation equations: Kirchhoff's equation or Ffowcs Williams - Hawkings (FW-H) equation. Calculation of the sound pressure at the observer's location is conducted by the integration of the source term along a surface (whcih can be a physical surface or a surface that surrounds the aerodynamically active area) and, in the case of FW-H equation,

by additional volume integral. The problem occurs when the velocities reach the speed of sound, because the integrals become highly singular due to Doppler effect.

Taking into account the above described methods and techniques, one can put them all in a scheme shown in Figure 1.2.1.

CAA	Direct methods			
	Hybrid methods	1. CFD analysis		
		2. Sound generation	Resolved sources (DNS, LES, DES)	
			Reconstructed sources (RANS+SNGR/SATIN)	
			Acoustic perturbation equation (APE)	
		3. Transport method	Computational transport	Linearised Euler equation (LEE)
				Wave equation
			Analytical transport	Acoustic analogy (FW-H)
				Kirchhoff integral

Figure 1.2.1: Noise prediction methods.

1.2.3   Numerical Difficulties in Computational Aeroacoustics

Disparity of energy, length and time scales between aerodynamics and aeroacoustics are the major problem of CAA. This is especially the case at lower Mach numbers. The ratio of sound power to mechanical power is of the order $10^{-4}M^5$. As an example, for the case of M=0.1 the ratio becomes 10^{-9} and even for M=0.7 (the case of an airliner) the ratio is 10^{-5}. This implies that almost every CFD simulation introduces artificial noise sources (caused by numerical errors) that would entirely contaminate information about physical sound sources. In aeroacoustics, the discretization techniques must be adjusted in a way that diffusion and dispersion errors reach the lowest possible level [1].

Boundary conditions in CAA require special attention. The outer boundaries, where acoustic waves leave the computational domain, must not cause any reflections, but this is often difficult to achieve. As stated above, CFD solution is used as a boundary condition for the CAA simulation, and there is also a problem of spurious reflections at the interface between CFD and CAA domains.

For further information about boundary conditions in CAA, the reader is referred to [1].

Chapter 2

Theoretical Background

This chapter is organised as follows: In the first section the basic laws of fluid dynamics and constitutive equations will be given. Section 2 deals with free-space acoustics, specifically with the sound measurements, wave equation (with the elementary solutions) and simple acoustic sources. Third section gives an overview of two aeroacoustic analogies.

2.1   Fluid Dynamics

The basic laws of fluid dynamics are written in the following equations:

- mass conservation equation:

$$\frac{\partial \rho}{\partial t} = -\frac{\partial (\rho u_j)}{\partial x_j},\tag{2.1}$$

- momentum conservation equation:

$$\frac{\partial (\rho u_i)}{\partial t} = -\frac{\partial (\rho u_j u_i)}{\partial x_j} + \rho f_i + \frac{\partial \sigma_{ji}}{\partial x_j},\tag{2.2}$$

- energy conservation equation:

$$\frac{\partial (\rho e_T)}{\partial t} = -\frac{\partial (\rho u_j e_T)}{\partial x_j} + \rho f_i u_i + \frac{\partial (\sigma_{ji} u_i)}{\partial x_j} - \frac{\partial q_i}{\partial x_i} + Q_w,\tag{2.3}$$

where ρ denotes density, u_j velocity, t time, x_j position vector, f_i the force field, σ_{ji} stress tensor, e_T total energy per unit mass, q_i heat flux density and Q_w heat production per unit volume.

8

The set of equations (2.1) , (2.2) and (2.3) gives the system of five equations (mass and energy equations are scalar equations, while the momentum equation is a vector equation). The system of equations (2.1) , (2.2) and (2.3) is valid for all fluids, but is not sufficient for complete description of fluid flow due to the inequality of number of equations and the number of unknowns. Of all the fields in the system, only the density of the force field f_i and the heat production per unit of volume Q_w are known, but the other 14 fields are unknown: density ρ, three velocity components v_i, six components of stress tensor σ_{ji}, energy per unit mass e and three components of heat flux q_i.

2.1.1 Constitutive Equations

In order to equalize the number of equations and the number of unknown physical quantities, the constitutive equations are introduced. Due to their introduction the new, expanded, system of equations is no longer applicable to all fluid media, but only to the ones that the constitutive equations are related to. The constitutive relations are:

- Ideal gas law:

$$\frac{p}{\rho} = RT, \tag{2.4}$$

  where R denotes the specific gas constant and t denotes the thermodynamic temperature.

- Caloric equation of state:

$$u = c_v T, \tag{2.5}$$

  where u denotes the internal energy per unit mass and c_v is the specific heat capacity at constant volume.

- The Fourier law:

$$q_i = -\lambda \frac{\partial T}{\partial x_i}, \tag{2.6}$$

  where λ denotes the conductivity.

- Newtonian fluid law:

$$\sigma_{ji} = -p\delta_{ji} + \Sigma_{ji}, \tag{2.7}$$

  where σ_{ji} is the stress tensor, p is the pressure, δ_{ji} is identity tensor and Σ_{ji} is the viscous stress tensor (symmetric).

- Speed of sound:

$$c = \sqrt{\left(\frac{\partial p}{\partial \rho}\right)_s}, \tag{2.8}$$

where the specific entropy s is kept constant due to the fact that sound is defined as isentropic (inviscid and adiabatic) pressure and density perturbations ($ds = 0$).

2.2 Free-Space Acoustics

2.2.1 Sound Measurements

Human ear detects pressure perturbations p' that are usually very small compared to the mean pressure of the fluid. Due to the fact that the range of detectable pressure magnitudes is large, logarithmic scale is used. Quantities which describe the magnitude of sound are:

- Sound pressure level (SPL)

$$\text{SPL} = \ln\left(\frac{p'}{p_{\text{ref}}}\right)\text{Np} = 2\log_{10}\left(\frac{p'}{p_{\text{ref}}}\right)\text{B} = 20\log_{10}\left(\frac{p'}{p_{\text{ref}}}\right)\text{dB}, \tag{2.9}$$

where p' is the root mean square (quadratic mean) sound pressure; p_{ref} is the reference sound pressure (commonly used $= 20\,\mu\text{Pa}$ for gases and $1\,\mu\text{Pa}$ for other media); 1 Np is the neper; $1\,\text{B} = (1/2)\ln(10)$ is the bel; and $1\,\text{dB} = (1/20)\ln(10)$ is the decibel. Most commonly used unit in acoustics is dB.

- Sound intensity level (IL)

  Sound intensity is defined as time-averaged energy flux associated to the acoustic wave. Sound intensity level is defined as:

$$\text{IL} = \frac{1}{2}\ln\left(\frac{I}{I_{\text{ref}}}\right)\text{Np} = \log_{10}\left(\frac{I}{I_{\text{ref}}}\right)\text{B} = 10\log_{10}\left(\frac{I}{I_{\text{ref}}}\right)\text{dB}, \tag{2.10}$$

where I is the sound intensity and I_{ref} is the reference sound intensity (for air $I_{\text{ref}} = 10^{-12}\,\text{W/m}^2$). Reference intensity level is obtained from the relationship $I = p'^2/(\rho_0 c_0)$, where $\rho_0 c_0 = 400\,\text{kgm}^{-2}\text{s}^{-1}$ at ambient conditions.

- Sound power level (PWL):

$$\text{PWL} = \frac{1}{2}\ln\left(\frac{P}{P_{\text{ref}}}\right)\text{Np} = \log_{10}\left(\frac{P}{P_{\text{ref}}}\right)\text{B} = 10\log_{10}\left(\frac{P}{P_{\text{ref}}}\right)\text{dB}, \tag{2.11}$$

where P is the sound power and P_{ref} is the reference power (takes value 10^{-12} W and corresponds to the power flowing through a surface of $1\,\text{m}^2$ with an intensity I_{ref}).

Human ear can detect sound in the audio range of

$$20\text{Hz} \leqslant f \leqslant 20\,\text{kHz}, \tag{2.12}$$

where f denotes the frequency.

For good hearing system the threshold of hearing at 1kHz is around SPL = 0 dB. Table 2.1 shows the sound intensity levels for some common sounds from everyday life.

Source	Sound Intensity (W/m^2)	Sound Intensity Level (dB)
Threshold of Hearing	1×10^{-12}	0
Rustling Leaves	1×10^{-11}	10
Whisper	1×10^{-10}	20
Normal Conversation	1×10^{-6}	60
Busy Street Traffic	1×10^{-5}	70
Vacuum Cleaner	1×10^{-4}	80
Large Orchestra	6.3×10^{-3}	98
Walkman at Maximum Level	1×10^{-2}	100
Front Rows of Rock Concert	1×10^{-1}	110
Threshold of Pain	1×10^{1}	130
Military Jet Takeoff	1×10^{2}	140
Instant Perforation of Eardrum	1×10^{4}	160

Table 2.1: Table of intensity levels and intensities of common sounds [28].

2.2.2 Approximations of Sound Propagation Equations

Even at the threshold of pain (SPL$\approx 140\,$dB) the relative pressure fluctuations are of the order $p'/p_0 = \mathscr{O}(10^{-3})$, where subscript 0 denotes atmospheric conditions. The same order of

magnitude applies to density fluctuations ρ' according to the relation

$$\frac{\rho'}{\rho_0} = \frac{p'}{\rho_0 c_0^2} = \frac{p'}{\dfrac{\rho_0 c_0^2}{p_0} \cdot p_0} = \frac{p'}{\gamma \cdot p_0}, \tag{2.13}$$

where $\gamma = \frac{c_p}{c_v} = 1.4$ is the heat capacity ratio and c_p is specific heat capacity at constant pressure. The fact that both variables (p' and ρ') are about three orders of magnitude times smaller than the mean values justifies the linearisation of the equations and illustrates the difficulty of acoustics within a conventional CFD framework.

Beside linearisation, further approximation can be introduced by neglecting friction and heat transfer. The expression for the unsteady Reynolds number yields

$$\text{Re}_{\text{unst}} = \frac{\lambda^2 f}{\nu}, \tag{2.14}$$

where λ is the wavelength of the acoustic wave and ν is the kinematic viscosity. For air $\nu = 1.5 \cdot 10^{-5} \text{m}^2/\text{s}$ and $c \approx 340$ m/s at $f = 1$ kHz, and since $\lambda = c/f$, it is obtained

$$\text{Re}_{\text{unst}} = \frac{c^2}{f\nu} = \mathcal{O}(10^7). \tag{2.15}$$

From this result, it can be concluded that viscosity plays a minor role in close proximity and only on large distances it cannot be neglected. For gases the Prandtl number is $\text{Pr} = \mathcal{O}(1)$, indicating that heat transfer is also negligible [1].

However, in the case of high frequencies, these approximations can no longer be applied. Attenuation effects are much larger in this case (at large distances, only low-frequency sounds can be heard) [1].

2.2.3 Wave Equation

To account for the wave propagation the field variable perturbation propagation is considered. The field variables are decomposed into the perturbation part (p', ρ', s', $\mathbf{v}'$) and mean reference part ($\bar{p}$, $\bar{\rho}$, $\bar{s}$, $\bar{\mathbf{v}}$). The perturbations of field variables are defined by

$$\begin{aligned}
p' &= p - \bar{p}, \\
\rho' &= \rho - \bar{\rho}, \\
s' &= s - \bar{s}, \\
\mathbf{v}' &= \mathbf{v} - \bar{\mathbf{v}},
\end{aligned} \tag{2.16}$$

where s denotes entropy per unit mass. Due to low perturbation values, compared to mean reference values, the equations (2.1), (2.2) and (2.3) are linearised and the heat transfer and viscous effects are also neglected:

$$\frac{\partial \rho'}{\partial t} + \bar{\rho} \, \nabla \cdot \mathbf{v}' = 0, \tag{2.17}$$

$$\bar{\rho} \frac{\partial \mathbf{v}'}{\partial t} + \nabla p' = \mathbf{f}, \tag{2.18}$$

$$\bar{\rho}\bar{T} \frac{\partial s'}{\partial t} = Q_w. \tag{2.19}$$

In addition, the constitutive equation (2.8) can be written as follows:

$$p' = c^2 \rho' + \left(\frac{\partial p}{\partial s} \right)_{\rho} s'. \tag{2.20}$$

From the Equations (2.17), (2.18), (2.19) and (2.20) the non-homogeneous wave equation can be derived [1]:

$$\frac{1}{c^2} \frac{\partial^2 p'}{\partial t^2} - \nabla^2 p' = q, \tag{2.21}$$

where q is equal to

$$q = \frac{(\partial p / \partial s)_{\rho}}{\bar{\rho} c^2 \bar{T}} \frac{\partial Q_w}{\partial t} - \nabla \cdot \mathbf{f}. \tag{2.22}$$

The first term on the right-hand side of eq. (2.22) corresponds to the dilatation of the fluid as a result of heat production (e.g. combustion, condensation). The second term corresponds to the sound production by an unsteady and nonuniform external force field. By its nature, this is a wave equation with sources, recognised by the second temporal derivative of p' and the laplacian term.

2.2.4 Elementary Solutions of the Wave Equation

Homogeneous form of the wave equation ($q = 0$) yields

$$\frac{1}{c_0^2} \frac{\partial^2 p'}{\partial t^2} - \nabla^2 p' = 0. \tag{2.23}$$

Two elementary solutions will be described: the plane wave and the spherical symmetric wave. The wave is considered to be in *free space* conditions, meaning that the fluid is not bounded by any walls or obstacles. In both cases the wave is generated by boundary or initial condition.

2.2.4.1 Plane wave

Plane waves are uniform in any plane normal to the direction of wave propagation. If the wave propagates in x_1 direction, equation (2.23) reduces to one-dimensional equation:

$$\frac{1}{c_0^2}\frac{\partial^2 p'}{\partial t^2} - \frac{\partial^2 p'}{\partial x_1^2} = 0, \tag{2.24}$$

where $p' = p'(x_1, t)$.

The solution of the equation (2.24) is called the solution of d'Alembert [1] and yields

$$p' = F\left(t - \frac{x_1}{c_0}\right) + G\left(t + \frac{x_1}{c_0}\right), \tag{2.25}$$

where F describes wave propagation in positive x_1 direction, whereas G represents wave propagation in negative direction. The more general form of the equation (2.25) yields

$$p' = F\left(t - \frac{\mathbf{n}\cdot\mathbf{x}}{c_0}\right), \tag{2.26}$$

where $\mathbf{n}$ is the unit vector which defines the direction of wave propagation. The plane wave can also be written in complex form:

$$p' = \hat{p}e^{i\omega t - i\mathbf{k}\cdot\mathbf{x}}, \tag{2.27}$$

where $\mathbf{k} = k\mathbf{n}$ represents the wave number vector.

2.2.4.2 Spherically Symmetric Wave

In this case, the sound pressure is the function of distance to the origin r, and time t: $p' = p'(r, t)$. The waves are uniform along the constant radius of the sphere. The wave equation (2.23) reduces to the form

$$\frac{1}{c_0^2}\frac{\partial^2 p'r}{\partial t^2} - \frac{\partial^2 p'r}{\partial r^2} = 0, \tag{2.28}$$

for every $r > 0$.

Solution of d'Alembert for spherically symmetric wave propagation equation yields

$$p' = \frac{1}{r}\cdot\left[F\left(t - \frac{r}{c_0}\right) + G\left(t + \frac{r}{c_0}\right)\right], \tag{2.29}$$

where F represents waves going outward and G waves going toward the source. In free field conditions there are no incoming waves, which is described through $G = 0$, but only outgoing waves. Written in complex form, the solution reads:

$$p' = \frac{A}{r}e^{i\omega t - ikr}, \tag{2.30}$$

where A is the amplitude and $k = \omega/c_0$ the wave number.

2.2.4.3 Simple acoustic sources: Monopoles, Dipoles and Quadrupoles

Spherical symmetric wave going outwards from the source is often called **monopole sound field**, Figure 2.2.1 a). For example, acoustic monopole can be a small sphere with a pulsating radius a:

$$a = a_0 + \hat{a}e^{i\omega t}. \tag{2.31}$$

The pressure radiated by a monopole may be written as

$$p' = -\frac{\rho_0 \omega^2 a_0 \hat{a}}{1 + ika_0} \frac{a_0}{r} e^{i\omega t - ik(r-a_0)}. \tag{2.32}$$

In the far-field the equation (2.32) reduces to

$$p' = i\frac{\omega \rho_0 \Phi_V}{4\pi r} e^{i\omega t - ik(r-a_0)}, \tag{2.33}$$

by substituting $\Phi_V = 4\pi a_0^2 v_r'(a_0) = 4\pi i a_0^2 \omega \hat{a}$ [1]. Acoustic monopole sound field occurs when a net mass flux (or volume source) is present in the fluid media. If the source region is small compared with the acoustic wavelength (the source field is compact), the monopole field will be dominant.

The first-order spatial derivative of the monopole field is called a **dipole field**. The far-field expression for the pressure radiated by an acoustic dipole may be written as

$$p' = -i\frac{\omega \rho_0 \Phi_V}{4\pi r} \cdot kd \cdot \cos\theta \cdot e^{i\omega t - ik(r-a_0)}. \tag{2.34}$$

The acoustic dipole can also be described as two monopoles of equal source strength, but opposite phase, and separated by a small distance d, Figure 2.2.1 b). A dipole does not radiate equally in all direction as a monopole does. The acoustic dipole field occurs when there is net momentum introduced into the fluid. In fact, it is the force acting on the fluid which causes energy to be radiated from the source. For example, the rigid sphere oscillating in one direction creates a dipole acoustic field. It can noticed that there is no volume source present in the fluid for the dipole.

A quadrupole source consists of two identical dipoles, with opposite phase and separated by a small distance. In this case there is no net flux of fluid and no net force acting on the fluid. In this case the sound waves are generated by fluctuating stress. There are two kinds of quadrupoles: *longitudinal source* and *lateral source*, shown in Figure 2.2.2. The far-field sound
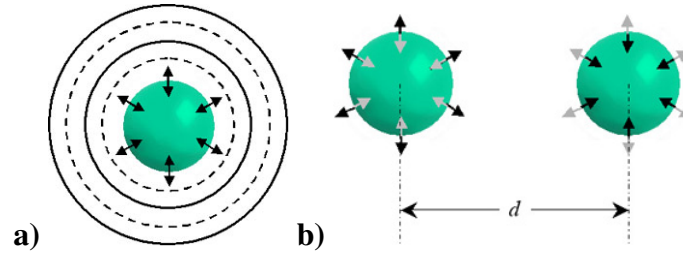
Figure 2.2.1: a) Monopole sound source, b) Dipole sound source, [29].
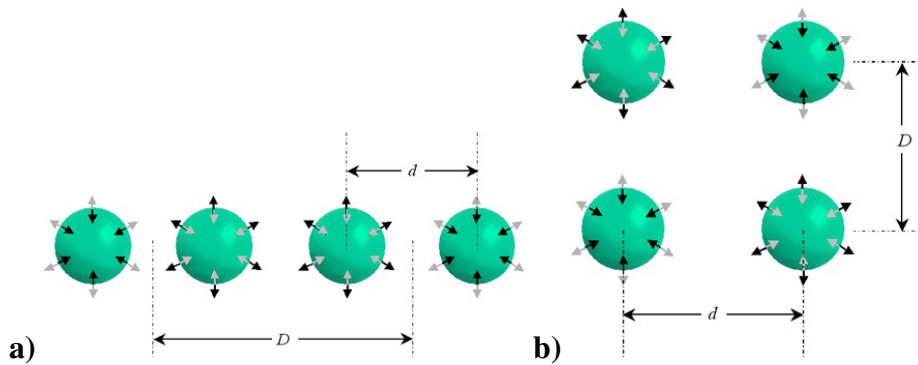
Figure 2.2.2: The two kinds of quadrupoles: a) Longitudinal quadrupole source; b) Lateral quadrupole source, [29].

pressure amplitude produced by a lateral quadrupole is given by equation

$$|p'| = \frac{\omega \rho_0 \Phi_V}{4\pi r} \cdot 4k^2 dD \cdot \cos\theta \sin\theta. \tag{2.35}$$

There are four directions where sound is radiated well, as well as four directions where destructive interference occurs and no sound is radiated (see Figure 2.2.3).

The far-field sound pressure amplitude produced by a longitudinal quadrupole yields

$$|p'| = \frac{\omega \rho_0 \Phi_V}{4\pi r} \cdot 4k^2 dD \cdot \cos^2\theta. \tag{2.36}$$

The field of the longitudinal quadrupole looks similar to the one of the dipole. Figure 2.2.3 shows monopole, dipole and both of the quadrupole sources, with contour lines for the sound pressure level in the far-field (thick line).
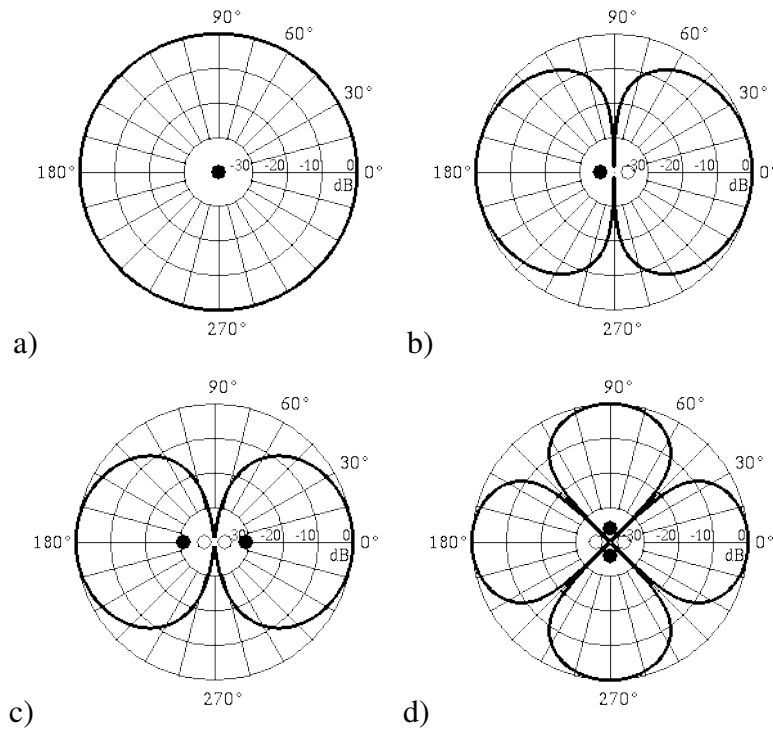
Figure 2.2.3: Simple acoustic sources: a) monopole, b) dipole, c) longitudinal quadrupole, d) lateral quadrupole.

2.3 Aeroacoustic Analogies

2.3.1 Lighthill's Analogy

In 1952 Sir James Lighthill has proposed an approach of predicting acoustic quantities in the far field that he named an *acoustic analogy*. The idea was to reformulate the general equations of gas dynamics (2.1) and (2.2), in order to derive a wave equation. He chose the density fluctuation as the featured variable, because of the fact that acoustic waves occur due to compressibility.

The derivation of the Lighthill's equation begins with the mass conservation equation:

$$\frac{\partial \rho}{\partial t} + \frac{\partial (\rho u_i)}{\partial x_i} = 0 \tag{2.37}$$

and the momentum conservation equation:

$$\frac{\partial (\rho u_i)}{\partial t} + \frac{\partial (\rho u_i u_j)}{\partial x_j} = -\frac{\partial p}{\partial x_i} + \frac{\partial \sigma_{ij}}{\partial x_j}. \tag{2.38}$$

After differentiating Equation (2.37) with respect to time and taking the divergence of Equa-

tion (2.38) and after subtracting the latter from the former, the following equation is obtained:

$$\frac{\partial^2 \rho}{\partial t^2} - \frac{\partial^2 (\rho u_i u_j)}{\partial x_i \partial x_j} = \frac{\partial p}{\partial x_j} - \frac{\partial \sigma_{ij}}{\partial x_i \partial x_j}. \tag{2.39}$$

Taking Equation (2.39) and subtracting the term $c_0^2 \frac{\partial^2 \rho}{\partial x_j^2}$ from both sides, a hyperbolic partial differential equation is obtained:

$$\frac{\partial^2 \rho}{\partial t^2} - c_0^2 \frac{\partial^2 \rho}{\partial x_j^2} = \frac{\partial^2 (\rho u_i u_j)}{\partial x_i \partial x_j} - \frac{\partial^2 \sigma_{ij}}{\partial x_i \partial x_j} + \frac{\partial^2}{\partial x_j^2} (p - c_0^2 \rho). \tag{2.40}$$

It is obvious that the Equation (2.40) represents a non-homogeneous wave equation and is called the *analogy* of Lighthill. The right-hand side of the equation can be written as

$$\frac{\partial^2 T_{ij}}{\partial x_i \partial x_j} = \frac{\partial^2}{\partial x_i \partial x_j} (\rho u_i u_j - \sigma_{ij} + (p - c_0^2 \rho) \delta_{ij}), \tag{2.41}$$

where

$$T_{ij} = \rho u_i u_j - \sigma_{ij} + (p - c_0^2 \rho) \delta_{ij} \tag{2.42}$$

denotes the *Lighthill stress* tensor.

During the derivation of the Equation (2.40) no approximations were introduced, so the equation is exact. The derivation started with four equations (one for mass conservation and three for momentum conservation) and resulted with only one equation, but the number of the unknowns remained unchanged ($u_i, p, \rho, \sigma_{ij}$). In order to make the *analogy* useful, the approximations that carry new information have to be introduced.

The first approximation is the assumption of linear acoustic perturbations, already described in Section 2.2.3. In the far field (where the listener is located) the assumption of linear disturbances of acoustic quantities is valid in most cases.

Other assumptions are related to the approximations of the source terms (right-hand side of Lighthill equation (2.40)). The first term of Lighthill stress tensor $\rho u_i u_j$ represents the Reynolds stress and takes into account the nonlinear convection of momentum. The second term σ_{ij} represents the viscous stress that is induced by molecular transport of momentum. The last term $(p - c_0^2 \rho) \delta_{ij}$ is recognised as an entropy production term and represents all effects due to entropy non-homogenities.

Some authors prefer to use the pressure as a reference variable instead of the density and, in that case, the Lighthill equation takes the following form:

$$\frac{1}{c_0^2}\frac{\partial^2 p}{\partial t^2} - \frac{\partial^2 p}{\partial x_j^2} = \frac{\partial^2}{\partial x_i \partial x_j}(\rho u_i u_j + \frac{1}{c_0^2}\frac{\partial^2}{\partial t^2}(p - c_0^2\rho - \sigma_{ij})). \tag{2.43}$$

.

All three distinct categories of sound sources can be recognised in the right-hand side of Equation (2.43):

- monopole sources, $\frac{\partial^2}{\partial t^2}p$,

- dipole sources, $-\frac{\partial^2}{\partial t^2}(c_0^2\rho)$, and

- quadrupole sources, $\frac{\partial^2}{\partial x_i \partial x_j}(\rho u_i u_j)$.

Additional approximations can be introduced through the source terms. For large Reynolds numbers, the viscous stress is negligible compared to the Reynolds stress. Then, assuming small fluctuating Mach numbers ($|U'|/c_0 \ll 1$, i.e. linear disturbances) the entropy term is also negligible compared to Reynolds stress. Taking into account the above approximations, the Lighthill stress tensor takes the simplified form:

$$T_{ij} \approx \rho u_i u_j, \tag{2.44}$$

so the Lighthill equation now yields

$$\frac{1}{c_0^2}\frac{\partial^2 p'}{\partial t^2} - \frac{\partial^2 p'}{\partial x_j^2} = \frac{\partial^2 \rho u_i u_j}{\partial x_i \partial x_j}. \tag{2.45}$$

Further assumption is that the reaction from the acoustic field to the source is negligible. Thus, the source field can be calculated separately from the acoustic field. The analogy is valid only if the sound is radiated into free space.

The integral formulation of Lighthill's analogy was first derived by Curle in the following form:

$$\rho'(\mathbf{x},t) = \rho(\mathbf{x},t) - \rho_0 =$$
$$\frac{1}{4\pi c_0^2}\frac{\partial^2}{\partial x_i \partial x_j}\int_V \frac{T_{ij}(\mathbf{y}, t - \frac{R}{c_0})}{R}dV(\mathbf{y}) + \frac{1}{4\pi c_0^2}\frac{\partial}{\partial x_i}\int_S \frac{l_j P_{ij}(\mathbf{y}, t - \frac{R}{c_0})}{R}dS(\mathbf{y}), \tag{2.46}$$

which is often called the Curle analogy, which takes solid and fixed surfaces into consideration. In Equation (2.46), $\mathbf{x}$ is the acoustic observation point, $\mathbf{y}$ is the point in the flow field where sound is generated, $R = |\mathbf{x} - \mathbf{y}|$, usually $|\mathbf{x}| \gg |\mathbf{y}|$, l_j is the unit direction vector of the solid boundary, pointing toward the fluid and t is the time measured at $\mathbf{x}$.

2.3.2   Ffowcs Williams - Hawkings (FW-H) Analogy

Whereas the Curle formulation allows only fixed control surface, the Ffowcs Williams - Hawkings (FW-H) formulation allows the use of moving control surfaces, e.g. a rotor. FW-H analogy generalises Lighthill's acoustic analogy so that the linear wave operator (that is, the whole left-hand side of the Equation (2.45)) remains the same and only the source terms on the right-hand side change:

$$S = \frac{\partial^2}{\partial x_i \partial x_j} T_{ij} H(f) - \frac{\partial}{\partial x_i}[P_{ij}n_j + \rho u_i(u_n - v_n)]\delta(f) + \frac{\partial}{\partial t}[\rho_0 v_n + \rho(u_n - v_n)]\delta(f), \quad (2.47)$$

where u_i denotes fluid velocity component in the x_i direction, u_n fluid velocity component normal to the surface $(f = 0)$, v_i surface velocity components in the x_i direction, v_n surface velocity component normal to the surface, $\delta(f)$ Dirac delta function, $H(f)$ Heaviside function, $P_{ij} = p\delta_{ij} - \sigma_{ij}$ is compressive stress tensor and T_{ij} is the Lighthill stress tensor in the full form:

$$T_{ij} = \rho u_i u_j + P_{ij} - c_0^2(\rho - \rho_0)\delta_{ij}, \quad (2.48)$$

f is a smooth function that takes the following values:

$$\begin{aligned} f(\mathbf{x},t) &< 0 \text{ if } \mathbf{x} \in B(t), \\ f(\mathbf{x},t) &= 0 \text{ if } \mathbf{x} \in S(t), \\ f(\mathbf{x},t) &> 0 \text{ outside } B(t), \end{aligned} \quad (2.49)$$

where $B(t)$ describes the volume enclosed by the surface $S(t)$.

The solution of the equation is obtained using the free-space Green function

$$4\pi p'(\mathbf{x},t) =$$
$$\frac{x_i x_j}{|\mathbf{x}|^3 c_0^2} \frac{\partial^2}{\partial t^2}\left[\int_V T_{ij} H dV\right] + \frac{x_j}{|\mathbf{x}|^2 c_0} \frac{\partial}{\partial t}\left[\int_S p'n_j + \rho u_j u_n ds\right] + \frac{1}{|\mathbf{x}|c_0} \frac{\partial}{\partial t}\left[\int_S \rho u_n ds\right]. \quad (2.50)$$

In the literature lots of different formulations of the FW-H analogy can be found. Equation (2.50) represents the Farassat's formulation 1 [5].

Surface *s* can describe either physical surfaces, such as a wing or a landing gear, or arbitrary control surfaces. The difficulty with the FW-H approach is enclosing all the sound sources by *s*. In the case of a plane jet, the eddies convect downstream and pass through the surface *s*. The example of FW-H surface is shown in Figure 2.3.1.
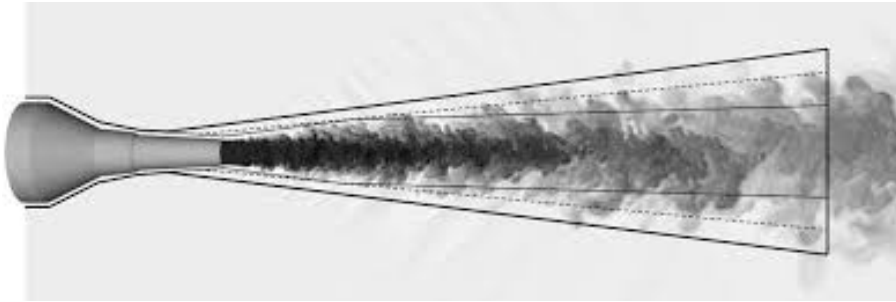
Figure 2.3.1: Example of FW-H surface surrounding the jet [30].

All integral methods (which is another name for aeroacoustic analogies) use a theoretical solution of the wave equation in their integral solutions. Hence a downside that is common to all analogies can be identified: Integral methods cannot account for changes in the speed of sound or the mean reference flow field between the source of sound and the observer, because they use a theoretical solution of the wave equation. Therefore, to accurately predict the acoustic field in cases of non-homogeneous mean flow field, which is often in real situations, other methods have been developed, such as the Linearised Euler Equations (LEEs), which are derived in the following chapter.

Chapter 3

Linearised Euler Equations

In the previous chapter the aeroacoustic analogies have been presented. Since they cannot account for the changes of the mean reference flow, other methods of predicting the acoustic field have to be used in order to overcome that problem, such as the Linearised Euler Equations (LEEs).

There are different ways of deriving the LEEs, all originating from the Euler equations. In the literature there are variety of different sets of equations under the name of linearized Euler equations. The reason for this could lie in different forms of Euler equations before introducing linearization [6]. Euler equations can be written in conservative and non-conservative form. Moreover, variables in Euler equations can be conservative and primitive. The form of the linearised Euler equations used in this study uses conservative variables in the conservative formulation and is the identical to the set "*formulation 2*" in the work of Blom [6].

As stated in Section 2.2.2, in sound propagation, the viscous effects are negligible and the isentropic assumption is justified. Neglecting viscous terms in Navier-Stokes equations the Euler equations are obtained. Written in the conservative form, Euler equations yield

$$\frac{\partial \rho}{\partial t} + \frac{\partial (\rho u_j)}{\partial x_j} = 0, \tag{3.1}$$

$$\frac{\partial (\rho u_i)}{\partial t} + \frac{\partial (\rho u_i u_j + p \delta_{ij})}{\partial x_j} = 0, \tag{3.2}$$

$$\frac{\partial (\rho e + \frac{1}{2}\rho u_i u_i)}{\partial t} + \frac{\partial (\rho e u_j + \frac{1}{2}\rho u_i u_i u_j + p u_j)}{\partial x_j} = 0, \tag{3.3}$$

where Equations (3.1), (3.2) and (3.3) represent the conservation of mass, momentum and energy respectively. In Equation (3.3) $e = c_v T$ represents internal energy per unit mass.

In this chapter, the first section gives the derivation of the non-conservative form of Euler equations and the semi-conservative form of energy equation. In the second section the derivation of the linearised Euler equations used in this thesis, as well as the non-conservative form of the LEEs are presented. In the same section the acoustic equations for the quiescent fluid are obtained. Third section deals with the boundary conditions in CAA. In the fourth section, one method for predicting the sound sources is presented.

In the following section, the non-conservative form of Euler equations and the semi-conservative form of energy equation are derived.

3.1 Non-conservative Form of Governing Equations

3.1.1 Conservation of Mass

Starting with the Equation (3.1) and applying the chain rule the non-conservative form of the mass conservation equation is obtained

$$\frac{\partial \rho}{\partial t} + \rho \frac{\partial u_j}{\partial x_j} + u_j \frac{\partial \rho}{\partial x_j} = 0. \tag{3.4}$$

3.1.2 Conservation of Momentum

Applying the same procedure to Equation (3.2) as in Equation (3.4) and after rearrangement of terms, one obtains

$$u_i \left(\frac{\partial \rho}{\partial t} + \rho \frac{\partial u_j}{\partial x_j} + u_j \frac{\partial \rho}{\partial x_j} \right) + \rho \frac{\partial u_i}{\partial t} + \rho u_j \frac{\partial u_i}{\partial x_j} + \frac{\partial p}{\partial x_i} = 0. \tag{3.5}$$

Terms inside parentheses can be identified as Equation (3.4) and are equal to zero. Finally, conservation of momentum in non-conservative form reads

$$\rho \frac{\partial u_i}{\partial t} + \rho u_j \frac{\partial u_i}{\partial x_j} + \frac{\partial p}{\partial x_i} = 0. \tag{3.6}$$

3.1.3 Conservation of Energy

Taking the Equation (3.3) and applying the chain rule one obtains

$$\rho \frac{\partial e}{\partial t} + e \frac{\partial \rho}{\partial t} + \rho e \frac{\partial u_j}{\partial x_j} + \rho u_j \frac{\partial e}{\partial x_j} + e u_j \frac{\partial \rho}{\partial x_j} + p \frac{\partial u_j}{\partial x_j} + u_j \frac{\partial p}{\partial x_j} +$$
$$+ \frac{1}{2} \left[2\rho u_i \frac{\partial u_i}{\partial t} + u_i u_i \frac{\partial \rho}{\partial t} + \rho u_i u_i \frac{\partial u_j}{\partial x_j} + 2\rho u_i u_j \frac{\partial u_i}{\partial x_j} + u_i u_i u_j \frac{\partial \rho}{\partial x_j} \right] = 0 \tag{3.7}$$

and after rearrangement of terms in Equation (3.7), it can be written as

$$e \left(\frac{\partial \rho}{\partial t} + \rho \frac{\partial u_j}{\partial x_j} + u_j \frac{\partial \rho}{\partial x_j} \right) + \rho \frac{\partial e}{\partial t} + \rho u_j \frac{\partial e}{\partial x_j} + p \frac{\partial u_j}{\partial x_j} + u_j \frac{\partial p}{\partial x_j} +$$
$$+ u_i \left(\rho \frac{\partial u_i}{\partial t} + \rho u_j \frac{\partial u_i}{\partial x_j} \right) + \frac{1}{2} u_i u_i \left(\frac{\partial \rho}{\partial t} + \rho \frac{\partial u_j}{\partial x_j} + u_j \frac{\partial \rho}{\partial x_j} \right) = 0. \tag{3.8}$$

Note that the terms in the second rows of Equation (3.7) and Equation (3.8) are equal to

$$\frac{1}{2} \left[2\rho u_i \frac{\partial u_i}{\partial t} + u_i u_i \frac{\partial \rho}{\partial t} + \rho u_i u_i \frac{\partial u_j}{\partial x_j} + 2\rho u_i u_j \frac{\partial u_i}{\partial x_j} + u_i u_i u_j \frac{\partial \rho}{\partial x_j} \right] =$$
$$\frac{1}{2} \frac{\partial (\rho u_i u_i)}{\partial t} + \frac{1}{2} \frac{\partial (\rho u_i u_i u_j)}{\partial x_j}. \tag{3.9}$$

The terms in the first and last pair of parentheses of the Equation (3.8) are the same and represent the equation for conservation of mass (Equation (3.4)) and are, therefore, equal to zero. Terms in second pair of parentheses are equal to $-\frac{\partial p}{\partial x_i}$ according to equation (3.6). Taking this into account, entire second row of Equation (3.8) adds up to

$$-u_i \frac{\partial p}{\partial x_i}, \tag{3.10}$$

which is also equal to

$$\frac{1}{2} \frac{\partial (\rho u_i u_i)}{\partial t} + \frac{1}{2} \frac{\partial (\rho u_i u_i u_j)}{\partial x_j}, \tag{3.11}$$

according to Equation (3.9).

Terms (3.11), that are involved in Equation (3.3) represent the temporal and spatial derivative of the kinetic energy, where the following identity has been used

$$\frac{1}{2} \frac{\partial (\rho u_i u_i)}{\partial t} + \frac{1}{2} \frac{\partial (\rho u_i u_i u_j)}{\partial x_j} = -u_i \frac{\partial p}{\partial x_i} \tag{3.12}$$

After subtraction of terms in Equation (3.8), the non-conservative form of equation for conservation of energy yields

$$\rho \frac{\partial e}{\partial t} + \rho u_j \frac{\partial e}{\partial x_j} + p \frac{\partial u_j}{\partial x_j} = 0. \tag{3.13}$$

3.1.3.1 Semi-conservative Form of the Energy Equation

In order to obtain the system of equations which contains unknown variables (ρ', u', v', w' and p'), the energy equation has to be expressed with p as the unknown variable, instead of e. If one considers the expression for heat capacity ratio

$$\gamma = \frac{c_p}{c_v} \tag{3.14}$$

and Mayer's relation

$$R = c_p - c_v, \tag{3.15}$$

the substitution of variables is introduced via

$$e = c_v T = \frac{R}{\gamma - 1} T \tag{3.16}$$

The conservative form of energy equation (3.3) can now be written as

$$\frac{1}{\gamma - 1}\frac{\partial p}{\partial t} + \frac{1}{2}\frac{\partial(\rho u_i u_i)}{\partial t} + \frac{1}{\gamma - 1}\frac{\partial(p u_j)}{\partial x_j} + \frac{1}{2}\frac{\partial(\rho u_i u_i u_j)}{\partial x_j} + \frac{\partial(p u_j)}{\partial x_j} = 0. \tag{3.17}$$

One can identify terms (3.11) in Equation (3.17), so after introducing the indentity (3.12) and rearranging one obtains

$$\frac{\partial p}{\partial t} + \frac{\partial(p u_j + \gamma p u_j)}{\partial x_j} - p\frac{\partial u_j}{\partial x_j} - \gamma u_j\frac{\partial p}{\partial x_j} = 0. \tag{3.18}$$

Note that the above equations are written for total, non-decomposed field variables.

3.2 Derivation of the Linearised Euler Equations

3.2.1 Conservation of Mass

The Equation (3.1) written with decomposed field variables (equations (2.16)) yields

$$\frac{\partial \bar{\rho}}{\partial t} + \frac{\partial \rho'}{\partial t} + \frac{\partial}{\partial x_j}\left(\bar{\rho}\bar{u}_j + \bar{\rho}u'_j + \rho'\bar{u}_j + \rho'u'_j\right) = 0. \tag{3.19}$$

One can note that the Equation (3.19) contains mean, first-order and second-order terms. If only the mean terms are isolated, one obtains the mean equation. Acoustic equation for conservation of mass is obtained by subtracting the mean equation from decomposed overall Equation (3.19) and reads

$$\frac{\partial \rho'}{\partial t} + \frac{\partial}{\partial x_j}\left(\bar{\rho}u'_j + \rho'\bar{u}_j + \rho'u'_j\right) = 0 \tag{3.20}$$

The acoustic equation for conservation of mass in form (3.20) is non-linear and contains a term $\frac{\partial(\rho'u'_j)}{\partial x_j}$ which is difficult to model. Johnson et al. [7] made a quantitative analysis which has shown that all second and higher order terms can be omitted due to the fact that they are much smaller than the first order terms. Retaining only first order terms, or in other words, *linearising* Equation (3.20), a linearized equation is obtained:

$$\frac{\partial \rho'}{\partial t} + \frac{\partial}{\partial x_j}\left(\bar{\rho}u'_j + \rho'\bar{u}_j\right) = 0. \tag{3.21}$$

3.2.2   Conservation of Momentum

Applying the same procedure as in derivation of linearised form of acoustic equation for conservation of mass (3.21), Equation (3.2) is written in terms of decomposed field variables:

$$\frac{\partial(\bar{\rho}\bar{u}_i)}{\partial t} + \frac{\partial(\bar{\rho}u_i')}{\partial t} + \frac{\partial(\rho'\bar{u}_i)}{\partial t} + \frac{\partial(\rho'u_i')}{\partial t} +$$

$$\frac{\partial}{\partial x_j}\left(\bar{\rho}\bar{u}_i\bar{u}_j + \bar{\rho}\bar{u}_iu_j' + \bar{\rho}u_i'\bar{u}_j + \bar{\rho}u_i'u_j' + \rho'\bar{u}_i\bar{u}_j + \rho'\bar{u}_iu_j' + \rho'u_i'\bar{u}_j + \rho'u_i'u_j' + \bar{p}\delta_{ij} + p'\delta_{ij}\right) = 0.$$

$$(3.22)$$

Subtracting the mean equation from decomposed overall Equation (3.22), the acoustic equation reads

$$\frac{\partial\bar{\rho}u_i'}{\partial t} + \frac{\partial\rho'\bar{u}_i}{\partial t} + \frac{\partial\rho'u_i'}{\partial t} +$$

$$\frac{\partial}{\partial x_j}\left(\bar{\rho}\bar{u}_iu_j' + \bar{\rho}u_i'\bar{u}_j + \bar{\rho}u_i'u_j' + \rho'\bar{u}_i\bar{u}_j + \rho'\bar{u}_iu_j' + \rho'u_i'\bar{u}_j + \rho'u_i'u_j' + p'\delta_{ij}\right) = 0. \qquad (3.23)$$

Neglecting second and higher-order terms in Equation (3.23), a linearised form is obtained

$$\frac{\partial(\bar{\rho}u_i')}{\partial t} + \frac{\partial(\rho'\bar{u}_i)}{\partial t} + \frac{\partial}{\partial x_j}\left(\bar{\rho}\bar{u}_iu_j' + \bar{\rho}u_i'\bar{u}_j + \rho'\bar{u}_i\bar{u}_j + p'\delta_{ij}\right) = 0. \qquad (3.24)$$

The Equation (3.24) can be rearranged in the following form

$$\frac{\partial(\bar{\rho}u_i')}{\partial t} + \frac{\partial}{\partial x_j}\left(\bar{\rho}\bar{u}_ju_i' + p'\delta_{ij}\right) + \frac{\partial(\rho'\bar{u}_i)}{\partial t} + \frac{\partial}{\partial x_j}\left(\bar{\rho}\bar{u}_iu_j' + \rho'\bar{u}_i\bar{u}_j\right) = 0. \qquad (3.25)$$

Expanding last two terms, one obtains

$$\frac{\partial(\rho'\bar{u}_i)}{\partial t} + \frac{\partial}{\partial x_j}\left(\bar{\rho}\bar{u}_iu_j' + \rho'\bar{u}_i\bar{u}_j\right) =$$

$$\rho'\frac{\partial\bar{u}_i}{\partial t} + \bar{u}_i\frac{\partial\rho'}{\partial t} + \bar{\rho}u_j'\frac{\partial\bar{u}_i}{\partial x_j} + \bar{\rho}\bar{u}_i\frac{\partial u_j'}{\partial x_j} + \bar{u}_iu_j'\frac{\partial\bar{\rho}}{\partial x_j} + \rho'\bar{u}_j\frac{\partial u_i}{\partial x_j} + \rho'\bar{u}_i\frac{\partial\bar{u}_j}{\partial x_j} + \bar{u}_i\bar{u}_j\frac{\partial\rho'}{\partial x_j} =$$

$$\rho'\frac{\partial\bar{u}_i}{\partial t} + \bar{\rho}u_j'\frac{\partial\bar{u}_i}{\partial x_j} + \rho'\bar{u}_j\frac{\partial u_i}{\partial x_j} + \bar{u}_i\left(\frac{\partial\rho'}{\partial t} + \bar{\rho}\frac{\partial u_j'}{\partial x_j} + u_j'\frac{\partial\bar{\rho}}{\partial x_j} + \bar{u}_j\frac{\partial\rho'}{\partial x_j} + \rho'\frac{\partial\bar{u}_j}{\partial x_j}\right) = \qquad (3.26)$$

$$\rho'\cancel{\frac{\partial\bar{u}_i}{\partial t}} + \bar{\rho}u_j'\frac{\partial\bar{u}_i}{\partial x_j} + \rho'\bar{u}_j\frac{\partial\bar{u}_i}{\partial x_j} + \bar{u}_i\left(\cancel{\frac{\partial\rho'}{\partial t} + \frac{\partial}{\partial x_j}\left(\bar{\rho}u_j' + \rho'\bar{u}_j\right)}^{\,0}\right)$$

It can be noticed that the expression enclosed by parentheses in bottom line of Equation (3.26) corresponds to equation for conservation of mass (3.21). Moreover, the first term in the same line can also be omitted because it contains the time derivative of a mean quantity. This is justified by the fact that mean quantities change very slowly compared to fluctuation ones.

Taking into account Equation (3.26), Equation (3.25) is written as

$$\frac{\partial(\bar{\rho}u_i')}{\partial t} + \frac{\partial}{\partial x_j}\left(\bar{\rho}\bar{u}_j u_i' + p'\delta_{ij}\right) + \left(\bar{\rho}u_j' + \rho'\bar{u}_j\right)\frac{\partial \bar{u}_i}{\partial x_j} = 0. \tag{3.27}$$

3.2.3   Conservation of Energy

Analogous procedure as in previous examples is also applied here. Starting with equation for pressure (3.18) and after introducing decomposed variables, subtracting the mean equation from decomposed overall equation and omitting second and higher-order fluctuating terms, one obtains

$$\frac{\partial p'}{\partial t} + \frac{\partial}{\partial x_j}\left(p'\bar{u}_j + \bar{p}u_j' + \gamma\bar{p}u_j' + \gamma p'\bar{u}_j\right) - p'\frac{\partial \bar{u}_j}{\partial x_j} - \bar{p}\frac{\partial u_j'}{\partial x_j} - \gamma\bar{u}_j\frac{\partial p'}{\partial x_j} - \gamma u_j'\frac{\partial \bar{p}}{\partial x_j} = 0 \tag{3.28}$$

Reordering terms in equation (3.28) one obtains

$$\frac{\partial p'}{\partial t} + \frac{\partial}{\partial x_j}\left(p'\bar{u}_j + \gamma\bar{p}u_j'\right) + \bar{p}\cancel{\frac{\partial u_j'}{\partial x_j}} + u_j'\frac{\partial \bar{p}}{\partial x_j} + \gamma p'\frac{\partial \bar{u}_j}{\partial x_j} + \gamma\bar{u}_j\cancel{\frac{\partial p'}{\partial x_j}}$$
$$-p'\frac{\partial \bar{u}_j}{\partial x_j} - \bar{p}\cancel{\frac{\partial u_j'}{\partial x_j}} - \gamma\bar{u}_j\cancel{\frac{\partial p'}{\partial x_j}} - \gamma u_j'\frac{\partial \bar{p}}{\partial x_j} = 0, \tag{3.29}$$

where some terms cancel out. After slight reordering, the final form of energy equation reads

$$\frac{\partial p'}{\partial t} + \frac{\partial}{\partial x_j}\left(p'\bar{u}_j + \gamma\bar{p}u_j'\right) + (\gamma-1)\left(p'\frac{\partial \bar{u}_j}{\partial x_j} - u_j'\frac{\partial \bar{p}}{\partial x_j}\right) = 0. \tag{3.30}$$

3.2.4   Linearised Euler Equations

Equations (3.21), (3.27) and (3.30) represent the linearised Euler equations in conservative form which are used in this thesis. The equations are summarised below:

$$\frac{\partial \rho'}{\partial t} + \frac{\partial}{\partial x_j}\left(\bar{\rho}u_j' + \rho'\bar{u}_j\right) = 0, \tag{3.21}$$

$$\frac{\partial \bar{\rho}u_i'}{\partial t} + \frac{\partial}{\partial x_j}\left(\bar{\rho}\bar{u}_j u_i' + p'\delta_{ij}\right) + \left(\bar{\rho}u_j' + \rho'\bar{u}_j\right)\frac{\partial \bar{u}_i}{\partial x_j} = 0, \tag{3.27}$$

$$\frac{\partial p'}{\partial t} + \frac{\partial}{\partial x_j}\left(p'\bar{u}_j + \gamma\bar{p}u_j'\right) + (\gamma-1)\left(p'\frac{\partial \bar{u}_j}{\partial x_j} - u_j'\frac{\partial \bar{p}}{\partial x_j}\right) = 0. \tag{3.30}$$

Note that the underlined terms in equations (3.27) and (3.30) contain spatial derivatives of mean quantities which are equal to zero when the mean flow is uniform. The sound propagation in

---

a general non-uniform mean flow is governed by the system of equations (3.21), (3.27) and (3.30), which can be written in the following matrix form:

$$\frac{\partial \mathbf{U'}}{\partial t} + \frac{\partial \mathbf{E'}}{\partial x} + \frac{\partial \mathbf{F'}}{\partial y} + \frac{\partial \mathbf{G'}}{\partial z} + \mathbf{H'} = 0, \tag{3.31}$$

where

$$\mathbf{U'} = \begin{pmatrix} \rho' \\ \bar{\rho} u' \\ \bar{\rho} v' \\ \bar{\rho} w' \\ p' \end{pmatrix}, \mathbf{E'} = \begin{pmatrix} \bar{\rho} u' + \rho' \bar{u} \\ \bar{\rho} \bar{u} u' + p' \\ \bar{\rho} \bar{u} v' \\ \bar{\rho} \bar{u} w' \\ p' \bar{u} + \gamma \bar{p} u' \end{pmatrix}, \mathbf{F'} = \begin{pmatrix} \bar{\rho} v' + \rho' \bar{v} \\ \bar{\rho} \bar{v} u' \\ \bar{\rho} \bar{v} v' + p' \\ \bar{\rho} \bar{v} w' \\ p' \bar{v} + \gamma \bar{p} v' \end{pmatrix}, \mathbf{G'} = \begin{pmatrix} \bar{\rho} w' + \rho' \bar{w} \\ \bar{\rho} \bar{w} u' \\ \bar{\rho} \bar{w} v' \\ \bar{\rho} \bar{w} w' + p' \\ p' \bar{w} + \gamma \bar{p} w' \end{pmatrix}$$

and

$$\mathbf{H'} = \begin{pmatrix} 0 \\ (\bar{\rho} u' + \rho' \bar{u})\frac{\partial \bar{u}}{\partial x} + (\bar{\rho} v' + \rho' \bar{v})\frac{\partial \bar{u}}{\partial y} + (\bar{\rho} w' + \rho' \bar{w})\frac{\partial \bar{u}}{\partial z} \\ (\bar{\rho} u' + \rho' \bar{u})\frac{\partial \bar{v}}{\partial x} + (\bar{\rho} v' + \rho' \bar{v})\frac{\partial \bar{v}}{\partial y} + (\bar{\rho} w' + \rho' \bar{w})\frac{\partial \bar{v}}{\partial z} \\ (\bar{\rho} u' + \rho' \bar{u})\frac{\partial \bar{w}}{\partial x} + (\bar{\rho} v' + \rho' \bar{v})\frac{\partial \bar{w}}{\partial y} + (\bar{\rho} w' + \rho' \bar{w})\frac{\partial \bar{w}}{\partial z} \\ (\gamma - 1)\left[p'\left(\frac{\partial \bar{u}}{\partial x} + \frac{\partial \bar{v}}{\partial y} + \frac{\partial \bar{w}}{\partial z}\right) - \left(u'\frac{\bar{p}}{\partial x} + v'\frac{\bar{p}}{\partial y} + w'\frac{\bar{p}}{\partial z}\right)\right] \end{pmatrix}.$$

In Equation (3.31) the term **H'** substitutes underlined terms in equations (3.27) and (3.30) and denotes the effect of non-homogeneous mean flow. This term can be seen as a source term that is numerically treated explicitly. Other terms that contain unknown variables are time derivative $\frac{\partial \mathbf{U'}}{\partial t}$ and conservative form of spatial derivatives $\frac{\partial \mathbf{E'}}{\partial x} + \frac{\partial \mathbf{F'}}{\partial y} + \frac{\partial \mathbf{G'}}{\partial z}$.

Blom [6] presented the system of LEEs in "*formulation 2*" which contains the term **H'** with components that belong to momentum equation

$$\mathbf{H'}_{Blom,mom.eq.} = \bar{\rho} u'_j \frac{\partial \bar{u}_i}{\partial x_j} - \frac{\rho'}{\bar{\rho}} \frac{\partial \bar{p}}{\partial x_i}, \tag{3.32}$$

whereas the corresponding components of **H'** presented in this paper are

$$\mathbf{H'}_{mom.eq.} \left(\bar{\rho} u'_j + \rho' \bar{u}_j\right) \frac{\partial \bar{u}_i}{\partial x_j} \tag{3.33}$$

The difference is in the assumption of steady mean flow

$$\frac{\partial \bar{u}_i}{\partial t} = 0 \tag{3.34}$$

that is introduced in the set of LEEs presented in this MS thesis (can be seen in equation (3.26)). Considering the mean equation for conservation of momentum

$$\frac{\partial \bar{u}_i}{\partial t} + \bar{u}_j \frac{\partial \bar{u}_i}{\partial x_j} + \frac{1}{\bar{\rho}} \frac{\partial \bar{p}}{\partial x_i} = 0 \tag{3.35}$$

one recognises

$$\frac{\partial \bar{u}_i}{\partial t} = -\bar{u}_j \frac{\partial \bar{u}_i}{\partial x_j} - \frac{1}{\bar{\rho}} \frac{\partial \bar{p}}{\partial x_i} \tag{3.36}$$

If the assumption (3.34) was not introduced, the terms on the right-hand side of equation (3.36) would remain and, hence, the term **H'** would be in the form as in [6]:

$$\left(\bar{\rho} u'_j + \rho' \bar{u}_j \right) \frac{\partial \bar{u}_i}{\partial x_j} + \rho' \left(-\bar{u}_j \frac{\partial \bar{u}_i}{\partial x_j} - \frac{1}{\bar{\rho}} \frac{\partial \bar{p}}{\partial x_i} \right) = \bar{\rho} u'_j \frac{\partial \bar{u}_i}{\partial x_j} - \frac{\rho'}{\bar{\rho}} \frac{\partial \bar{p}}{\partial x_i} \tag{3.37}$$

where the first term denotes momentum components of the vector **H'** that belong to present set of LEEs, the second term denotes the unsteady non-uniform mean flow effects and the term on the right-hand side the corresponding components presented by Blom.

3.2.5　Linearised Euler Equations in Non-Conservative Form

Linearized Euler equations in non-conservative form written in primitive variables can be derived either through the set of non-conservative Euler equations (3.4), (3.6) and (3.13) or by applying the chain rule on the set (3.21), (3.27) and (3.30) and recognising the mean equation for conservation of mass in momentum equation. The linearised Euler equations written in primitive variables in non-conservative form read

$$\frac{\partial \rho'}{\partial t} + \bar{\rho} \frac{\partial u'_j}{\partial x_j} + \rho' \frac{\partial \bar{u}_j}{\partial x_j} + \bar{u}_j \frac{\partial \rho'}{\partial x_j} + u'_j \frac{\bar{\rho}}{\partial x_j} = 0, \tag{3.38}$$

$$\frac{\partial u'_i}{\partial t} + \bar{u}_j \frac{\partial u'_i}{\partial x_j} + u'_j \frac{\partial \bar{u}_i}{\partial x_j} + p' \frac{\bar{u}_j}{\gamma \bar{p}} \frac{\partial \bar{u}_i}{\partial x_j} + \frac{1}{\bar{\rho}} \frac{\partial p'}{\partial x_i} = 0, \tag{3.39}$$

$$\frac{\partial p'}{\partial t} + \bar{u}_j \frac{\partial p'}{\partial x_j} + u'_j \frac{\partial \bar{p}}{\partial x_j} + \gamma \bar{p} \frac{\partial u'_j}{\partial x_j} + \gamma p' \frac{\partial \bar{u}_j}{\partial x_j} = 0. \tag{3.40}$$

The equations (3.38), (3.39) and (3.40) are also obtained by Johnson et al.[7], with the exception that in their study the mass equation is substituted by the isentropic signal assumption

$$\rho' = \frac{p'}{c_0^2}, \tag{3.41}$$

where c_0 denotes the speed of sound.

The system of equations (3.39) and (3.40) is also implemented and tested in this thesis in order to verify the author's code. Preliminary results have shown that there is no difference between results obtained by using equations (3.39) and (3.40) and results obtained with equations (3.21), (3.27) and (3.30), so the latter set was used in further simulations because their terms are in conservative form, which is more suitable for finite volume discretisation.

3.2.6   Acoustic Equations for a Quiescent Fluid

Omitting all terms which are related to mean flow or to gradients of mean quantities in equations (3.38), (3.39) and (3.40), the linearized Euler equations for quiescent fluid are obtained:

$$\frac{\partial \rho'}{\partial t} + \bar{\rho}\frac{\partial u'_j}{\partial x_j} = 0, \tag{3.42}$$

$$\bar{\rho}\frac{\partial u'_i}{\partial t} + \frac{\partial p'}{\partial x_i} = 0, \tag{3.43}$$

$$\frac{\partial p'}{\partial t} + \gamma\bar{p}\frac{\partial u'_j}{\partial x_j} = 0. \tag{3.44}$$

Using only momentum and energy equations (3.43) and (3.44) the *wave equation* can be obtained. This is done by differentiating the Equation (3.43) in space and the Equation (3.44) in time. Subtracting the former from the latter, the wave equation written in terms of pressure fluctuation is obtained

$$\frac{\partial^2 p'}{\partial t^2} - \frac{\gamma\bar{p}}{\bar{\rho}}\frac{\partial^2 p'}{\partial x_j^2} = 0, \tag{3.45}$$

or

$$\frac{\partial^2 p'}{\partial t^2} - c_0^2\frac{\partial^2 p'}{\partial x_j^2} = 0, \tag{3.46}$$

where the equation for speed of sound in an ideal gas is used

$$c_o = \sqrt{\frac{\gamma\bar{p}}{\bar{\rho}}} \tag{3.47}$$

Using the isentropic signal assumption (3.41), the wave equation can be written in terms of density fluctuation

$$\frac{\partial^2 \rho'}{\partial t^2} - c_0^2\frac{\partial^2 \rho'}{\partial x_j^2} = 0 \tag{3.48}$$

3.3   Boundary Conditions in Computational Aeroacoustics

In most cases it is prohibitively expensive to compute the turbulence and its acoustic radiation at the same time. The compromise is to conduct the calculations separately. First, the flow field is calculated via LES or unsteady RANS, then the acoustic field is obtained through CAA calculation. The latter calculation is carried out using turbulence data from obtained CFD simulation as input. In the following text the far-field non-reflecting boundary conditions will be explained. Also, the linearised Euler equations, formed in matrix form, will be used

$$\frac{\partial \mathbf{u}}{\partial t} + \mathbf{A}\frac{\partial \mathbf{u}}{\partial x} + \mathbf{B}\frac{\partial \mathbf{u}}{\partial y} + \mathbf{C}\frac{\partial \mathbf{u}}{\partial z} + \mathbf{D}\mathbf{u} = 0, \tag{3.49}$$

where

$$\mathbf{u} = \begin{pmatrix} \rho' \\ u' \\ v' \\ w' \\ p' \end{pmatrix}, \mathbf{A} = \begin{pmatrix} \bar{u} & \bar{\rho} & 0 & 0 & 0 \\ 0 & \bar{u} & 0 & 0 & \frac{1}{\bar{\rho}} \\ 0 & 0 & \bar{u} & 0 & 0 \\ 0 & 0 & 0 & \bar{u} & 0 \\ 0 & \gamma\bar{p} & 0 & 0 & \bar{U} \end{pmatrix}, \mathbf{B} = \begin{pmatrix} 0 & 0 & \bar{\rho} & 0 & 0 \\ 0 & 0 & 0 & 0 & 0 \\ 0 & 0 & 0 & 0 & \frac{1}{\bar{\rho}} \\ 0 & 0 & 0 & 0 & 0 \\ 0 & 0 & \gamma\bar{p} & 0 & 0 \end{pmatrix},$$

$$\mathbf{C} = \begin{pmatrix} 0 & 0 & 0 & \bar{\rho} & 0 \\ 0 & 0 & 0 & 0 & 0 \\ 0 & 0 & 0 & 0 & 0 \\ 0 & 0 & 0 & 0 & \frac{1}{\bar{\rho}} \\ 0 & 0 & 0 & \gamma\bar{p} & 0 \end{pmatrix}, \mathbf{D} = \begin{pmatrix} 0 & 0 & \frac{d\bar{\rho}}{dy} & 0 & 0 \\ 0 & 0 & \frac{d\bar{u}}{dy} & 0 & 0 \\ 0 & 0 & 0 & 0 & 0 \\ 0 & 0 & 0 & 0 & 0 \\ 0 & 0 & 0 & 0 & 0 \end{pmatrix}$$

where $\bar{u}$, $\bar{\rho}$ and $\bar{p}$ are the mean velocity, density and pressure. γ is the ratio of specific heats. It is assumed that the flow varies only in y direction. Equation (3.49) can be obtained from the Equation (3.31) by extraction of the Jacobian matrices $\mathbf{A}$, $\mathbf{B}$, $\mathbf{C}$ and $\mathbf{D}$, which will be used in the following subsection.

3.3.1   Characteristic Non-reflecting Boundary Condition

In the case of nearly normal incident angle of the acoustic wave, the characteristic non-reflecting boundary condition gives satisfactory results. This kind of boundary condition is based on the characteristic splitting of the Jacobian matrices $\mathbf{A}$, $\mathbf{B}$ or $\mathbf{C}$ in Equation (3.49) at the boundary where the x, y or z coordinate is constant.

If we take, for example, the case of non-reflecting boundary where $x = x_0$ the decomposition of **A** would be

$$\mathbf{A} = \mathbf{E}\Lambda\mathbf{E}^{-1} \tag{3.50}$$

where Λ is the eigenvalue diagonal matrix and **E** is the eigenvector matrix. In the next step only positive eigenvalues remain so the matrix Λ changes to Λ^+ and matrix **A** changes to $\mathbf{A}^+$. Taking into account above changes the Equation (3.50) takes the form

$$\frac{\partial \mathbf{u}}{\partial t} + \mathbf{A}^+\frac{\partial \mathbf{u}}{\partial x} + \mathbf{B}\frac{\partial \mathbf{u}}{\partial y} + \mathbf{C}\frac{\partial \mathbf{u}}{\partial z} + \mathbf{D}\mathbf{u} = 0 \tag{3.51}$$

In this form (after generalising the characteristic splitting to other coordinates) the backward differencing can be applied to all spatial derivatives.

The issue with characteristic splitting is that matrices *A*, *B* and *C* are not simultaneously diagonalisable so the characteristic non-reflecting boundary condition is not exact. This results in existence of the reflection coefficient

$$R_{acoustic} = \frac{1 - \cos\Phi_i}{1 - \cos\Phi_r} \tag{3.52}$$

where Φ_i and Φ_r denote outgoing and reflected wave, respectively. Now it is shown in Equation (3.52) that this kind of boundary condition works best in the cases of nearly normal incident angles of outgoing waves to the boundary.

3.3.2 Radiation Boundary Condition

The radiation boundary condition simulates the infinite domain with a bounded one and is based on representing the solution in asymptotic forms at the far field. This is done by asymptotic expansion that is written in form of ascending powers of $\frac{1}{r}$, where *r* is the distance between the boundary point and the source of the sound. When asymptotic expansion is known, the radiation boundary condition is derived in the form of differential equations. The radiation boundary condition can be easily discretised by using backward differences, that is without any information outside computational domain. Balyiss and Turkel [8] give several radiation boundary conditions with the following approximation for pressure

$$\frac{\partial p}{\partial t} + \frac{\partial p}{\partial r} + \frac{p}{r} = 0. \tag{3.53}$$

Due to the fact that the radiation boundary condition is based on the asymptotic expansion of the solution, the non-reflecting boundaries should be placed far away from the sound source.

3.3.3   Absorbing-zone Techiques

In the literature, beside the name "absorbing zone", names such as "buffer layers" or "sponge layer" can be found. Such tecniques use additonal zones of the grid which surround the physical domain, whose function is to attenuate outgoing waves and hence minimize the reflection of waves. There are various kinds of absorbing zone boundaries, and some will be explained in the following text.

3.3.3.1   Artificial Dissipation and Damping

This kind of absorbing zone uses the similar governing equations as in physical domain, with only difference being the additional damping term. Either with Navier-Stokes or Euler equations, the modified equation reads:

$$\frac{\partial \mathbf{u}}{\partial t} = L(\mathbf{u}) - \nu(\mathbf{u} - \mathbf{u}_0), \tag{3.54}$$

where $\mathbf{u}$ is the solution vector, L represents all spatial operators of the Equation (3.54), ν is the positive damping coefficient and u_0 is the mean value of u in absorbing zone which is time independent.

3.3.3.2   Grid Stretching and Numerical Filtering

Beside modification of equations in the absorbing zone, the attenuation can be achieved via numerical damping. This can be done by gradually stretching and coarsening the grid in the downstream direction in the absorbing layer. In this way the wave is underresolved and numerically dissipated. The grid stretching has to be done smoothly, otherwise it will cause numerical reflection [9]. This method often includes low-pass numerical filters in order to reduce the length of the absorbing zone. In some cases high-order filters should be applied even to the physical domain [10].

3.3.3.3   Modification of Convective Mean Velocity

Another way to avoid reflections is to modify the mean flow inside the buffer zone so that it becomes supersonic. The formulation consists of additional artificial convective terms of the

form:

$$U_0(x,y)\frac{\partial \mathbf{u}}{\partial x} + V_0(x,y)\frac{\partial \mathbf{u}}{\partial y}, \tag{3.55}$$

where U_0 and V_0 are the artificial velocities and are equal to zero at the beginning of the buffer zone and gradually increase towards the end of the zone.

3.3.4 Perfectly Matched Layers (PML)

The first PML formulation was given by Berenger [11] for boundary treatment of Maxwell equation in computational electromagnetics. Hu [12] has implemented PML in linearized Euler equations and obtained numerically stable results. The idea behind the PML is the same as in absorbing zone techiques. The difference is that in PML the equations match perfectly to the governing equations of the physical domain. Fulfilling the conditions of PML, the boundary of physical domain should not give any reflections, whatever the frequency or the angle of the outgoing wave. Moreover, the PML zones are much shorter than buffer zones and are less sensitive to parametric variations.

3.4 Sound Sources

The acoustic field calculation can be conducted using direct or hybrid approach. In direct simulation both the flow and aerodynamically generated acoustic fields are solved fully using compressible Navier-Stokes equations. In hybrid approach the computation domain is split into different regions, so that the acoustic and the flow field can be solved with different equations and different numerical techniques. The flow field can be calculated either via steady state (e.g. RANS) or transient solver (e.g. DNS, LES, URANS, DES). Using information obtained from the flow simulation, one can calculate *acoustic sources*, which are further provided to the CAA solver that calculates the propagation of sound, using integral methods (Lighthill's analogy, FW-H analogy, Kirchhoff integral) or computational methods (LEE, APE, PCE...).

In the following section, a method proposed by Kraichnan [13], Bailly et al. [14] and later Billson [15] for sound generation and propagation will be described.

3.4.1 The SNGR Method

The Stochastic Noise Generation and Radiation (SNGR) method can be split into three steps:

1. Calculation of compressible RANS solution using $k - \varepsilon$ turbulence model.

2. Calculation of unsteady turbulent velocity field using turbulent kinetic energy, time scale and length scale from RANS solution. Random Fourier modes are used to calculate the turbulent velocity field.

3. Calculation of non-homogeneous linearized Euler equations [15] with source terms obtained from turbulence field that is provided in step 2. The mean flow field from RANS solution is also taken into account in the LEEs.

First and second step will be more closely described in following subsections.

3.4.1.1 Reynolds Averaged Navier-Stokes Solution

There are actually two purposes of the RANS solution. The first is to provide the mean flow quantities for the linearized Euler equations in step 3. The other purpose is to provide the turbulence quantities k and ε (turbulence kinetic energy and dissipation rate) used as input data for calculation of turbulent velocity field in step 2.

3.4.1.2 Generation of Synthesized Turbulence

A time and space dependent turbulent velocity field is generated using random Fourier modes [15]. Kraichnan [13] and Bailly et al. [14] proposed an equation for space and time dependent turbulence velocity field

$$\mathbf{u}_t(\mathbf{x},t) = 2 \sum_{n=1}^{N} \hat{u}_n \cos(\mathbf{k}_n(\mathbf{x} - \mathbf{u}_c t) + \psi_n + \omega_n t) \sigma_n, \tag{3.56}$$

Billson [15] proposed similar equation that is only space dependent:

$$\mathbf{u}_t(\mathbf{x}) = 2 \sum_{n=1}^{N} \hat{u}_n \cos(\mathbf{k}_n \mathbf{x} + \psi_n) \sigma_n, \tag{3.57}$$

where $\hat{u}_n$, $\mathbf{k}_n$, ψ_n and σ_n are amplitude, wave number vector, phase and direction of the nth Fourier mode, respectively. The length of direction σ_n is $|\sigma_n| = 1$. The orientation of $\mathbf{k}_n$ is

random on a sphere with radius k_n in order to ensure the isotropy of the turbulent velocity field. The time dependency of the synthesized turbulence velocity field is introduced through convective operator and time filter in order to avoid a problem of spatial de-correlation [15].

If one assumes the incompressibility, the continuity equation gives the relation

$$\mathbf{k}_n \cdot \boldsymbol{\sigma}_n \equiv 0 \tag{3.58}$$

for all n, i.e. the wave number vector and the spatial direction of nth Fourier mode are perpendicular. The spatial angles φ_n, α_n, θ_n and the phase ψ_n are random with following probability functions

$$
\begin{aligned}
p(\varphi_n) &= 1/(2\pi), \quad 0 \leqslant \varphi_n \leqslant 2\pi, \\
p(\psi_n) &= 1/(2\pi), \quad 0 \leqslant \psi_n \leqslant 2\pi, \\
p(\theta_n) &= (1/2)\sin\theta, \quad 0 \leqslant \theta_n \leqslant \pi, \\
p(\alpha_n) &= 1/(2\pi), \quad 0 \leqslant \alpha_n \leqslant 2\pi.
\end{aligned}
\tag{3.59}
$$

One can conclude from (3.59) that the distribution of the direction of $\mathbf{k}_n$ is uniform on the surface of the sphere.

The amplitude of each mode $\hat{u}_n$ can be calculated by

$$\hat{u}_n = \sqrt{E(k_n)\Delta k_n}, \tag{3.60}$$

where $E(k_n)$ is the turbulence energy spectrum function and Δk_n is a small interval in the spectrum located at k_n. The energy spectrum of isotropic turbulence is simulated by model spectrum, see Figure 3.4.1 Turbulence kinetic energy is then calculated by the sum of squares of $\bar{u}_n$ over all n

$$\bar{k} = \sum_{n=1}^{N} \hat{u}_n^2. \tag{3.61}$$

Billson [15] used modified von Kármán-Pao sprectrum in order to simulate the energy spectrum for isotropic turbulence

$$E(k) = \alpha \frac{u'^2}{k_e} \frac{(k/k_e)^4}{[1+(k/k_e)^2]^{17/6}} e^{[-2(k/k_\eta)^2]}, \tag{3.62}$$

where k is the wave number, $k_\eta = \varepsilon^{1/4}\nu^{-3/4}$ is the Kolmogorov wave number, ν is the molecular viscosity, ε is the turbulent dissipation rate, $u'^2 = 2\bar{k}/3$ is the root mean square value of the velocity fluctuations. One can notice that there are two free parameters in equation (3.62):
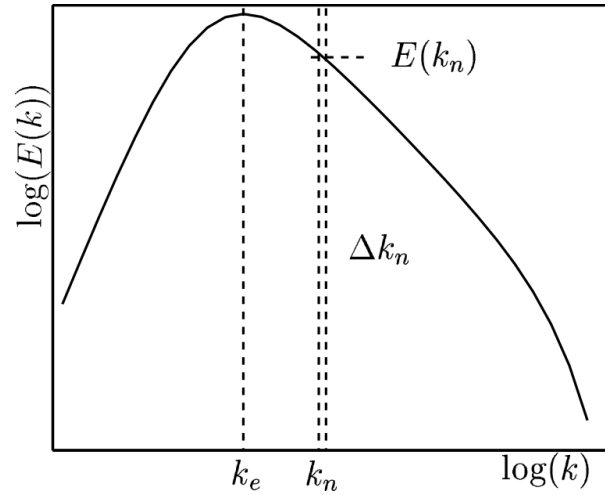
Figure 3.4.1: Model spectrum [15].

α and k_e. α determines the kinetic energy of the spectrum and k_e is the wave number of the eddies that contain the most of the kinetic energy in the spectrum. The information available in RANS solution are turbulent kinetic energy $\bar{k}$ and turbulent dissipation rate ε. These quantities are used to determine α and k_e and, thus, shape of the spectrum shown in Figure 3.4.1. The constant α can be determined by requiring that the total turbulent kinetic energy must be equal to the integral of the energy spectrum over all wave numbers

$$\bar{k} = \int_0^\infty E(k)dk \tag{3.63}$$

In [15] the α was found to be $\alpha = 1.45276$.

The turbulence length scale from the RANS solution can be obtained as

$$L_t = f_L \frac{\bar{k}^{3/2}}{\varepsilon}, \tag{3.64}$$

where f_L is the length scale factor.

Assuming that the length scale from the RANS solution is the same as the integral length scale for isotropic turbulence, one gets the equation

$$L_t = \frac{\pi}{2u'^2} \int_0^\infty \frac{E(k)}{k} dk \tag{3.65}$$

which is used to determine the wave number k_e. This can be done by

$$k_e = \frac{9\pi}{55} \frac{\alpha}{L_t} \tag{3.66}$$

where L_t in known from RANS solution and $\alpha = 1.45276$.

The time dependence of synthesized turbulence velocity field can be found in [15].

Chapter 4

Verification and Validation

This chapter is organised as follows: Section 4.1 presents the methodology for solving the LEEs numerically. Section 4.2 section deals with three benchmark cases, which have been used to validate the solver for the acoustic propagation. Section 4.3 gives the equations for estimating the grid convergence error.

4.1 Numerical Methodology

Equations (3.21), (3.27) and (3.30), used in this thesis, are partial differential equations (PDEs). In general, the exact solution to PDEs is limited to only few simplest problems and most often does not exist for the problems in the engineering practice.

A numerical method suitable for solving the system of PDEs is the Finite Volume Method (FVM), which is used in this thesis. OpenFOAM-extend software package has been used to solve the equations (3.21) - (3.30) numerically.

The FVM is a discretisation method that requires division of the computational domain into a finite number of volumes, which are called finite volumes. In order to find numerical solutions to PDEs using the finite volume method, terms in PDEs have to be expressed through volume integrals of finite volumes, which are then converted to surface integrals using the Gauss's theorem. The approximation is then introduced through representing the surface integrals as sums of the fluxes at the surfaces of each finite volume. For more details see [16], [17].

4.2   Benchmark Cases

The validation of the developed solver with linearized Euler equations has been made with three benchmark cases for which the analytical solution is provided in ICASE/LaRC Workshop on Benchmark Problems in Computational Aeroacoustics (CAA), [2]. In this workshop, the benchmark problems are defined as problems 1 and 2 in Category 3 and problem 1 in Category 4. For convenience, in the following text these benchmark problems will be called test case with horizontal mean flow, test case with diagonal mean flow and reflective wall test case, respectively.

4.2.1   Test Cases with Horizontal and Diagonal Mean Flows

In [2], test cases with horizontal and diagonal mean flows are presented to test the effectiveness of radiation boundary conditions, inflow and outflow boundary conditions and the isotropy property of the computational algorithm. The variables are dimensionless with the following scales

- Δx = length scale*,

- a_∞ (ambient sound speed) = velocity scale,

- $\frac{\Delta x}{a_\infty}$ = time scale,

- ρ_∞ = density scale and

- $\rho_\infty a_\infty^2$ = pressure scale.

*The length scale is obtained by using the cell size of the coarsest grid (40K).

The computational domain is defined with $-100 \leqslant x \leqslant 100$, $-100 \leqslant y \leqslant 100$ and is embedded in free space (see Figure 4.2.3).

4.2.1.1   Test Case with Horizontal Mean Flow

For given $M_x = 0.5$ and $M_y = 0$ the initial value problem is to be solved. Initial fields of dimensionless variables, fluctuations of pressure $\hat{p}'$, density $\hat{\rho}'$ and velocity components $\hat{u}'$ and

$\hat{v'}$, are given for dimensionless time $\hat{t} = 0$ with:

$$\hat{p'} = \exp\left[-(\ln 2)\left(\frac{x^2+y^2}{9}\right)\right], \tag{4.1}$$

$$\hat{\rho'} = \exp\left[-(\ln 2)\left(\frac{x^2+y^2}{9}\right)\right] + 0.1\exp\left[-(\ln 2)\left(\frac{(x-67)^2+y^2}{25}\right)\right], \tag{4.2}$$

$$\hat{u'} = 0.04\,y\exp\left[-(\ln 2)\left(\frac{(x-67)^2+y^2}{25}\right)\right], \tag{4.3}$$

$$\hat{v'} = -0.04\,(x-67)\exp\left[-(\ln 2)\left(\frac{(x-67)^2+y^2}{25}\right)\right]. \tag{4.4}$$

4.2.1.2 Analytical Solution to Test Case with Horizontal Mean Flow

Let $\alpha_1 = \frac{\ln 2}{9}$, $\alpha_2 = \frac{\ln 2}{25}$, $M = 0.5$ and $\eta = \left[(x-Mt)^2+y^2\right]^{1/2}$. The analytical solution is given by Tam and Webb in [18]:
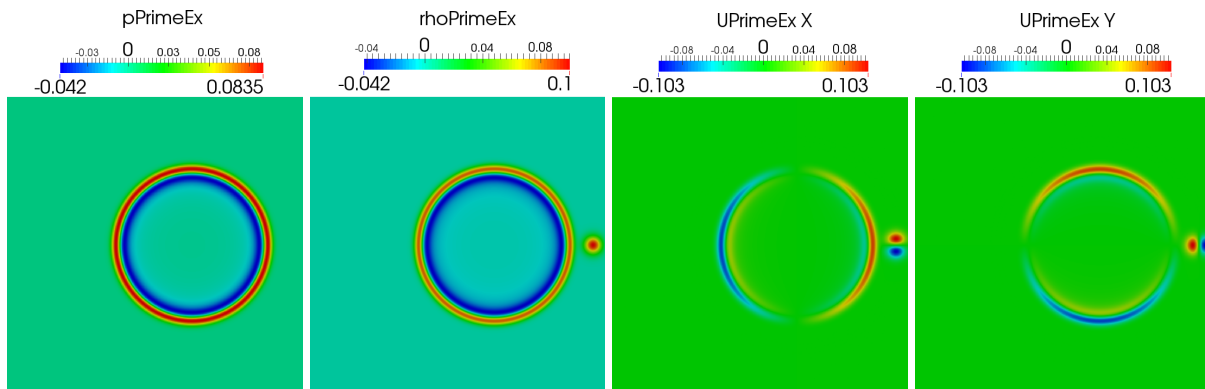
$$\hat{u'} = \frac{x-Mt}{2\alpha_1\eta}\int_0^\infty e^{\frac{-\xi^2}{4\alpha_1}}\sin(\xi t)J_1(\xi\eta)\xi d\xi + 0.04ye^{-\alpha_2\left[(x-67-Mt)^2+y^2\right]}, \tag{4.5}$$

$$\hat{v'} = \frac{y}{2\alpha_1\eta}\int_0^\infty e^{\frac{-\xi^2}{4\alpha_1}}\sin(\xi t)J_1(\xi\eta)\xi d\xi - 0.04(x-67-Mt)e^{-\alpha_2\left[(x-67-Mt)^2+y^2\right]}, \tag{4.6}$$

$$\hat{p'} = \frac{1}{2\alpha_1}\int_0^\infty e^{\frac{-\xi^2}{4\alpha_1}}\cos(\xi t)J_0(\xi\eta)\eta d\eta, \tag{4.7}$$

$$\hat{\rho'} = \hat{p'} + 0.1e^{-\alpha_2\left[(x-67-Mt)^2+y^2\right]}, \tag{4.8}$$

where $J_0(...)$ and $J_1(...)$ are Bessel functions of order 0 and 1.

Figure 4.2.1: Analytical solutions for test case with horizontal mean flow at time $\hat{t} = 50$: Acoustic fields $\hat{p'}$, $\hat{\rho'}$, $\hat{u'}$ and $\hat{v'}$.

4.2.1.3   Test Case with Diagonal Mean Flow

For given $M_x = M_y = 0.5\cos\left(\frac{\pi}{4}\right)$ the initial value problem is to be solved. Initial fields of dimensionless variables $\hat{p}'$, $\hat{\rho}'$, $\hat{u}'$ and $\hat{v}'$ are given for time $\hat{t} = 0$ with:

$$\hat{p}' = \exp\left[-(\ln 2)\left(\frac{x^2 + y^2}{9}\right)\right], \tag{4.9}$$

$$\hat{\rho}' = \exp\left[-(\ln 2)\left(\frac{x^2 + y^2}{9}\right)\right] + 0.1\exp\left[-(\ln 2)\left(\frac{(x-67)^2 + (y-67)^2}{25}\right)\right], \tag{4.10}$$

$$\hat{u}' = 0.04(y-67)\exp\left[-(\ln 2)\left(\frac{(x-67)^2 + (y-67)^2}{25}\right)\right], \tag{4.11}$$

$$\hat{v}' = -0.04(x-67)\exp\left[-(\ln 2)\left(\frac{(x-67)^2 + (y-67)^2}{25}\right)\right]. \tag{4.12}$$

Note that the mean flow is in the direction of the diagonal of the computational domain.

4.2.1.4   Analytical Solution to Test Case with Diagonal Mean Flow

Let $\alpha_1 = \frac{\ln 2}{9}$, $\alpha_2 = \frac{\ln 2}{25}$, $M_x = M_y = 0.5\cos\left(\frac{\pi}{4}\right)$ and $\eta = \left[(x - M_x t)^2 + (y - M_y t)^2\right]^{1/2}$. The analytical solution is given by

$$\hat{u}' = \frac{x - M_x t}{2\alpha_1 \eta}\int_0^\infty e^{\frac{-\xi^2}{4\alpha_1}}\sin(\xi t)J_1(\xi\eta)\xi d\xi + 0.04(y - M_y t)e^{-\alpha_2\left[(x-67-M_x t)^2 + (y-67-M_y t)^2\right]}, \tag{4.13}$$

$$\hat{v}' = \frac{y - m_y t}{2\alpha_1 \eta}\int_0^\infty e^{\frac{-\xi^2}{4\alpha_1}}\sin(\xi t)J_1(\xi\eta)\xi d\xi - 0.04(x - 67 - M_x t)e^{-\alpha_2\left[(x-67-M_x t)^2 + (y-67-M_y t)^2\right]}, \tag{4.14}$$

$$\hat{p}' = \frac{1}{2\alpha_1}\int_0^\infty e^{\frac{-\xi^2}{4\alpha_1}}\cos(\xi t)J_0(\xi\eta)\eta d\eta, \tag{4.15}$$

$$\hat{\rho}' = \hat{p}' + 0.1e^{-\alpha_2\left[(x-67-M_x t)^2 + (y-67-M_y t)^2\right]}, \tag{4.16}$$

where $J_0(...)$ and $J_1(...)$ are Bessel functions of order 0 and 1.

The idea behind the sets of equations (4.1) to (4.4) and (4.9) to (4.12) is to introduce three initial pulses: acoustic, entropy and vorticity pulse [18]. Acoustic pulse consists of pressure and density fluctuations (eq. (4.1) and the first term of eq. (4.2)), entropy pulse of density fluctuation (second term in eq. (4.2)) while the vorticity pulse consists of velocity fluctuations (equations (4.3) and (4.4)).

The acoustic wave involves all fluctuation variables ($\hat{p}'$, $\hat{\rho}'$, $\hat{u}'$ and $\hat{v}'$), despite the fact that it is initialised only with pressure and density fluctuations. It is non-dispersive, non-dissipative,
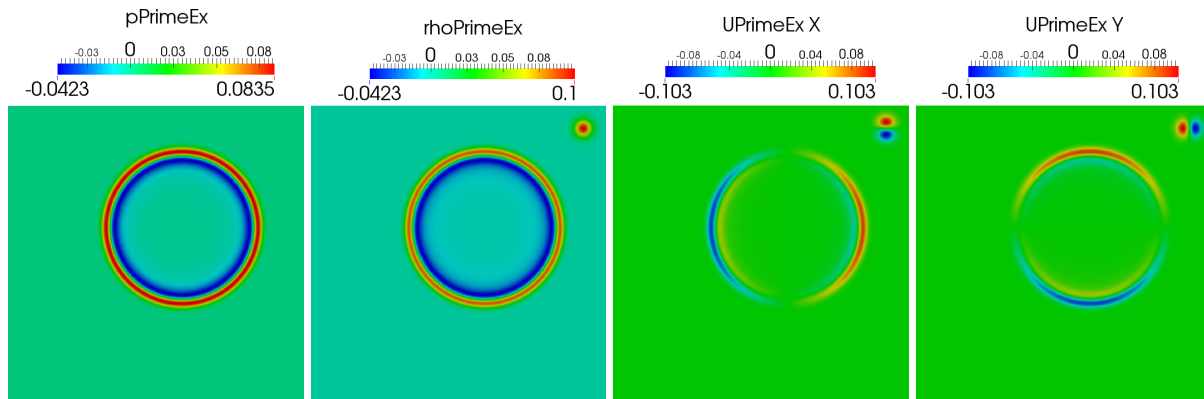
Figure 4.2.2: Analytical solutions for test case with diagonal mean flow at time $\hat{t} = 50$: Acoustic fields $\hat{p}'$, $\hat{\rho}'$, $\hat{u}'$ and $\hat{v}'$.

isotropic and propagates with the speed of sound [18]. The entropy waves involve only density fluctuations, whereas the vorticity waves consist only of velocity fluctuations. Both kind of waves are non-dissipative, non-dispersive and highly directional. They are convected in the direction of the mean flow and have the same mean velocity as the flow [18]. Taking these characteristics into consideration, numerical calculation of propagation of the acoustic, entropy and vorticity waves provides a possibility of examining how much numerical dispersion, dissipation or radiation anisotropy does the numerical procedure introduce.

All initial pulses are generated using Gaussian distribution. It could be noticed from equations (4.9)-(4.12) that the vorticity and entropy pulses are initiated at two thirds of the distance from the center of the domain (where the acoustic pulse is initiated) to the outflow boundary.

Figure 4.2.3 shows initial fields of $\hat{\rho}'$ for test cases with horizontal and diagonal mean flow, where only the acoustic and entropy pulses are visible. One can note that the acoustic pulse is initiated with the maximum value $\hat{p}'_{max} = \hat{\rho}'_{max} = 1$, whereas the entropy pulse is initiated with $\hat{\rho}'_{max} = 0.1$ (blue dots in the right parts of domains in Figure 4.2.3). Vorticity pulse cannot be seen on Figure 4.2.3, because it does not consist of density fluctuation.

4.2.2   Test Case with Reflective Wall

Test case with reflective wall is designed to test the effectiveness of wall boundary conditions, where the same dimensionless variables are used in previous test cases. The test case gives a reflection of an acoustic pulse off a wall in the presence of a uniform flow in semi-infinite
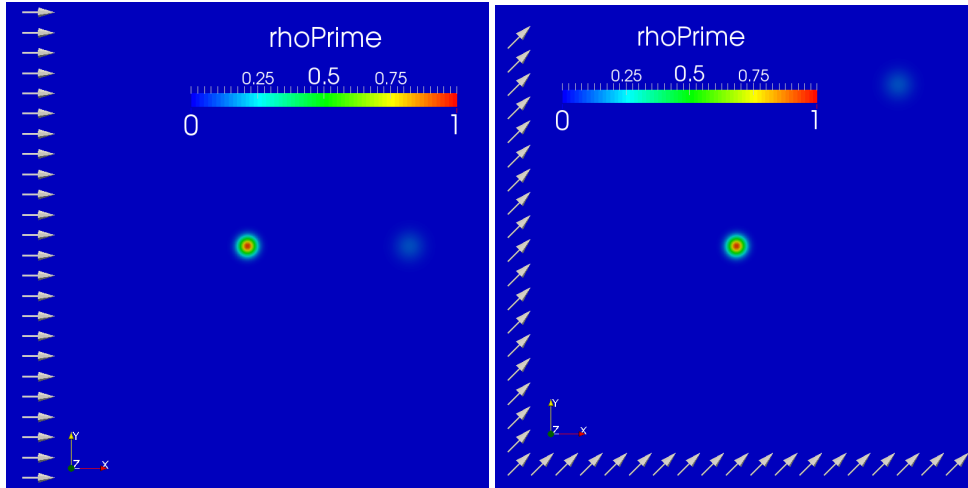
Figure 4.2.3: Initial field of $\hat{\rho}'$ for test cases with horizontal mean flow (left) and diagonal mean flow (right); arrows show the direction of the mean velocity field $\bar{u}$.

space.

The computational domain is defined with $-100 \leqslant x \leqslant 100$, $0 \leqslant y \leq 200$. The wall is located at $y = 0$ (see Figure 4.2.4). The initial condition for $\hat{t} = 0$ is given by

$$\hat{u}' = \hat{v}' = 0, \tag{4.17}$$

$$\hat{p}' = \hat{\rho}' = \exp\left\{ -(\ln 2)\left[\frac{x^2 + (y-25)^2}{25} \right] \right\}. \tag{4.18}$$

Note that the denominator, 25, in the argument of exponential function in eq. (4.18) is different compared to denominators, 9, in arguments of exponential functions for acoustic pulses (i.e. first terms) in equations (4.1), (4.2), (4.9) and (4.10). These denominators represent the squares of half-widths [18] of the corresponding pulses, so the half-widths take values 3, for acoustic pulses in test cases with horizontal and diagonal mean flow, and 5, for vorticity and entropy pulses in the same test cases, and for the acoustic pulse in the test case with reflective wall. Greater half-width of a pulse results in wider distribution of the pulse, i.e. smaller gradients of the reference variable. Figure 4.2.4 shows the initial field of $\hat{p}'$ for the test case with reflective wall.
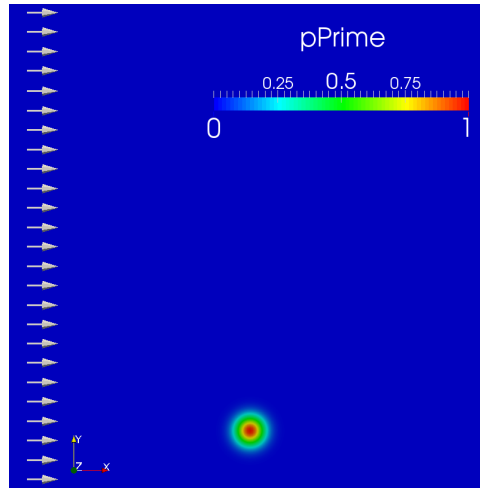
Figure 4.2.4: Initial field of dimensionless $\hat{p}'$ for reflective wall test case. Arrows show the direction of the mean velocity field $\bar{u}$. The bottom boundary represents the wall.

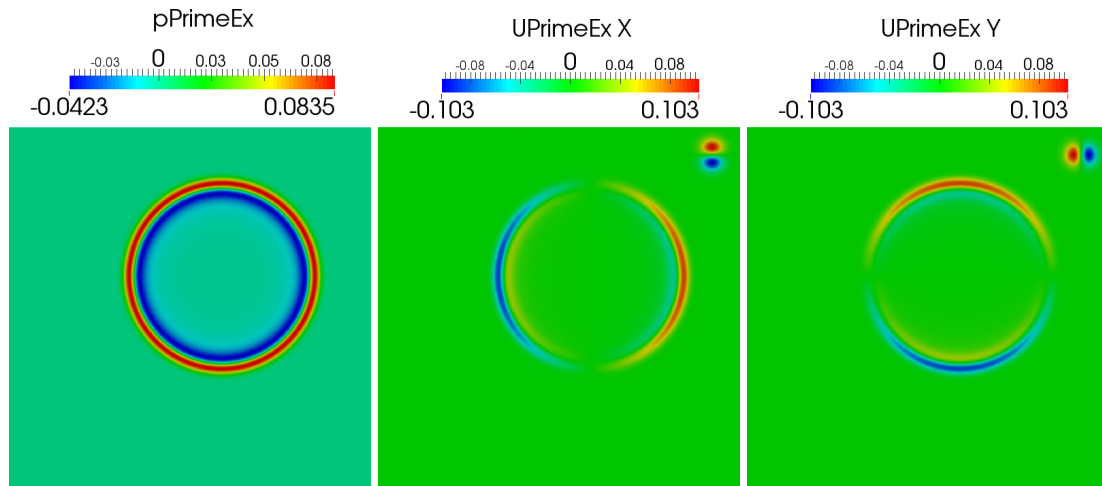#### 4.2.2.1 Analytical Solution for Test Case with Reflective Wall

With $\alpha = \frac{\ln 2}{25}$, $\eta = \left[(x - Mt)^2 + (y - 25)^2\right]^{1/2}$ and $\zeta = \left[(x - Mt)^2 + (y + 25)^2\right]^{1/2}$ the analytical solution has the following form [2]:

$$\hat{u}' = \frac{x - Mt}{2\alpha\eta} \int_0^\infty e^{-\frac{\xi^2}{4\alpha}} \sin(\xi t) J_1(\xi\eta)\xi d\xi + \frac{x - Mt}{2\alpha\zeta} \int_0^\infty e^{-\frac{\xi^2}{4\alpha}} \sin(\xi t) J_1(\xi\zeta)\xi d\xi, \quad (4.19)$$

$$\hat{v}' = \frac{y - 25}{2\alpha\eta} \int_0^\infty e^{-\frac{\xi^2}{4\alpha}} \sin(\xi t) J_1(\xi\eta)\xi d\xi + \frac{y + 25}{2\alpha\zeta} \int_0^\infty e^{-\frac{\xi^2}{4\alpha}} \sin(\xi t) J_1(\xi\zeta)\xi d\xi, \quad (4.20)$$

$$\hat{p}' = \hat{\rho}' = \frac{1}{2\alpha} \int_0^\infty e^{-\frac{\xi^2}{4\alpha}} \cos(\xi t) \left[J_0(\xi\eta) + J_0(\xi\zeta) \right] \xi d\xi. \quad (4.21)$$

The author has noticed that in the eq. (4.20) the sign in the factor $\frac{y+25}{2\alpha\zeta}$ has been wrongly written in [2], page 11, Problem 1, second equation.

Figure 4.2.5: Analytical solutions for the test case with reflective wall at time $\hat{t} = 50$: Acoustic fields $\hat{p}'$, $\hat{u}'$ and $\hat{v}'$.

4.3   Grid Convergence Error Analysis

Verification of the numerical procedure will be carried out through Richardson extrapolations, in standard and generalized form, as well as through orders of accuracy for computational procedure. Grid Convergence Index (GCI) will also be assessed [19].

Richardson [20], [21] as cited in [22] introduced a method for extrapolating two discrete second-order solutions to yield a fourth-order accurate solution. The two solutions were obtained on a fine grid with spacing h_1 and a coarse grid with spacing h_2, where $h_2/h_1 = 2$. For a second-order numerical scheme, the two discrete solutions f_1 and f_2 may be written as

$$f_1 = f_{exact} + g_2 h_1^2 + \mathcal{O}(h_1^3), \tag{4.22}$$

$$f_2 = f_{exact} + g_2 h_2^2 + \mathcal{O}(h_2^3), \tag{4.23}$$

where f_{exact} and g_2 are the exact solution and the coefficient of the second-order error term, respectively. For a second-order scheme, the coefficient g_1 is zero, so the terms $g_1 h_1$ and $g_1 h_2$ vanish from equations (4.22) and (4.23).

Neglecting terms of the order h^3 and higher, one obtains approximations of the coefficient

g_2 and f_{exact}: $\tilde{g}_2$ and $\tilde{f}_{exact}$. The system can now be solved and yields

$$\tilde{g}_2 = \frac{f_2 - f_1}{3h_1^2}, \tag{4.24}$$

$$\tilde{f}_{exact} = f_1 + \frac{f_1 - f_2}{3}, \tag{4.25}$$

where $\tilde{f}_{exact}$ is also called the (standard) Richardson extrapolate.

The requirement for ratio $h_2/h_1 = 2$ can often be difficult to fulfill, which is especially the case for 3D grids (i.e. the number of cells would have to be increased or reduced 8 times). Hence, Roache [19] introduced the generalized procedure for Richardson extrapolation with arbitrary grid refinement factor r and order p. The analogous equations to eq. 4.22 and eq. 4.23 can now be rewritten as

$$f_1 = f_{exact} + g_p h_1^p + \mathcal{O}(h_1^{p+1}), \tag{4.26}$$

$$f_2 = f_{exact} + g_p h_2^p + \mathcal{O}(h_2^{p+1}) \tag{4.27}$$

and the approximate coefficient $\tilde{g}_p$ and $\tilde{f}_{exact}$ read

$$\tilde{g}_p = \frac{f_2 - f_1}{h_1^p(r^p - 1)}, \tag{4.28}$$

$$\tilde{f}_{exact} = f_1 + \frac{f_1 - f_2}{r^p - 1}, \tag{4.29}$$

where $r = r_{21} = h_2/h_1$ and p denotes the order of accuracy. The generalized form of r yields $r_{k+1,k} = h_{k+1}/h_k$. In the eq. (4.29) the term $\tilde{f}_{exact}$ is called the generalized Richardson extrapolate.

The order of accuracy p cannot be calculated from only two discrete solutions. Hence, a third solution needs to be taken into account so the order of accuracy could be assessed. Thus, one introduces the third solution

$$f_3 = f_{exact} + g_p h_3^p + \mathcal{O}(h_3^{p+1}) \tag{4.30}$$

and after neglecting higher-order terms and rearranging an expression for p reads

$$p = \frac{\ln\left(\frac{\varepsilon_{32}}{\varepsilon_{21}}\right) + \ln\left(\frac{r_{21}^p - 1}{r_{32}^p - 1}\right)}{\ln r_{21}}, \tag{4.31}$$

where $\varepsilon_{21} = f_2 - f_1$ and $\varepsilon_{32} = f_3 - f_2$. The eq. (4.31) is transcendental in p and needs to be solved iteratively. For the case of constant grid refinement ratio when $r = r_{21} = r_{32}$, the eq. (4.31) simplifies to

$$p = \frac{\ln(\varepsilon_{32}/\varepsilon_{21})}{\ln r}. \tag{4.32}$$

4.3.1   Grid Convergence Index (GCI)

Grid Convergence Index (GCI) is a measure for quantifying how much the computed value is away from the value of the asymptotic numerical solution [26]. In order to calculate the GCI, the Richardson error estimators are introduced [23]:

$$E_1^{fine} = -g_p h_1^p = \frac{\varepsilon_{21}}{1 - r^p}, \tag{4.33}$$

$$E_2^{coarse} = -g_p h_2^p = -g_p h_1^p r^p = \frac{r^p \varepsilon_{21}}{1 - r^p}, \tag{4.34}$$

where E_1^{fine} is a fine-grid Richardson error estimator and approximates the error in a fine-grid solution (f_1) by comparing it to that of a coarse grid (f_2) and E_2^{coarse} is a coarse-grid Richardson error estimator that approximates the error in a coarse-grid solution (f_2) by comparing it to that of a fine grid (f_1).

Grid Convergence Index is calculated as

$$GCI_1^{fine} = F_s |E_1^{fine}|, \tag{4.35}$$

$$GCI_2^{coarse} = F_s |E_2^{coarse}|, \tag{4.36}$$

where F_s denotes a safety factor and it is recommended to take $F_s = 3$ for the case with two grids and $F_s = 1.25$ for the case with three or more grids [23]. Since all the test cases are calculated with five grids, the value $F_s = 1.25$ will be taken.

It is also possible to calculate the GCI with fractional Richardson error estimators which are obtained using relative errors $e_{21} = (f_2 - f_1)/f_1$ and $e_{32} = (f_3 - f_2)/f_2$

$$GCI_{21} = \frac{F_s |e_{21}|}{r_{21}^p - 1}, \tag{4.37}$$

$$GCI_{32} = \frac{F_s |e_{32}|}{r_{32}^p - 1}. \tag{4.38}$$

Both equations (4.37) and (4.38) give the GCI for the fine-grid error estimation and are applied in the following analysis.

It is important to check if the grid resolutions are within the asymptotic range of convergence. It can be done using following criterion:

$$\frac{GCI_{32}}{r^p GCI_{21}} \approx 1. \tag{4.39}$$

The disadvantage of the eq. (4.39) is that r refers to a constant grid refinement ratio, so in the case of fine-grid combination (see Section 6.3), the mathematical mean of r_{32} and r_{21} will be used instead of r, in the absence of better criterion.

Chapter 5

Simulation Parameters

In this chapter the simulation set-up will be presented for the validation test cases, presented in Chapter 6. The first section describes the grids used in the computation. The second section deals with numerical schemes applied for certain terms of the equations, which are implemented in the solver, and the third one gives the boundary conditions used in simulations.

5.1   Discretisation of the Computational Domain

In order to perform numerical simulations for all test cases, five uniform and structured two-dimensional grids have been generated, where the numbers of cells and cell sizes are presented in Table 5.1. The dimensionless time step has been set to $\Delta \hat{t} = 0.05$ for all simulations.

Grid name	Number of cells	Cell size ($\Delta x = \Delta y$)
40K	40 000 (200 $\times$ 200)	1
160K	160 000 (400 $\times$ 400)	0.5
360K	360 000 (600 $\times$ 600)	0.333
640K	640 000 (800 $\times$ 800)	0.25
1M	1 000 000 (1000 $\times$ 1000)	0.2

Table 5.1: List of grids for numerical simulations of all test cases.

5.2   Numerical Schemes

OpenFOAM software environment provides run-time selectable discretisation schemes that are required for discretization of the governing equations for propagation of acoustic waves.

Looking at the set of linearized Euler equations (3.21), (3.27) and (3.30), one can notice that the equations are the first-order partial differential equations and consist of the terms which contain time derivatives, gradients and divergences. Required numerical schemes are defined in `fvSchemes` dictionary, specifically its sub-dictionaries: `ddtSchemes`, `gradSchemes`, `divSchemes`, `interpolationSchemes` and `snGradSchemes`. Time-derivative terms are discretised with backward Euler implicit method that is second order accurate. Fourth order accurate gradient scheme is used for gradient terms. Divergence schemes are discretised with Gauss' theorem either using linear interpolation (for explicit terms) or linear upwind interpolation (for implicit terms).

Table 5.2 gives an overview of numerical schemes applied to all terms, where the word `Gauss` specifies the standard finite volume discretisation of Gaussian integration which requires the interpolation of values from cell centers to face centers. The surface normal gradient schemes have been set to `uncorrected`, because in all simulations the orthogonal grids have been used.

5.3   Boundary Conditions

For test cases with horizontal and diagonal mean flow *von Neumann* boundary condition is used on all boundaries:

$$\frac{\partial \Phi}{\partial n} = 0 \tag{5.1}$$

where Φ denotes a field and n is a surface normal on the boundary oriented outwards. *Von Neumann* (i.e. `zeroGradient`) boundary condition is chosen in the absence of better boundary condition (such as in 3.3) for a non-reflective boundary.

Reflective wall test case examines the effectiveness of wall boundary conditions and, therefore, contains three boundaries with *von Neumann* boundary conditions on all fields and one boundary (at $y = 0$) with wall boundary condition. To model the wall, Dirichlet boundary

Time-derivative schemes (ddtSchemes)	
default	backward

Gradient schemes (gradSchemes)	
default	fourth

Divergence schemes (divSchemes)	
div(rho*UPrime)	Gauss linear
div(gamma*p*rho*UPrime)	Gauss linear
div(phi,rhoPrime)	Gauss linearUpwind Gauss linear
div((rho*phi),rhoPrime)	Gauss linearUpwind Gauss linear
div(phi,pPrime)	Gauss linearUpwind Gauss linear

Interpolation schemes (interpolationSchemes)	
default	linear

Surface normal gradient schemes (snGradSchemes)	
default	uncorrected

Table 5.2: Numerical schemes used for all test cases.

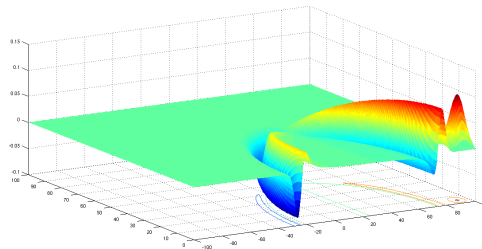condition is used for velocity

$$\hat{u}' = \hat{v}' = 0, \tag{5.2}$$

while the *von Neumann* boundary condition is used for $\hat{p}'$ and $\hat{\rho}'$

$$\frac{\partial p'}{\partial n} = \frac{\partial \rho'}{\partial n} = 0. \tag{5.3}$$

In the next chapter the results of the validation test cases will be presented, as well as the results of the simulation of noise generated by a mixing layer.

Chapter 6

Results & Discussion

In this chapter the results of all test cases will be presented. The first section gives numerical solutions and difference between analytical and numerical solutions for different time instances. In the second section the comparison of results of all test cases for time instant $\hat{t} = 50$ will be reported. The third section deals with the grid convergence error analysis for all test cases. In the fourth section, the equations, computational setup and results for the mixing layer simulation will be presented.

In this chapter, all variables ($\hat{p}'$, $\hat{\rho}'$, $\hat{u}'$, $\hat{v}'$ and $\hat{t}$) are dimensionless with scales defined in Section 4.2. For convenience, the abbrevations HMF test case (horizontal mean flow), DMF test case (diagonal mean flow) and RW test case (reflective wall) will often be used.

6.1 Results for Different Time Instants

In this section, for test cases with horizontal mean flow (HMF) and diagonal mean flow (DMF), numerically obtained acoustic fields of velocity fluctuation magnitude $|\hat{\mathbf{U}}'|$ and density fluctuation $\hat{\rho}'$ will be given for different time instants. In addition, the field of difference between

analytical and numerical solutions for $\hat{\rho}'$ will be given. For reflective wall (RW) test case, the fields of velocity fluctuation magnitude $|\hat{\mathbf{U}}'|$, pressure fluctuation $\hat{p}'$ and difference between analytical and numerical solutions for $\hat{p}'$ will be presented. All numerical solutions presented in this section are obtained using the finest grid, with 1 000 000 cells.

6.1.1 Test Case with Horizontal Mean Flow

Test cases HMF and DMF are used to examine the quality of numerical procedure for calculating acoustic, vorticity and entropy wave propagation. They are also used to test the effectiveness of the open boundary. In Section 4.2 the initial distribution of the acoustic fields $\hat{p}'$, $\hat{\rho}'$, $\hat{u}'$ and $\hat{v}'$ is given in order to numerically solve the initial value problem by using linearised Euler equations (3.21), (3.27) and (3.30).

Figures 6.1.2, 6.1.3, 6.1.4, 6.1.5, 6.1.6 show three fields for various times: The first row contains the velocity fluctuation magnitude $|\hat{\mathbf{U}}'| = \sqrt{\hat{u}'^2 + \hat{v}'^2}$, the second row contains the density fluctuation $\hat{\rho}'$ and the third row contains the difference between analytical and numerical solutions for $\hat{\rho}'$, $\Delta\rho'$. Each column represents the three fields at the corresponding time (shown on top of the figures). Acoustic and entropy waves are presented by the field of density fluctuation $\hat{\rho}'$ and the vorticity wave by the field of velocity fluctuation magnitude $|\hat{\mathbf{U}}'|$. Pressure fluctuation fields $\hat{p}'$ are not shown in the figures, because they look exactly the same when the entropy wave leaves the domain, as shown in Figure 6.1.1.

In figures 6.1.2 and 6.1.3 the propagation of acoustic wave through the computational domain and convection of vorticity and entropy pulses are shown. The acoustic wave is initiated at the center of the domain at $\hat{t} = 0$, whereas the vorticity and entropy waves are initiated downstream of the acoustic wave, on two thirds of the distance between the acoustic wave and the outflow boundary. Vorticity wave can be seen in the field of $|\hat{\mathbf{U}}'|$ on the right half of the domain, and entropy wave in the field of $\hat{\rho}'$, also on the right half of the domain. The wavefront of the acoustic pulse expands radially, but due to the mean flow velocity the whole wave is convected downstream at the same time. Entropy and vorticity pulses are convected by the mean flow velocity without the change in shape or amplitude.

The first column in Figure 6.1.2 shows the fields of $|\hat{\mathbf{U}}'|$, $\hat{\rho}'$ and $\Delta\rho'$ at time $\hat{t} = 0$. It is noted that the initial distribution of acoustic field variables calculated using the grid with
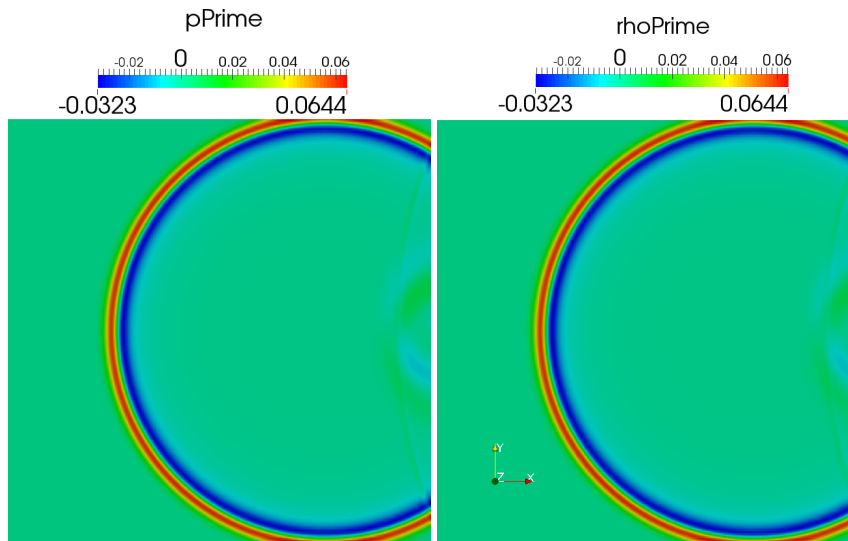
Figure 6.1.1: Comparison between solutions of $\hat{p}'$ and $\hat{\rho}'$ at time $\hat{t} = 100$, HMF test case.

1000000 cells does not provide exact values of the initial variable distribution, even though no numerical procedure has been applied yet. This occurs due to even numbers of cells (1000) for each coordinate, so no cell center is located at $x = 0$, $y = 0$. It has been observed that this error does not affect the solutions noticeably, so the analysis of that error has not been conducted. To obtain initial distributions of the field variables, the numerical calculation of the LEEs is not needed, so no error has been introduced by solving the LEEs, as shown in the field $\Delta\rho'$ at time $\hat{t} = 0$.

In the last two columns of the Figure 6.1.2 and the first column of the Figure 6.1.3 the fields of $\Delta\rho'$ show the values that are generated mostly by small phase shift between the two solutions, due to large gradients of numerically and analytically obtained fields of $\hat{\rho}'$ (see Section 6.2).

The second column in the Figure 6.1.3 shows three fields just after all three waves reach the outflow boundary at time $\hat{t} = 70$ (the time until the waves reach the boundary is $\hat{t} = 66.67$). Figures 6.1.4 and 6.1.5 show further propagation of acoustic wavefront towards the side and inflow boundaries, whereas the vorticity and entropy wave entirely leave the domain. On this figure the spurious reflections from the boundaries of the domain can be seen and are especially detectable on the fields of differences $\Delta\rho'$ (bottom row). At time $\hat{t} = 280$ near the side boundaries, the wave reflected for the second time can be seen and contains larger values of acoustic variables than the one-time-reflected waves do.

The Figure 6.1.6 shows three fields at time instants $\hat{t} = 400$, $\hat{t} = 480$ and $\hat{t} = 600$. The scale

range of the fields of differences has increased more than 10 times, compared to the one of the Figure 6.1.5 at $\hat{t} = 280$. That could be caused by the fact that as the acoustic wave expands, its curvature gets smaller and as the incidence angle of the wave and the boundary approaches to zero, the reflected wave takes nearly the same position and superposes with the incident wave.

It can also be noted that for later times the fields of differences and density fluctuation agree well, concluding that the domain nearly contains only spurious reflected waves.
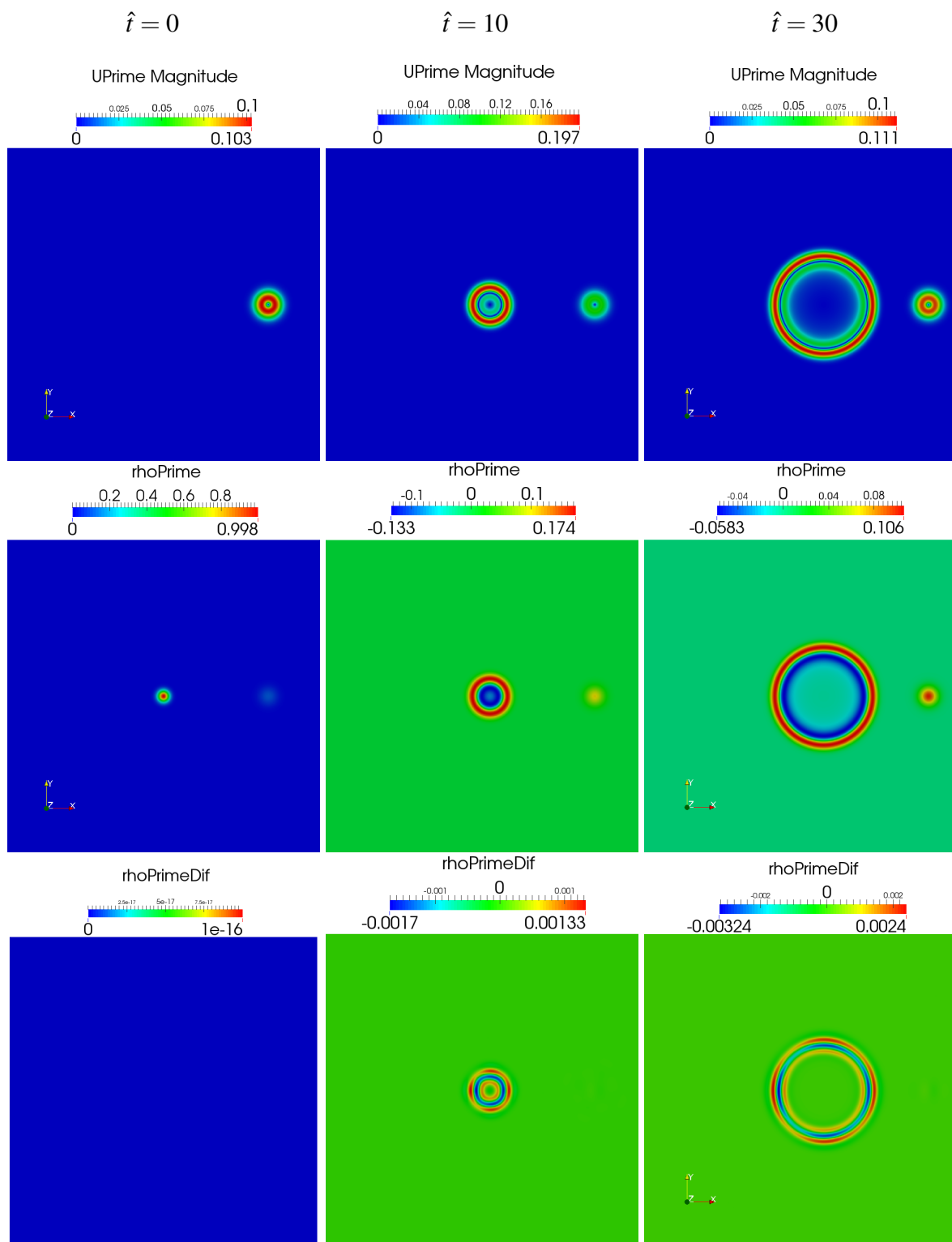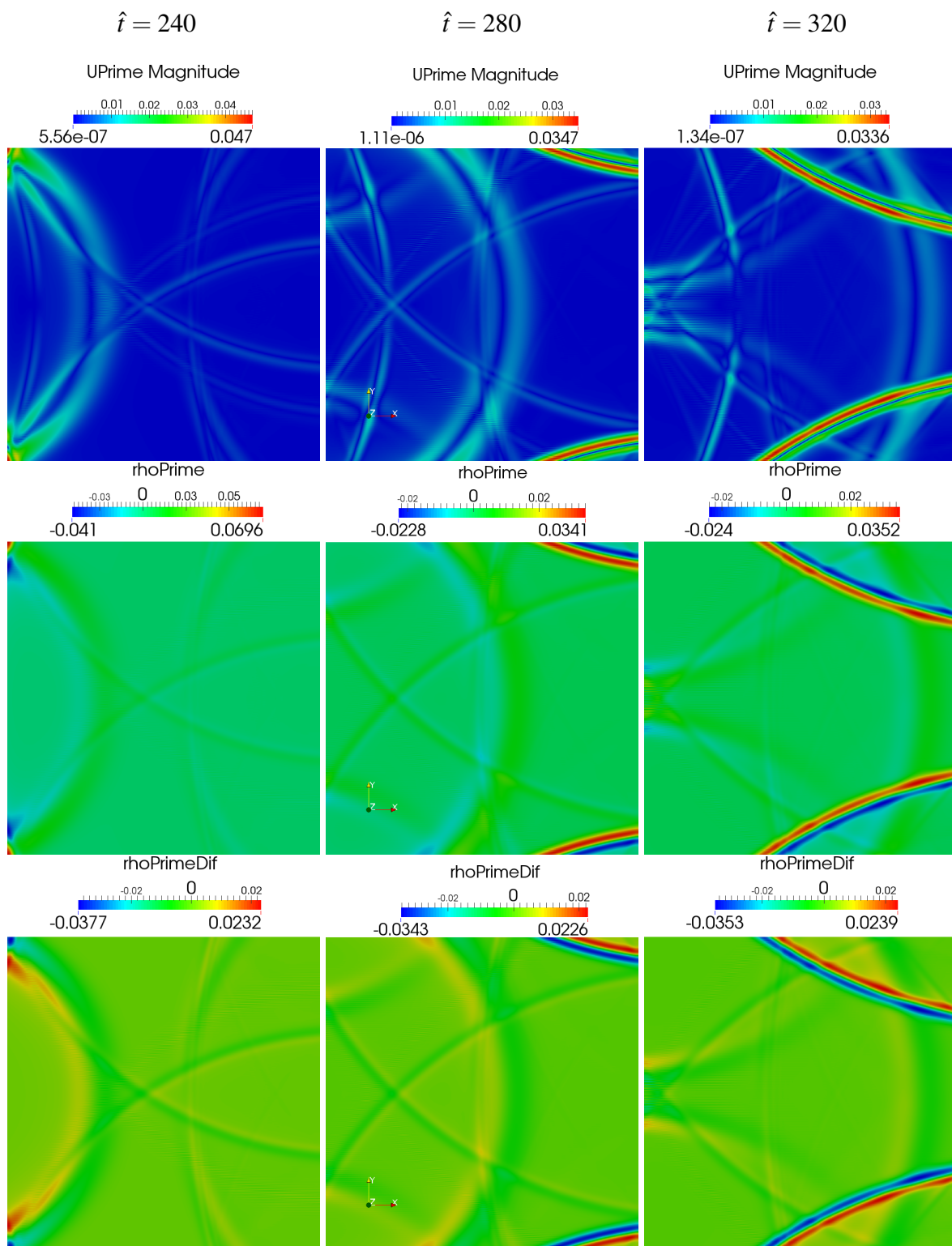
Figure 6.1.2: Acoustic fields: velocity fluctuation magnitude, $|\hat{\mathbf{U}}'|$ (top), density fluctuation, $\hat{\rho}'$ (middle), difference between $\hat{\rho}'_{analytical}$ and $\hat{\rho}'_{numerical}$ (bottom), 1 000 000 cell grid.
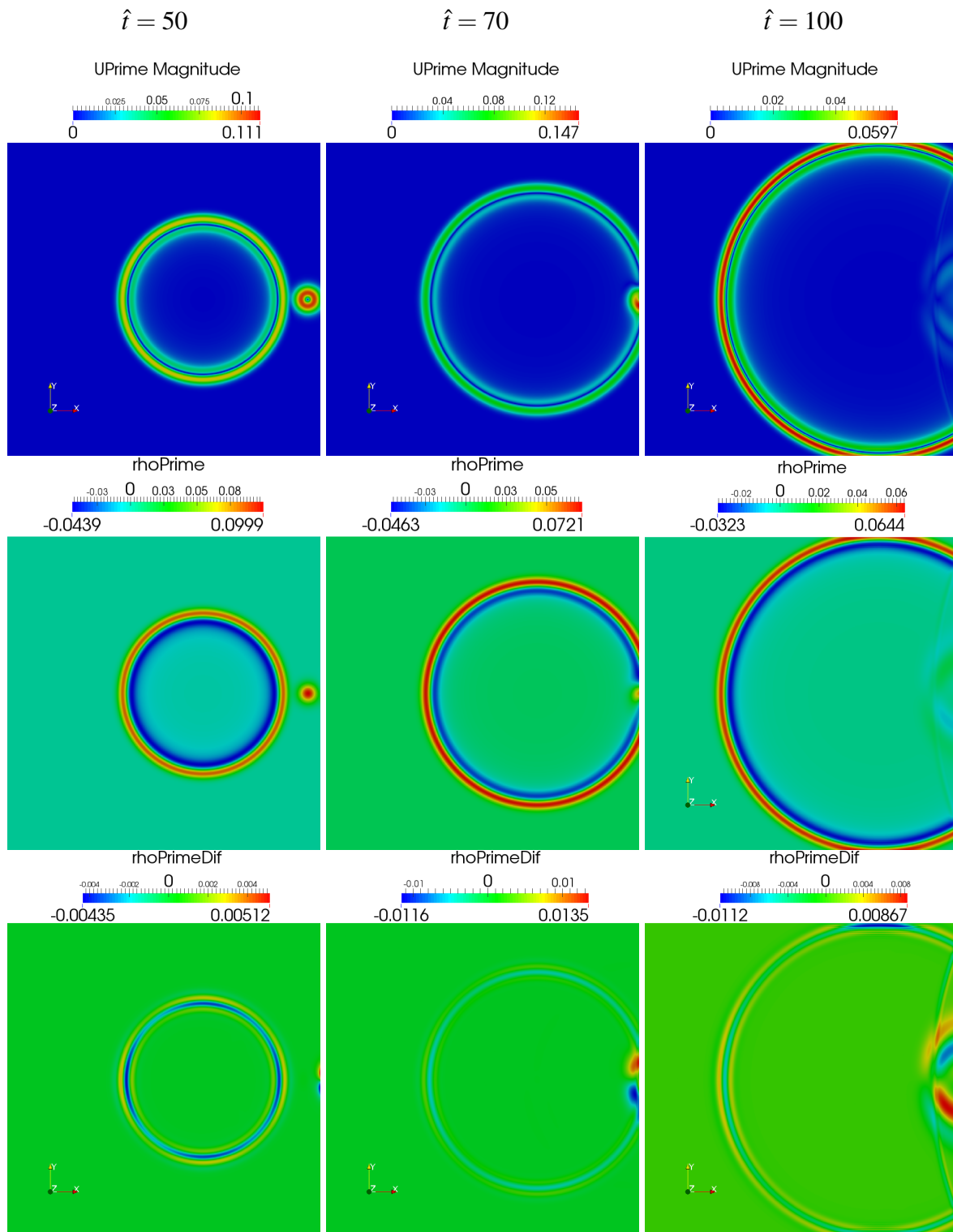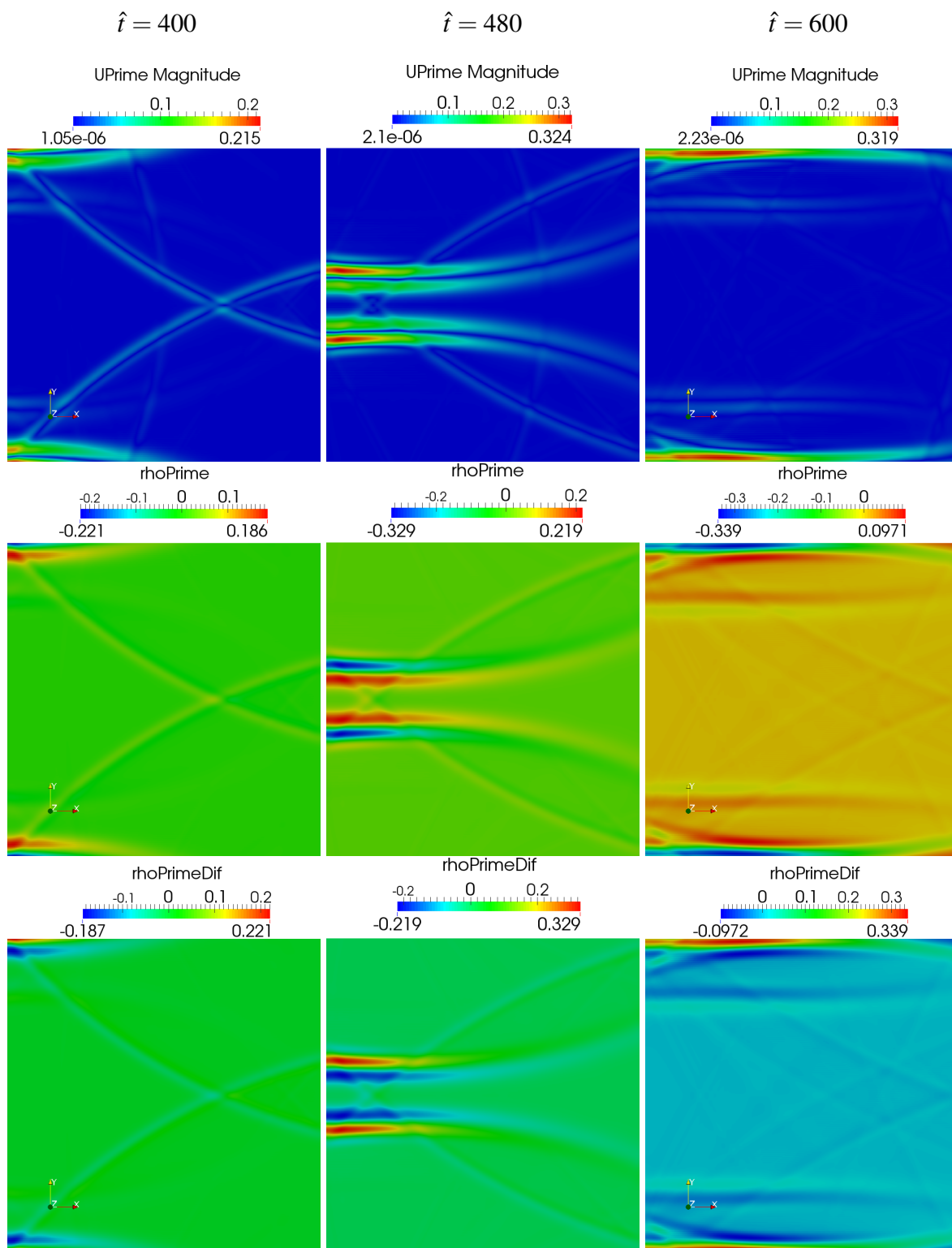
Figure 6.1.3: Acoustic fields: velocity fluctuation magnitude, $|\hat{\mathbf{U}}'|$ (top), density fluctuation, $\hat{\rho}'$ (middle), difference between $\hat{\rho}'_{analytical}$ and $\hat{\rho}'_{numerical}$ (bottom), 1 000 000 cell grid.
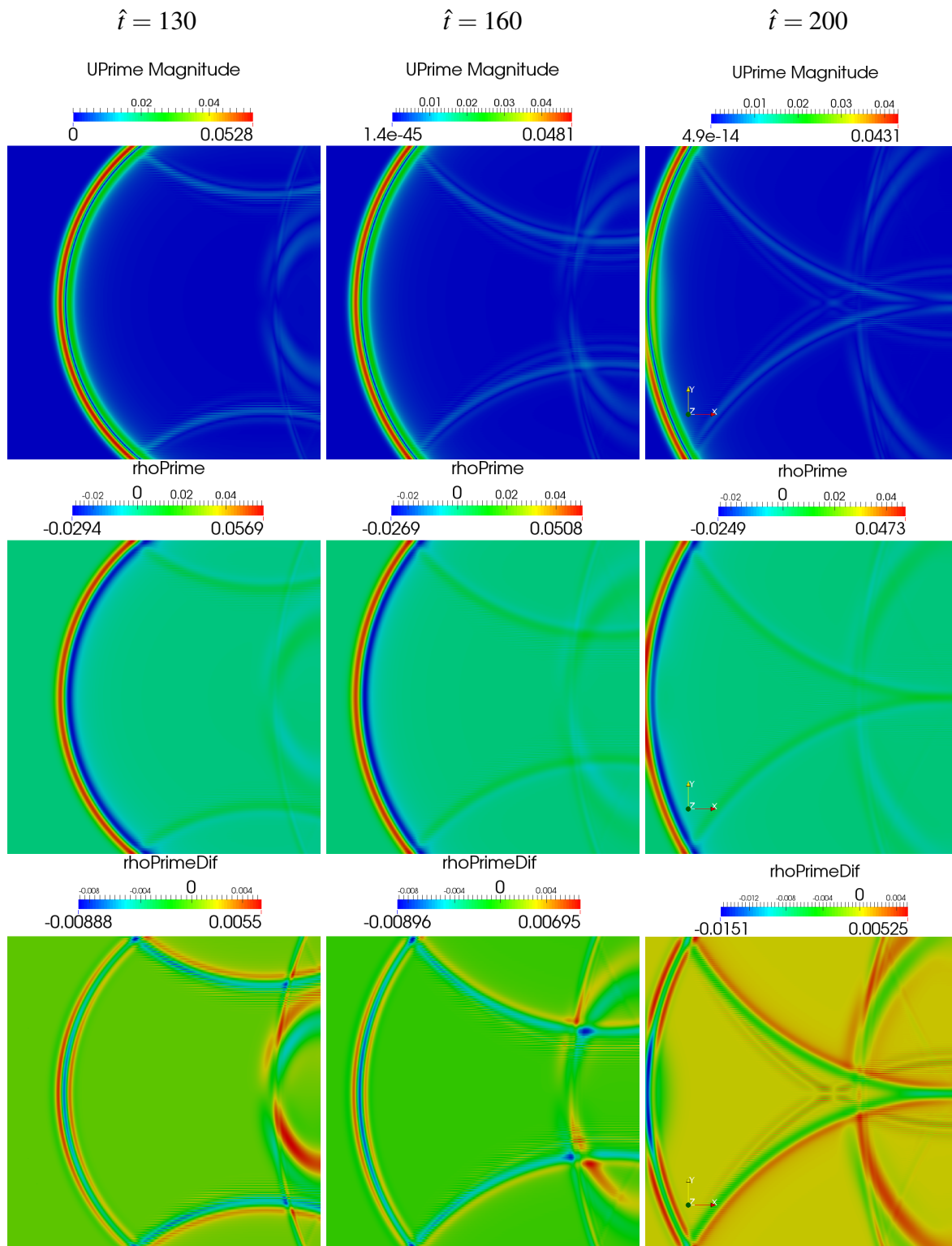
Figure 6.1.4: Acoustic fields: velocity fluctuation magnitude, $|\hat{\mathbf{U}}'|$ (top), density fluctuation, $\hat{\rho}'$ (middle), difference between $\hat{\rho}'_{analytical}$ and $\hat{\rho}'_{numerical}$ (bottom), 1 000 000 cell grid.

Figure 6.1.5: Acoustic fields: velocity fluctuation magnitude, $|\hat{\mathbf{U}}'|$ (top), density fluctuation, $\hat{\rho}'$ (middle), difference between $\hat{\rho}'_{analytical}$ and $\hat{\rho}'_{numerical}$ (bottom), 1 000 000 cell grid.

Figure 6.1.6: Acoustic fields: velocity fluctuation magnitude, $|\hat{\mathbf{U}}'|$ (top), density fluctuation, $\hat{\rho}'$ (middle), difference between $\hat{\rho}'_{analytical}$ and $\hat{\rho}'_{numerical}$ (bottom), 1 000 000 cell grid.

6.1.2 Test Case with Diagonal Mean Flow

Figures 6.1.7 and 6.1.8 show propagation and convection of acoustic, vorticity and entropy wave analogously as in previous subsection, with the difference that they are convected diagonally by the mean velocity. As described in Section 6.1.1, initial fields show a small deviation from an exact variable distribution, due to discretisation. In the bottom row of the Figure 6.1.8, which shows the field of numerical error for $\hat{\rho}'$, at $\hat{t} = 80$, it can be noted in the right upper corner of the domain that an open boundary generates an error, which is greater than the one present at the acoustic wavefront. Acoustic field $\hat{p}'$ is not shown because it is not different from the field of $\hat{\rho}'$ for later time instants. The only difference is in the fact that the field of $\hat{\rho}'$ contains the entropy wave.

Figures 6.1.9 and 6.1.10 show further propagation and reflections of acoustic wave. The field of differences at $\hat{t} = 200$ shows that second-time-reflected waves contain larger values, compared to the waves that are reflected once. The same field at $\hat{t} = 300$ shows the effect of increasing the magnitudes of acoustic variables in the waves with small incidence angles (described in previous subsection).

In Figure 6.1.11 all three fields for all chosen time instances show that the domain contains only spurious reflected waves that grow in their magnitudes as time changes.
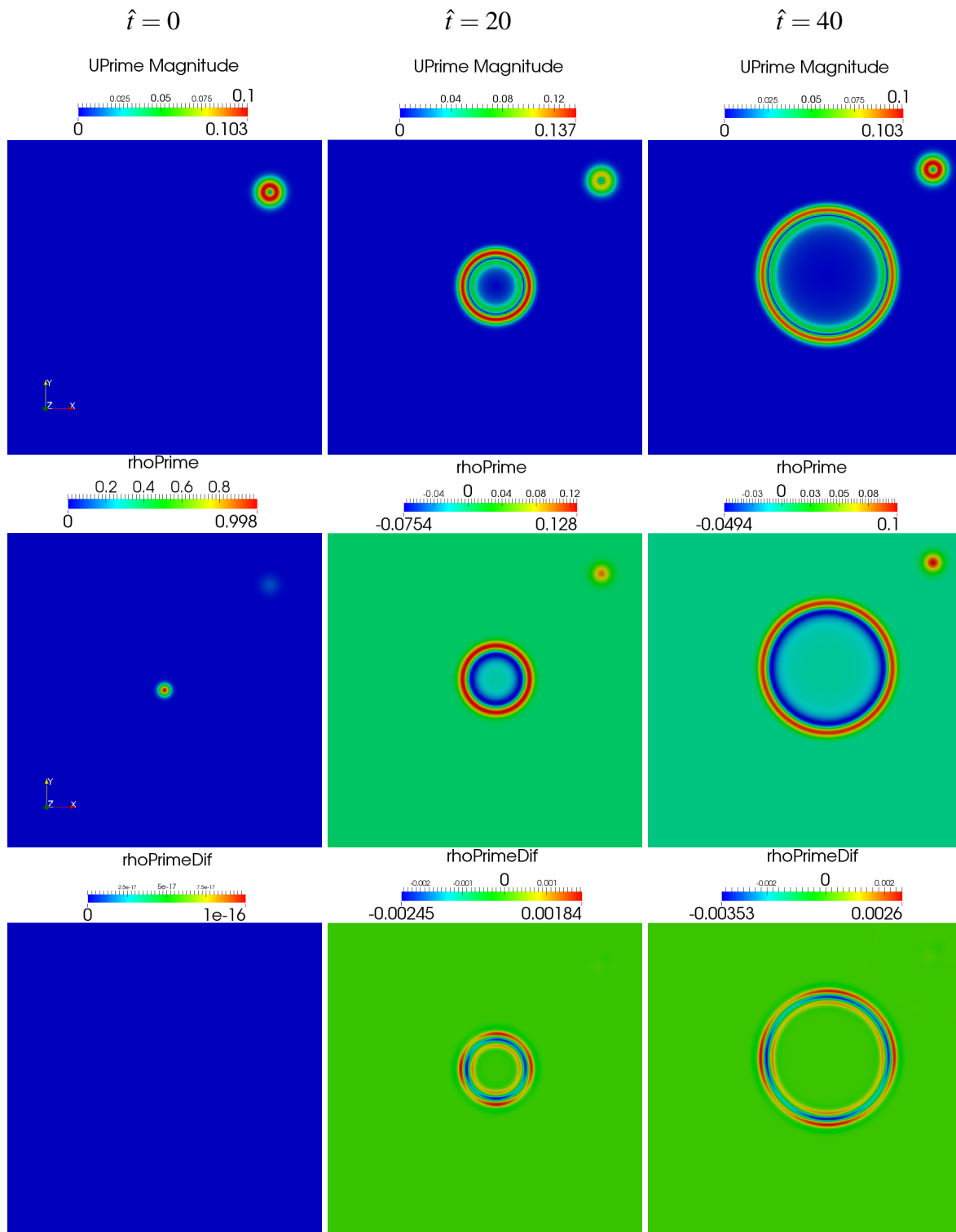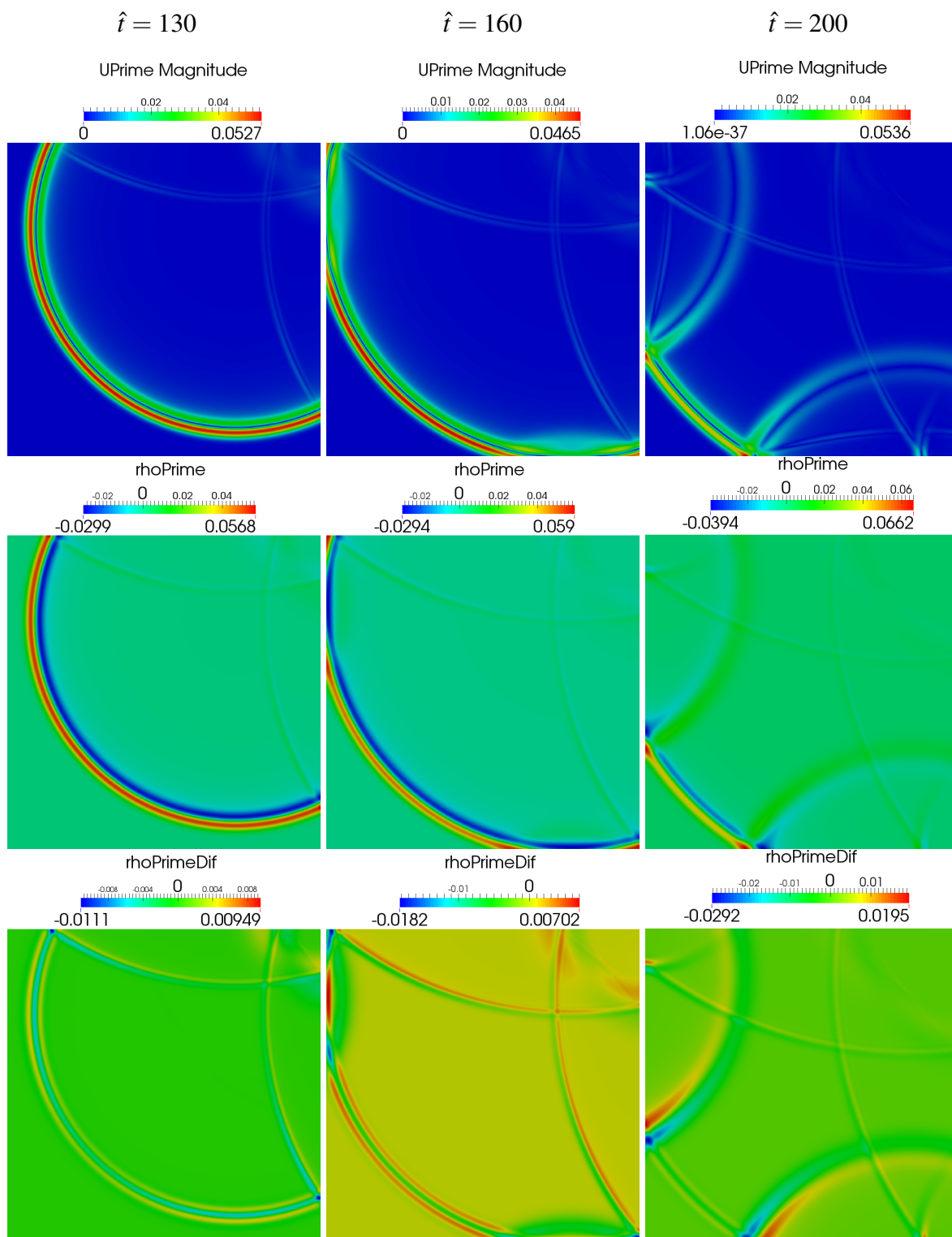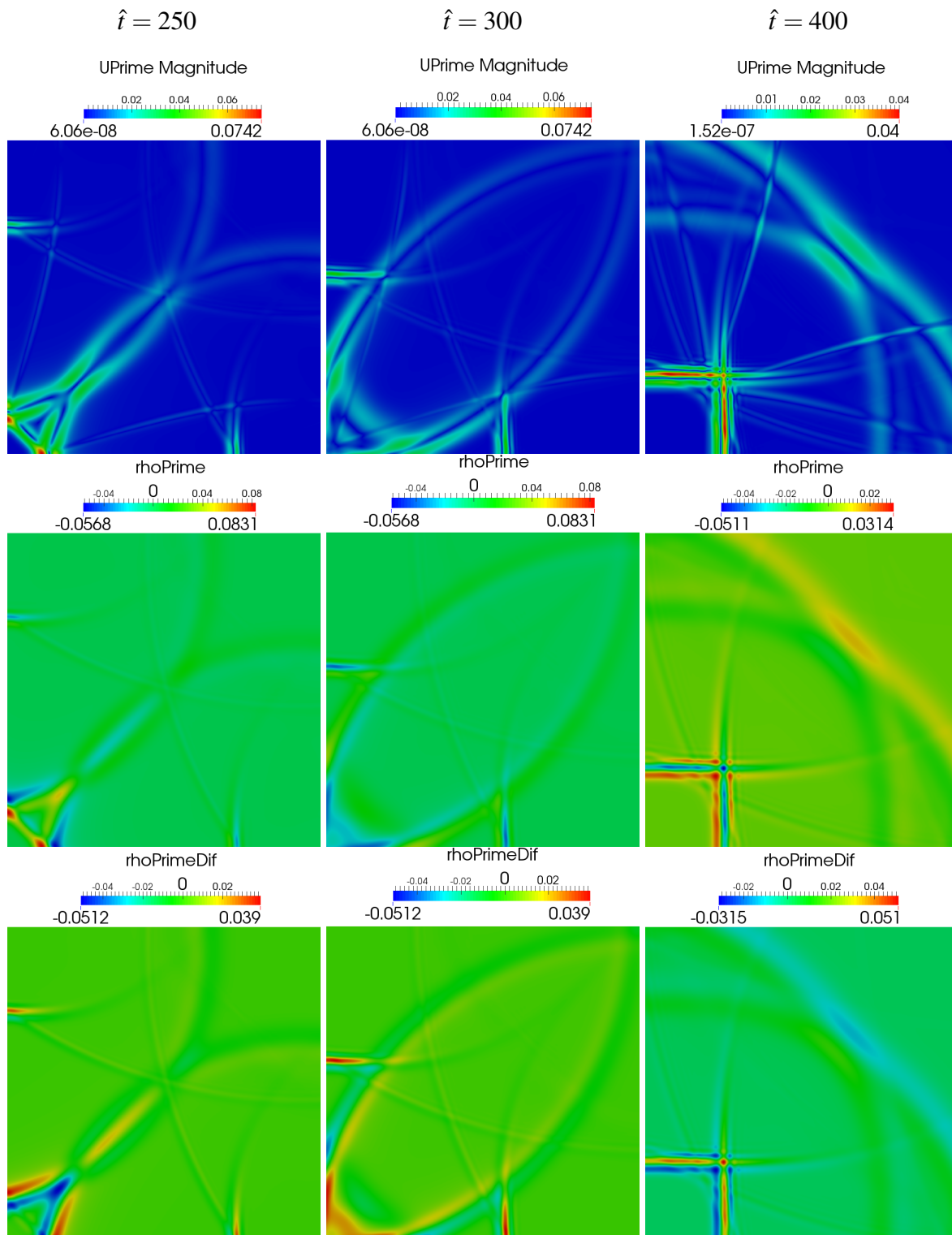
Figure 6.1.7: Acoustic fields: velocity fluctuation magnitude, $|\hat{\mathbf{U}}'|$ (top), density fluctuation, $\hat{\rho}'$ (middle), difference between $\hat{\rho}'_{analytical}$ and $\hat{\rho}'_{numerical}$ (bottom), 1 000 000 cell grid.
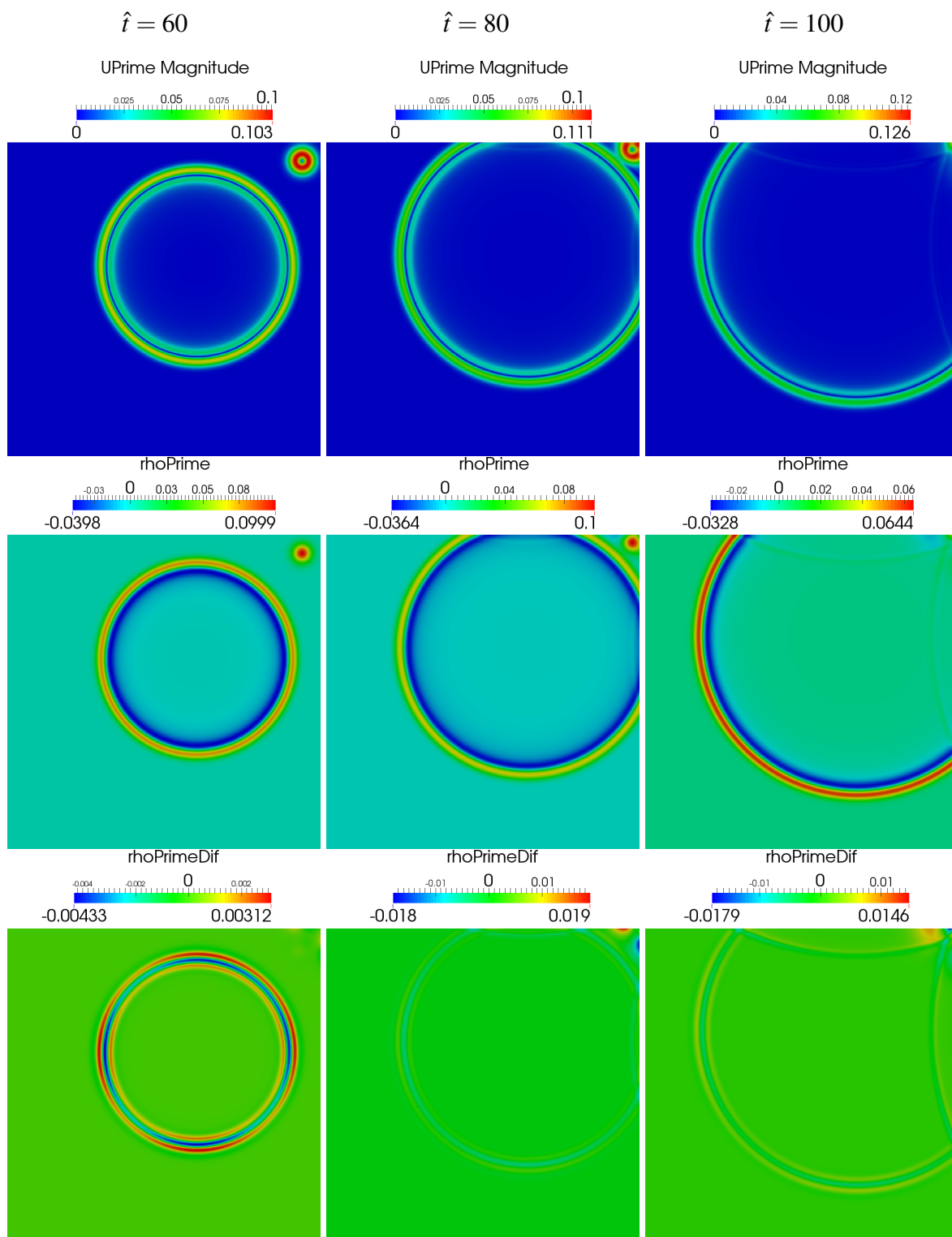
Figure 6.1.8: Acoustic fields: velocity fluctuation magnitude, $|\hat{\mathbf{U}}'|$ (top), density fluctuation, $\hat{\rho}'$ (middle), difference between $\hat{\rho}'_{analytical}$ and $\hat{\rho}'_{numerical}$ (bottom), 1 000 000 cell grid.
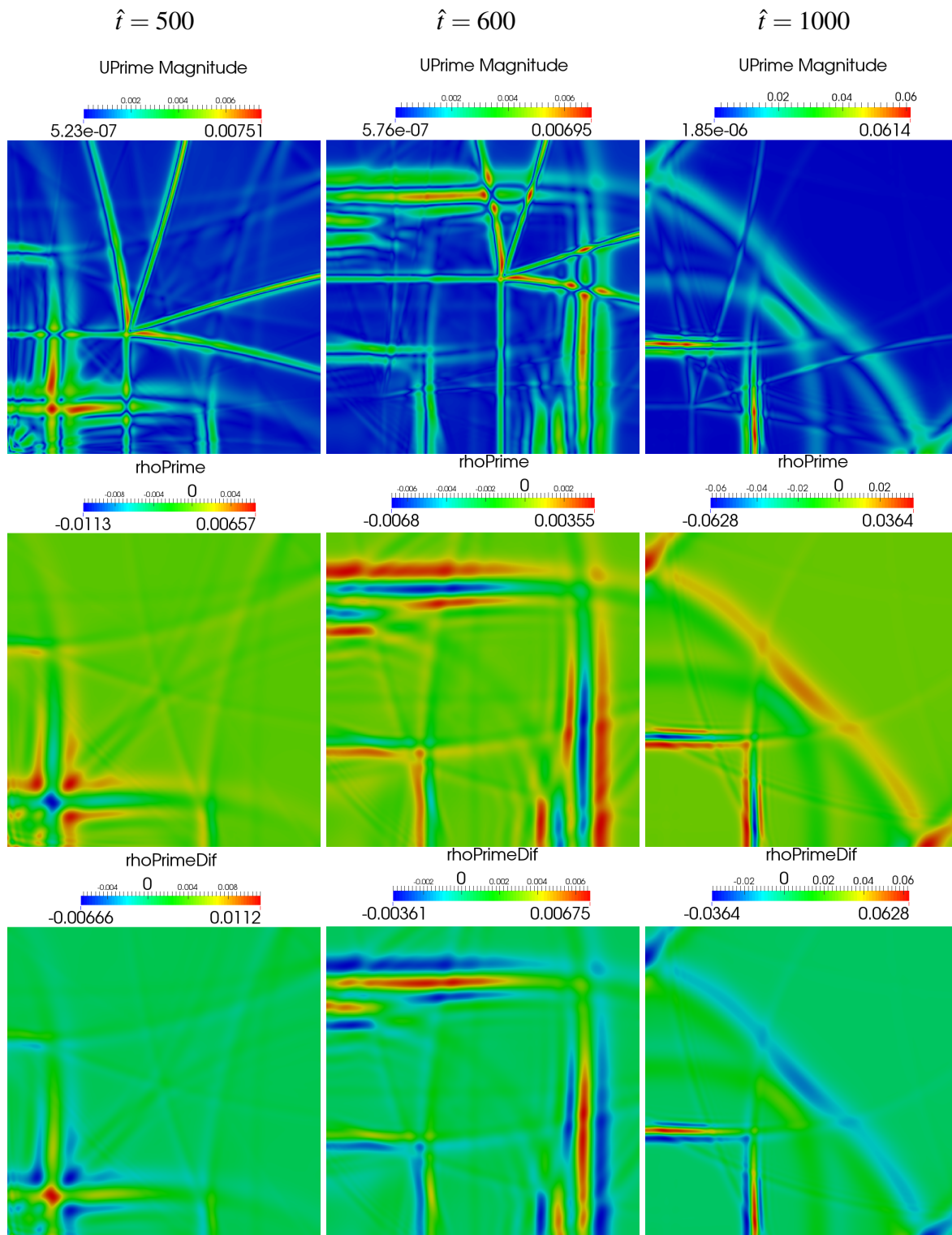
Figure 6.1.9: Acoustic fields: velocity fluctuation magnitude, $|\hat{\mathbf{U}}'|$ (top), density fluctuation, $\hat{\rho}'$ (middle), difference between $\hat{\rho}'_{analytical}$ and $\hat{\rho}'_{numerical}$ (bottom), 1 000 000 cell grid.

Figure 6.1.10: Acoustic fields: velocity fluctuation magnitude, $|\hat{\mathbf{U}}'|$ (top), density fluctuation, $\hat{\rho}'$ (middle), difference between $\hat{\rho}'_{analytical}$ and $\hat{\rho}'_{numerical}$ (bottom), 1 000 000 cell grid.

Figure 6.1.11: Acoustic fields: velocity fluctuation magnitude, $|\hat{\mathbf{U}}'|$ (top), density fluctuation, $\hat{\rho}'$ (middle), difference between $\hat{\rho}'_{analytical}$ and $\hat{\rho}'_{numerical}$ (bottom), 1 000 000 cell grid.

6.1.3   Test Case with Reflective Wall

Test case with reflective wall (RW) is used to test the wall boundary condition for the acoustic wave reflection. In Section 4.2 the initial distribution of the acoustic fields $\hat{p}'$, $\hat{\rho}'$, $\hat{u}'$ and $\hat{v}'$ is given in order to numerically solve the initial value problem by using linearised Euler equations (3.21), (3.27) and (3.30).

Because of the fact that the solutions of $\hat{p}'$ and $\hat{\rho}'$ are exactly the same (Figure 6.1.12), results that describe propagation only of acoustic wave will be shown in terms of velocity fluctuation magnitude field $|\hat{\mathbf{U}}'|$, pressure fluctuation field $\hat{p}'$ and the field of difference between analytically and numerically obtained $\hat{p}'$.
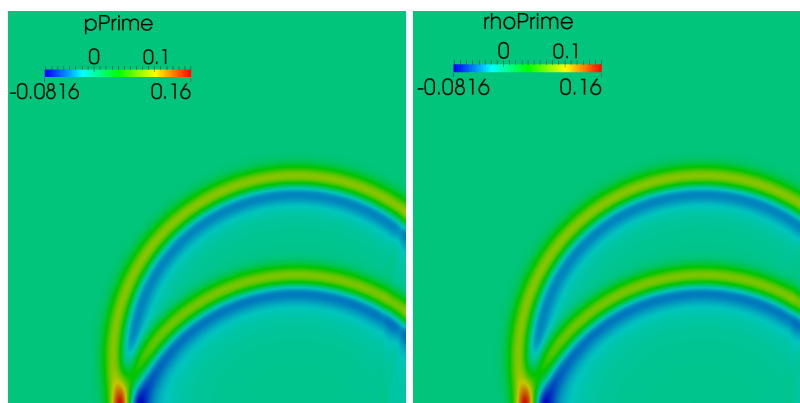

Figure 6.1.12: Comparison between solutions of $\hat{p}'$ and $\hat{\rho}'$ at time $\hat{t} = 90$, RW test case.

As stated in Section 4.2, vorticity pulse is not present at $\hat{t} = 0$ (there is no velocity fluctuation field), what is in accordance with the field of $|\hat{\mathbf{U}}'|$ at $\hat{t} = 0$, shown in the left column of Figure 6.1.13.

Figures 6.1.13 and 6.1.14 show radiation and convection of the acoustic wave, as well as its reflection off the wall. The fields of differences show a good agreement between analytical and numerical solutions for non-reflected wave and the wave reflected off the wall.

In Figure 6.1.15 the fields of differences show the waves that are small in their amplitudes, even in the case of spurious reflected waves. These waves are reflected once and do not make noticeable difference compared to ones from test cases with horizontal and diagonal mean flow.
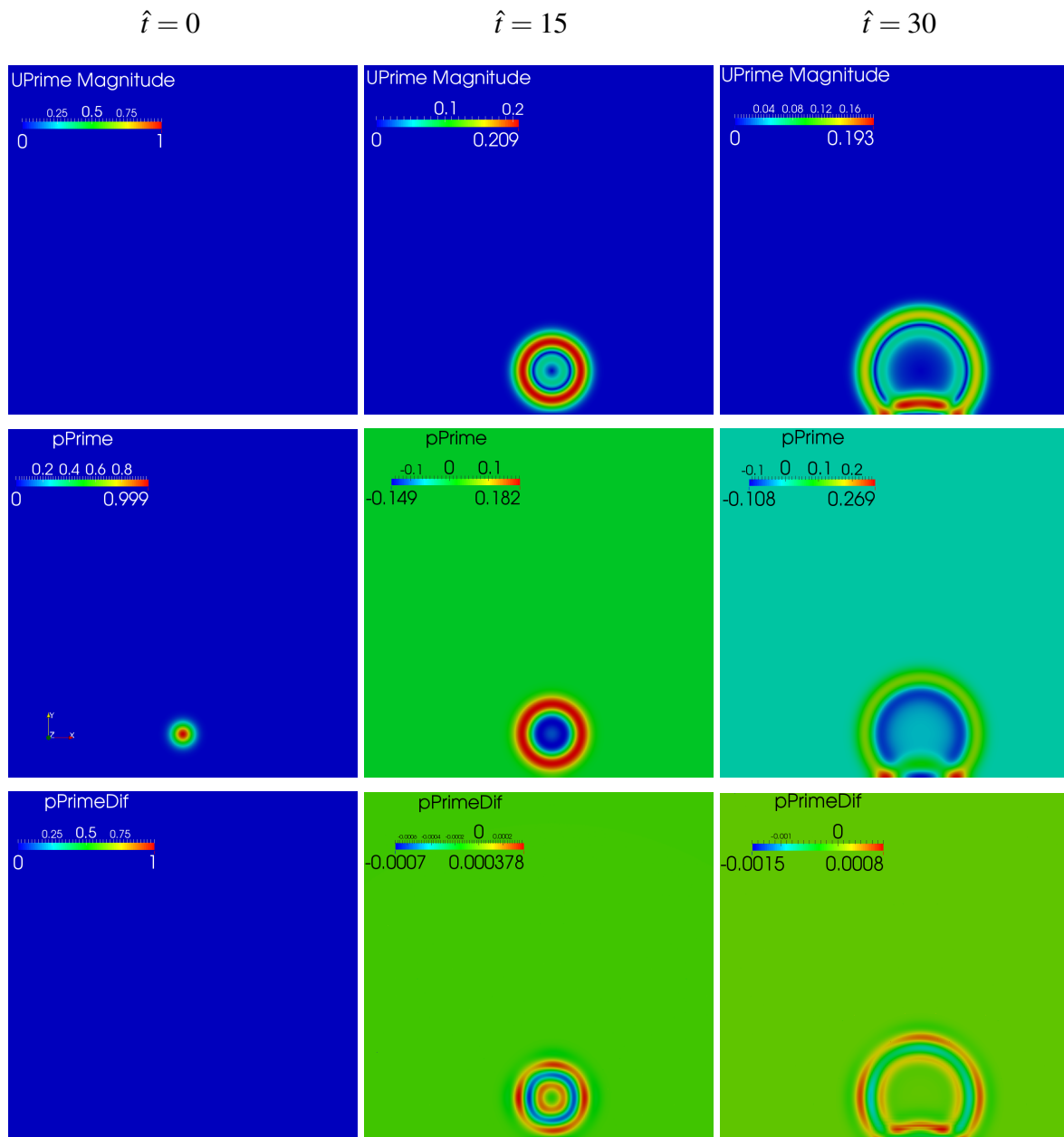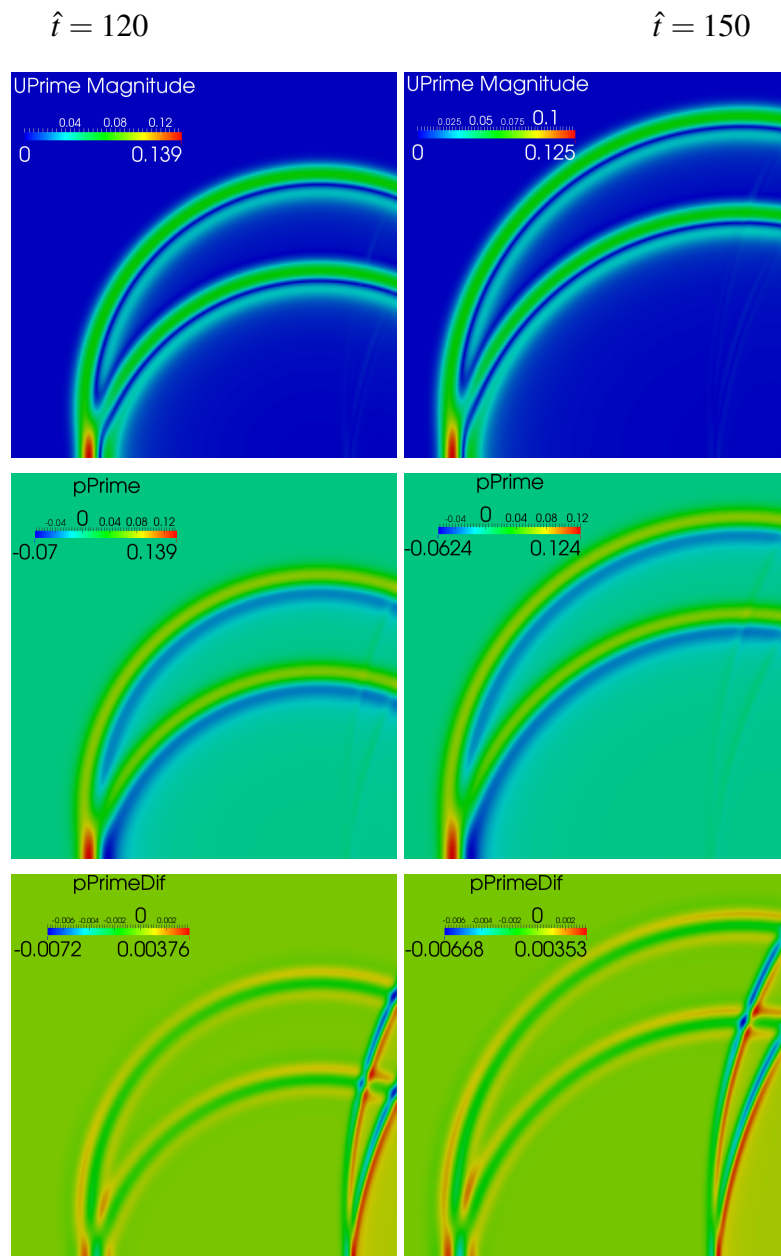
Figure 6.1.13: Acoustic fields: velocity fluctuation magnitude, $|\hat{\mathbf{U}}'|$ (top), pressure fluctuation, $\hat{p}'$ (middle), difference between $\hat{p}'_{analytical}$ and $\hat{p}'_{numerical}$ (bottom), 1 000 000 cell grid.
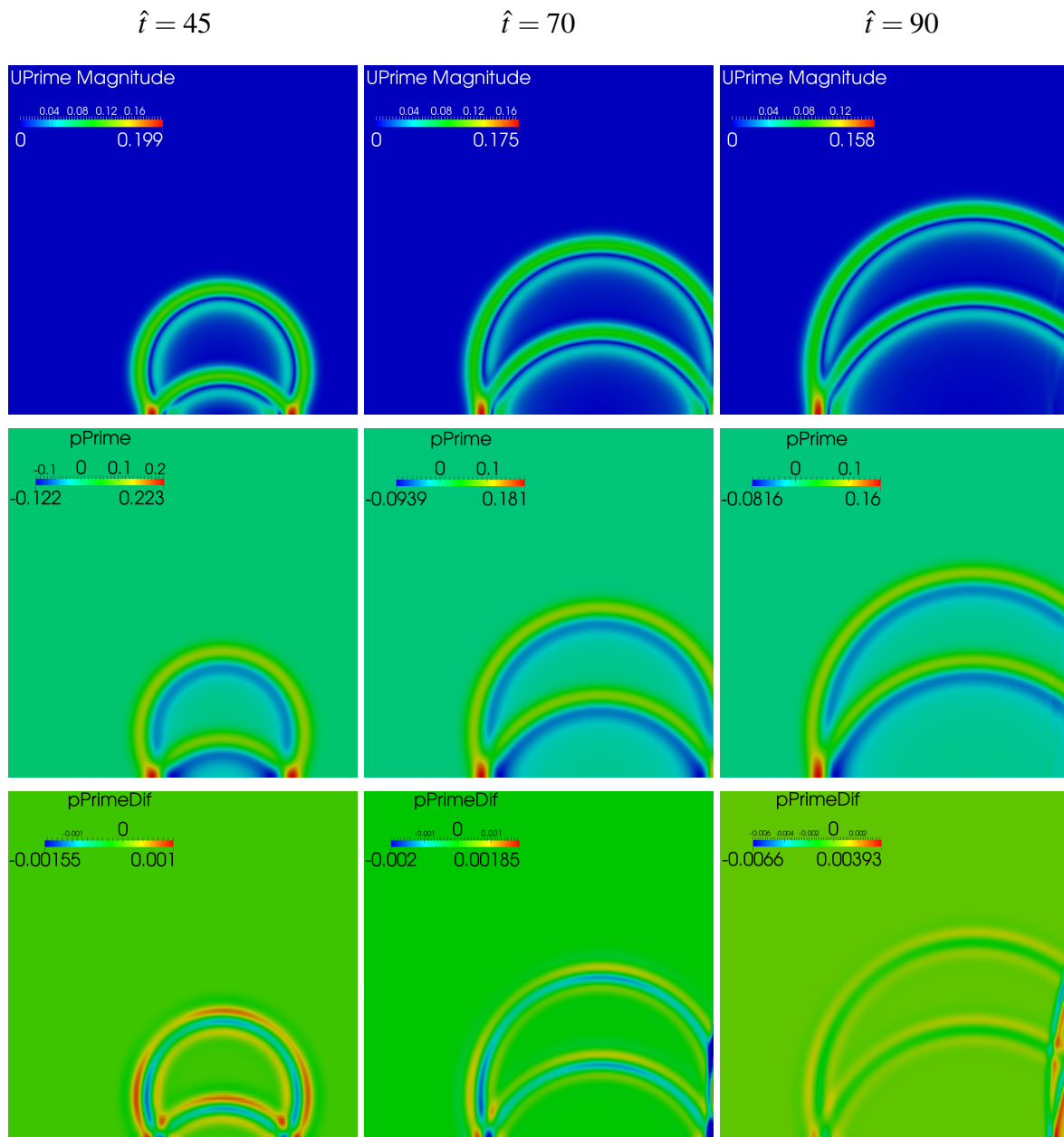
Figure 6.1.14: Acoustic fields: velocity fluctuation magnitude, $|\hat{\mathbf{U}}'|$ (top), pressure fluctuation, $\hat{p}'$ (middle), difference between $\hat{p}'_{analytical}$ and $\hat{p}'_{numerical}$ (bottom), 1 000 000 cell grid.

$\hat{t} = 120$ $\hat{t} = 150$
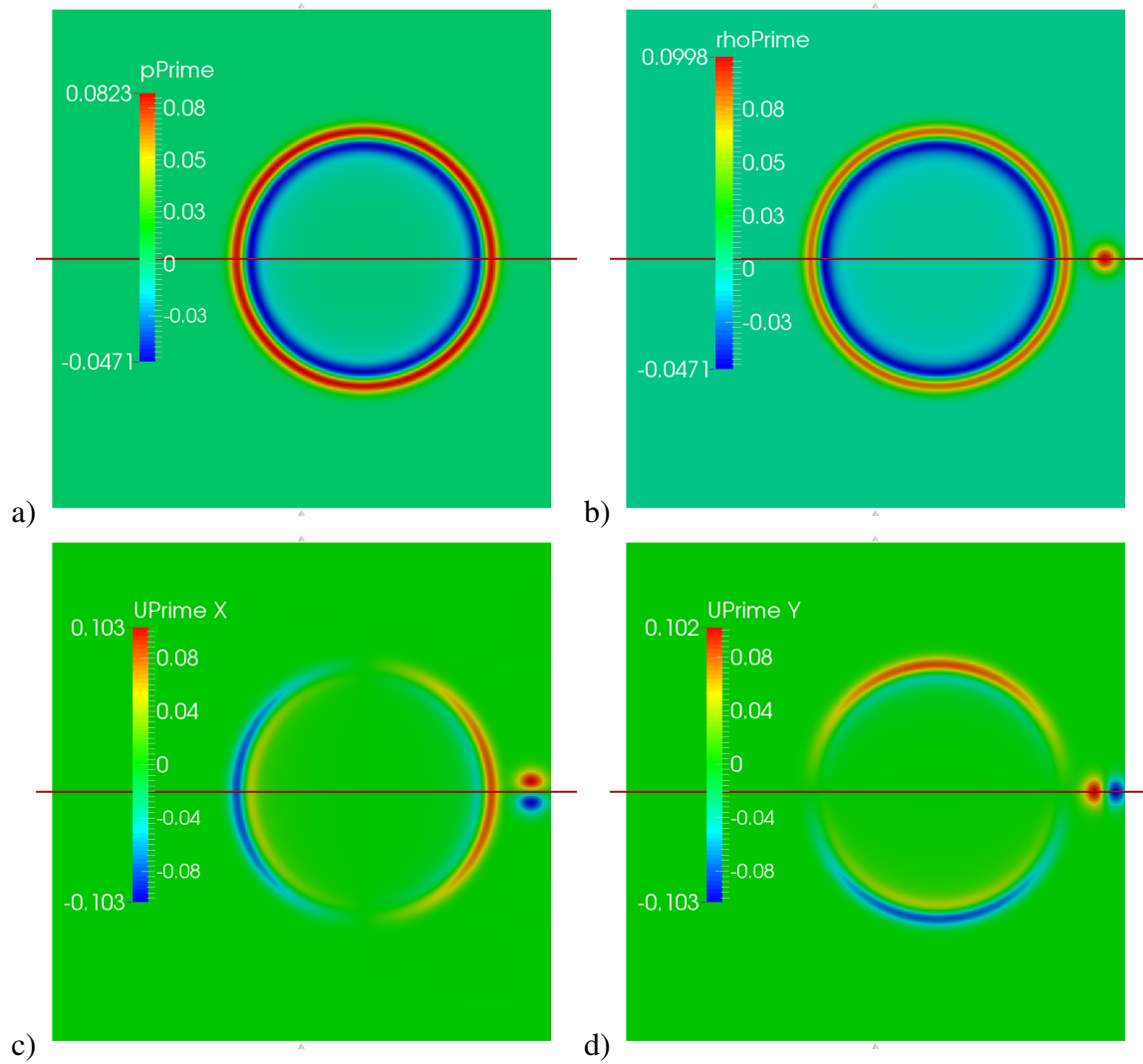

Figure 6.1.15: Acoustic fields: velocity fluctuation magnitude, $|\hat{\mathbf{U}}'|$ (top), pressure fluctuation, $\hat{p}'$ (middle), difference between $\hat{p}'_{analytical}$ and $\hat{p}'_{numerical}$ (bottom), 1 000 000 cell grid.

6.2   Comparison for Time $\hat{t} = 50$

For test cases with horizontal and diagonal mean flow, time $\hat{t} = 50$ is chosen because the waves have not reached the boundaries yet, so only the wave convection and radiation could be verified and validated, without the contamination of solutions caused by spurious wave reflections. For reflective wall test case, the acoustic wave reflection off the wall has already happened at $\hat{t} = 50$, but the requirement that the wave should not reach open boundaries is respected.

6.2.1   Test Case with Horizontal Mean Flow

In order to compare numerical and analytical solutions, as well as numerical solutions on different grids, the dimensionless time is fixed at $\hat{t} = 50$. The Figure 6.2.1 shows computed acoustic fields: pressure fluctuation $\hat{p}'$, density fluctuation $\hat{\rho}'$ and velocity fluctuation components $\hat{u}'$ and $\hat{v}'$ at time $\hat{t} = 50$ on the grid with 360 000 cells. The horizontal lines (at $y = 0$) define the slices through which the acoustic fields are examined in the following figures.

Figure 6.2.1: Acoustic fields a) $\hat{p}'$, b) $\hat{\rho}'$, c) $\hat{u}'$ and d) $\hat{v}'$ at time $\hat{t} = 50$ on the grid with 360 000 cells.
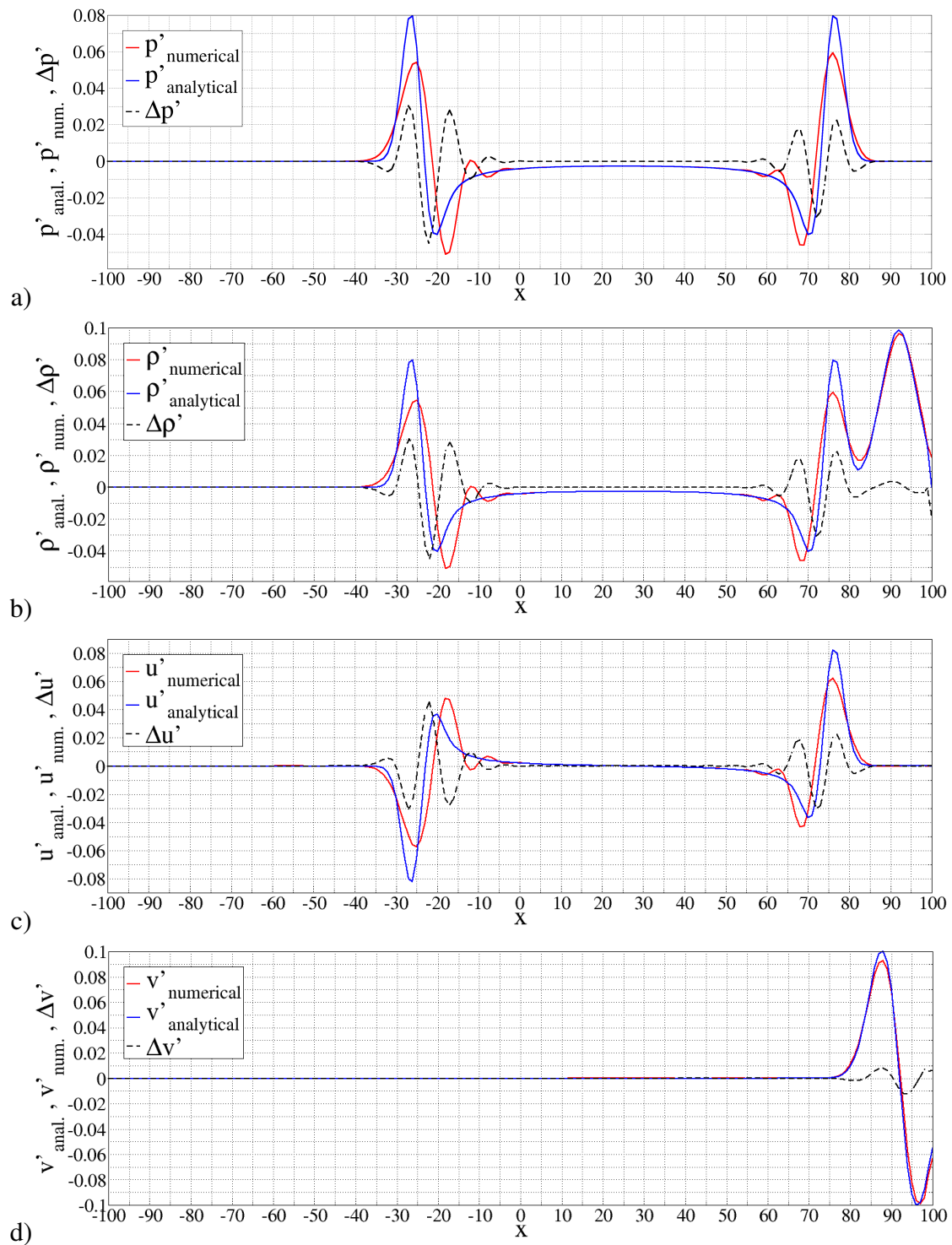
Figure 6.2.2: Acoustic variables: fluctuation of a) pressure $\hat{p}'$, b) density $\hat{\rho}'$ and velocity components c) $\hat{u}'$ and d) $\hat{v}'$ at time $\hat{t} = 50$, $y = 0$, 40 000 cell grid, HMF test case.
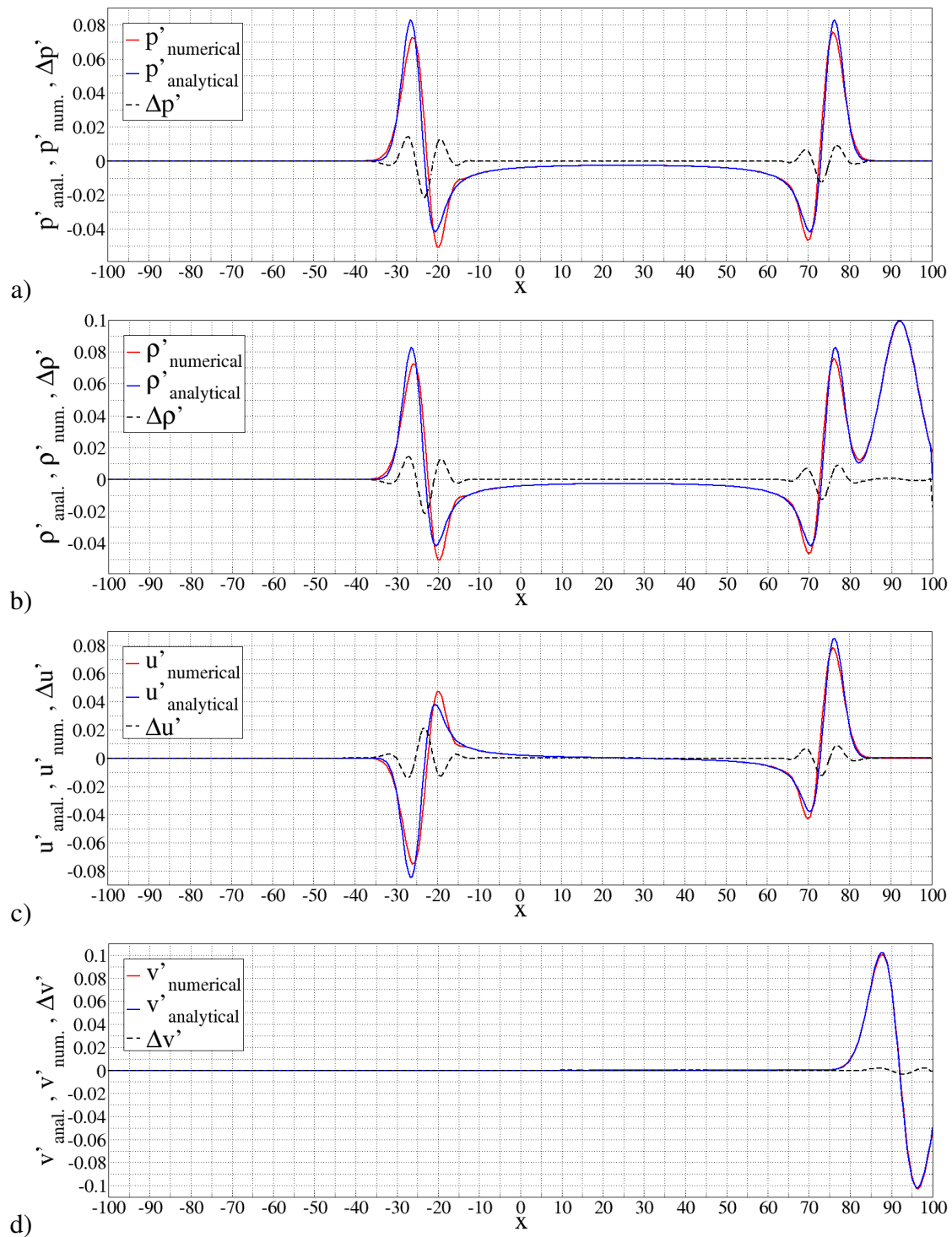
Figure 6.2.3: Acoustic variables: fluctuation of a) pressure $\hat{p}'$, b) density $\hat{\rho}'$ and velocity components c) $\hat{u}'$ and d) $\hat{v}'$ at time $\hat{t} = 50$, $y = 0$, 160 000 cell grid, HMF test case.
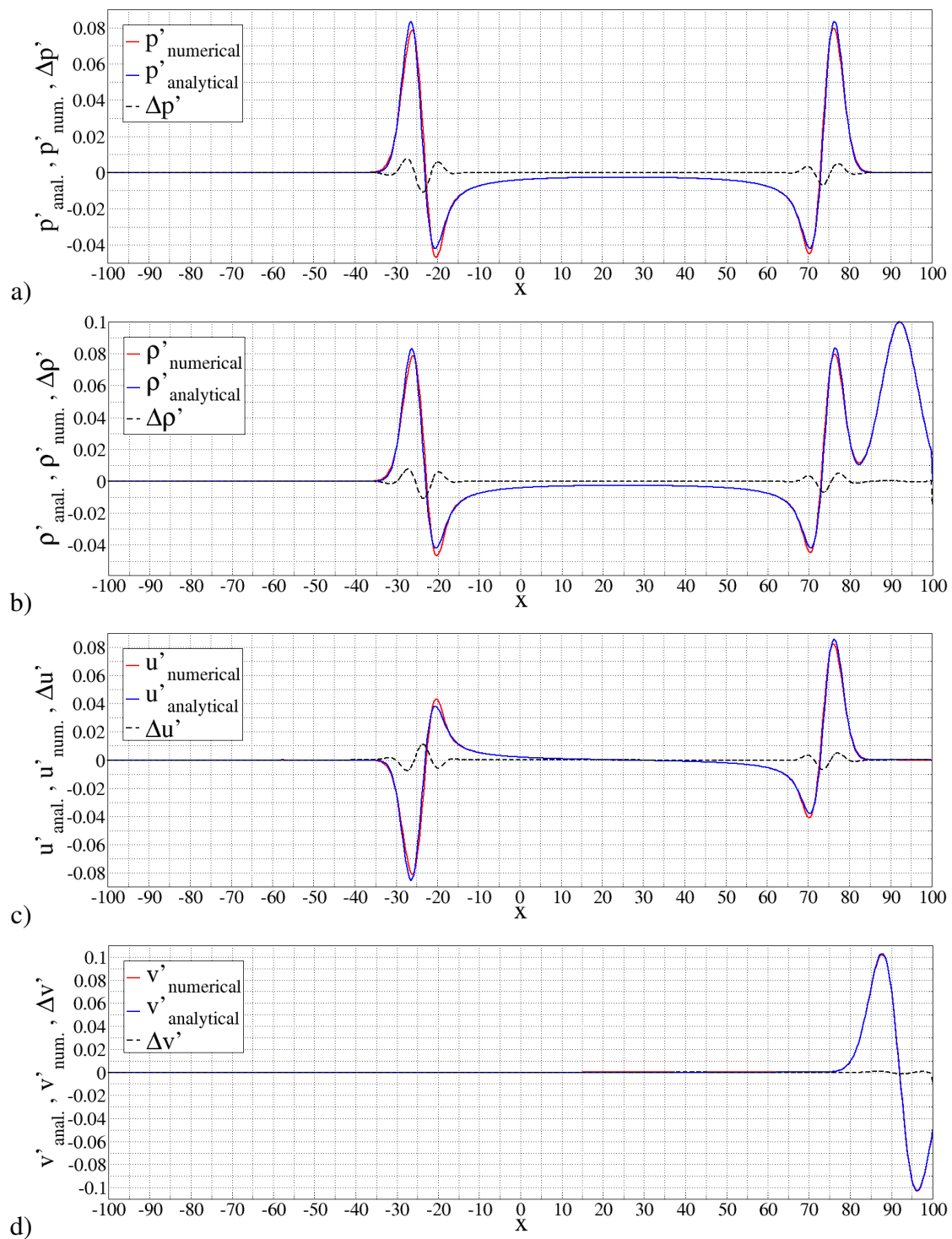
Figure 6.2.4: Acoustic variables: fluctuation of a) pressure $\hat{p}'$, b) density $\hat{\rho}'$ and velocity components c) $\hat{u}'$ and d) $\hat{v}'$ at time $\hat{t} = 50$, $y = 0$, 360 000 cell grid, HMF test case.

Figure 6.2.5: Acoustic variables: fluctuation of a) pressure $\hat{p}'$, b) density $\hat{\rho}'$ and velocity components c) $\hat{u}'$ and d) $\hat{v}'$ at time $\hat{t} = 50$, $y = 0$, 640 000 cell grid, HMF test case.
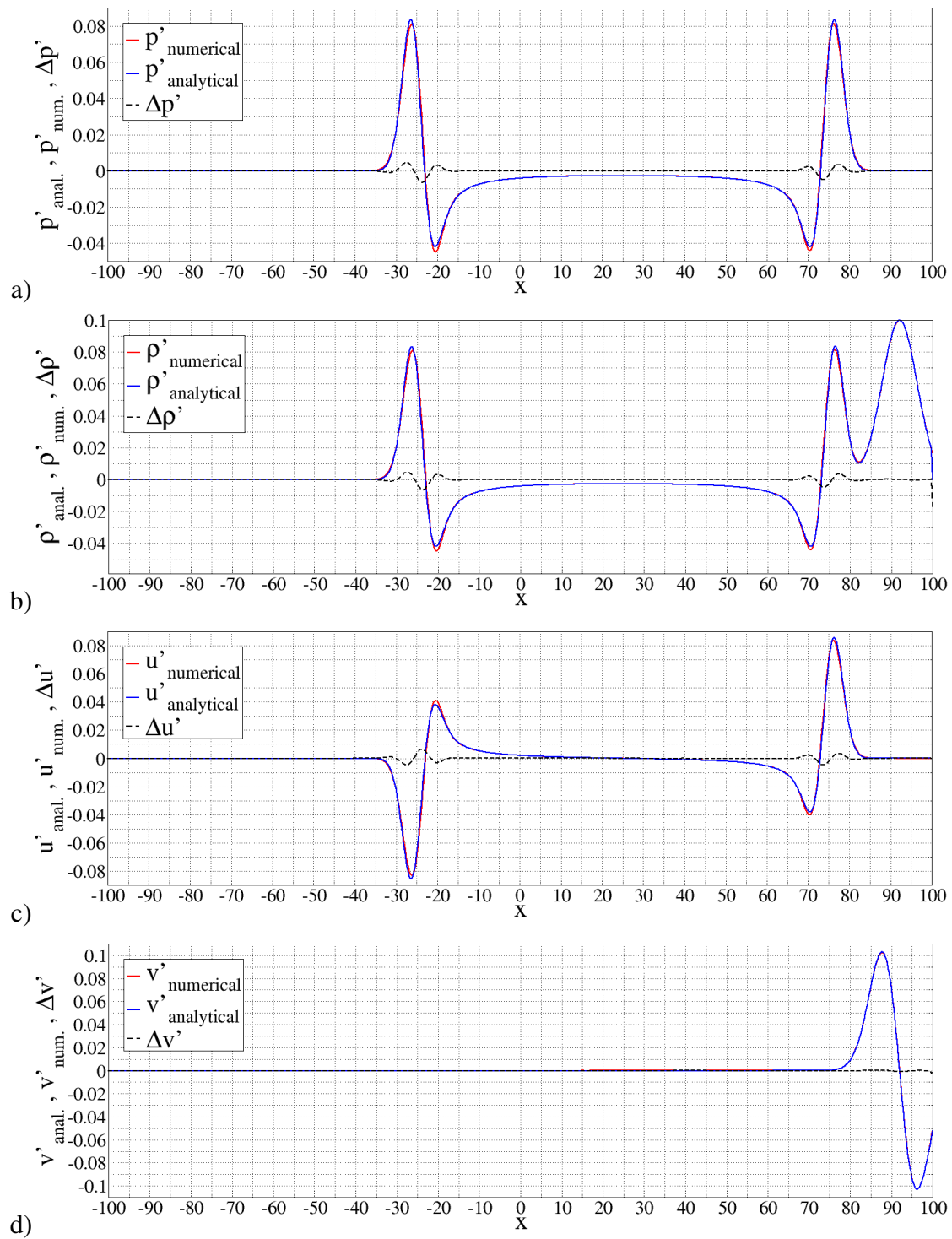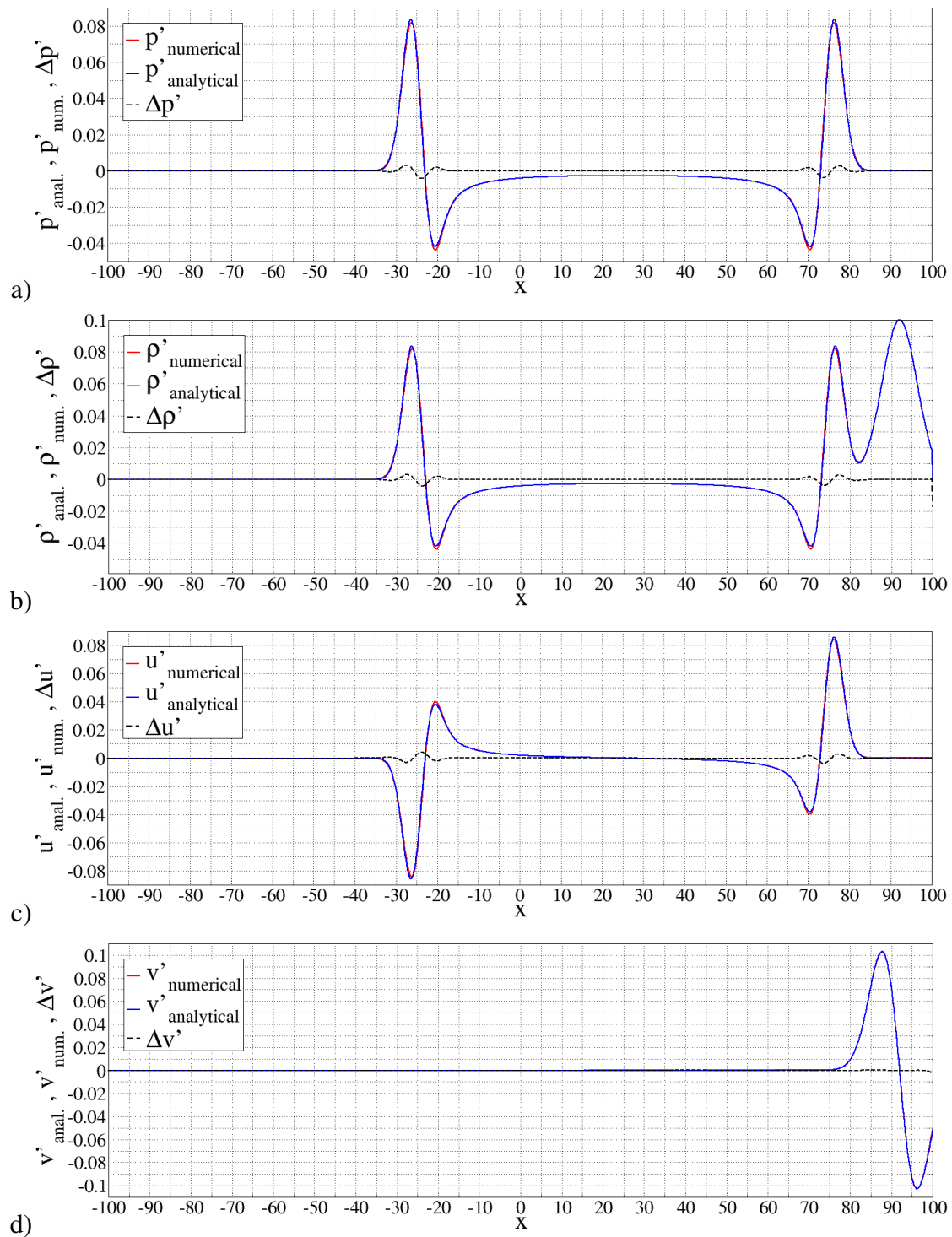
Figure 6.2.6: Acoustic variables: fluctuation of a) pressure $\hat{p}'$, b) density $\hat{\rho}'$ and velocity components c) $\hat{u}'$ and d) $\hat{v}'$ at time $\hat{t} = 50$, $y = 0$, 1 000 000 cell grid, HMF test case.

Figures 6.2.2, 6.2.3, 6.2.4, 6.2.5 and 6.2.6 show acoustic variables $\hat{p}'$, $\hat{\rho}'$, $\hat{u}'$ and $\hat{v}'$ at time $\hat{t} = 50$. Blue lines denote analytical solutions provided in Section 4.2, while red lines denote the corresponding solutions computed by the LEE code and dashed lines denote the difference between analytical and numerical solutions.

It is obvious that the differences between analytical and numerical solutions are diminished by increasing the grid resolution. The differences are caused by numerical dispersion and dissipation (together they are often called numerical diffusion). Numerical dispersion can be recognized as the waves that are not in phase with the analytical solution, whereas the numerical dissipation is recognized as the loss in the amplitude. Numerical dispersion and dissipation are especially evident in the case of the 40 000 cell grid (see fig. 6.2.2). Therefore, it can be concluded that the differences between analytical and numerical solutions describe an error due to combined effect of numerical dispersion and dissipation.

For example, looking at Figure 6.2.3 a), it can be noticed on the left wave that the difference $\Delta \hat{p}'$ consists of three half-waves. The first one is generated mostly by difference of amplitudes between numerical and analytical solutions, i.e. dissipation, as well as the third one. Second half-wave is generated in the region of highest gradients of $\hat{p}'_{analytical}$ and $\hat{p}'_{numerical.}$ and has the largest amplitude among three half-waves. Hence the small phase shift, i.e. dispersion, generates greater error than the one generated by amplitude loss, i.e. dissipation. In authors opinion, the two errors should not be compared to each other and should be analysed separately. In the following section 6.3 only the error generated by the numerical dissipation will be analysed, i.e. only amplitude values (both positive and negative) will be taken into account.

Combining the differences between analytical and numerical solutions for all grids, the Figure 6.2.7 is obtained. It can be noticed that numerical procedure gives more accurate solutions for entropy and vorticity waves compared to the radiating acoustic wave. The reason for this is in the fact that the half-width of entropy and vorticity initial pulses (equals 5) is greater than the one of the initial acoustic pulse (equals 3).
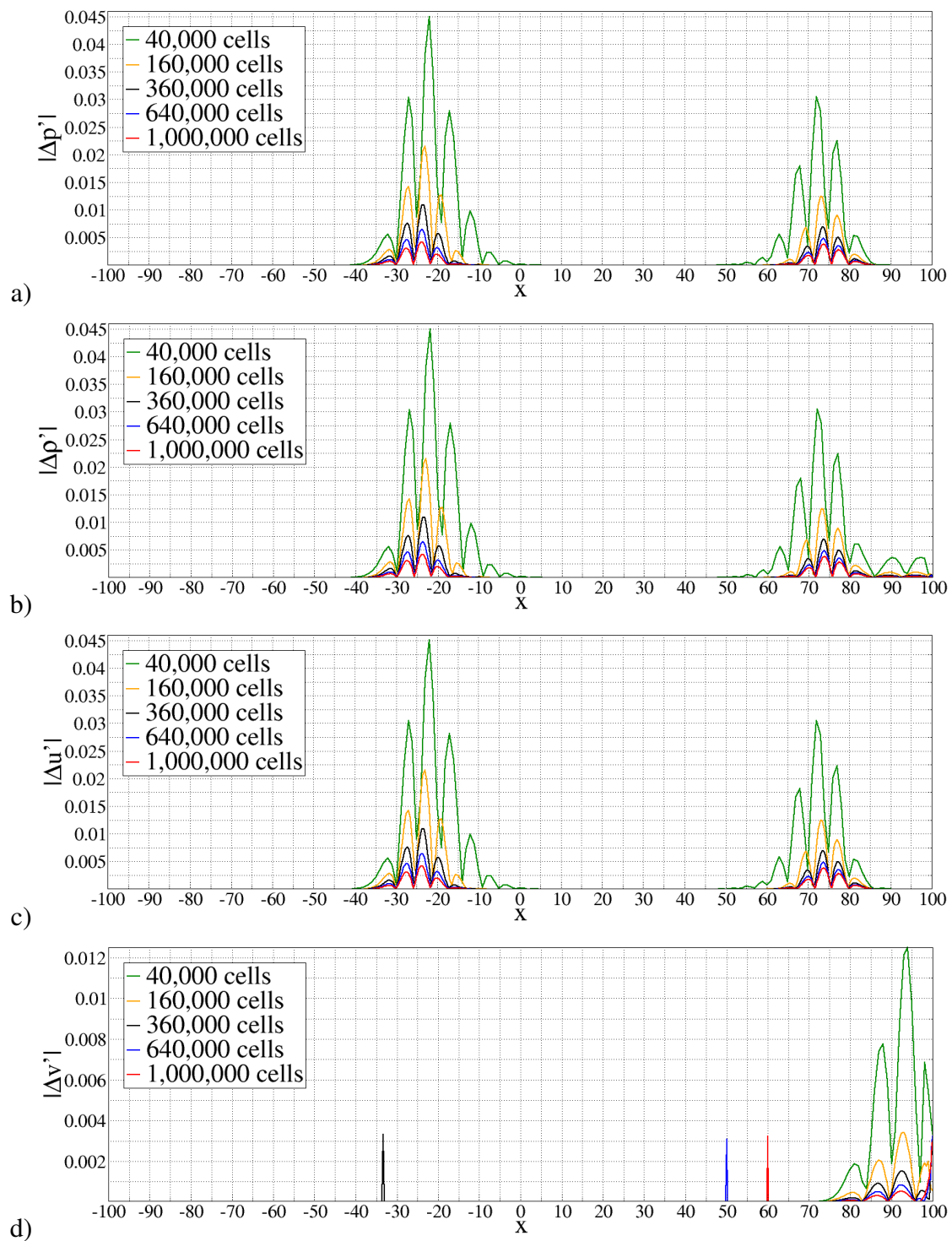
Figure 6.2.7: Numerical errors: a) $|\Delta\hat{p}'|$, b) $|\Delta\hat{\rho}'|$, c) $|\Delta\hat{u}'|$ and d) $|\Delta\hat{v}'|$ at time $\hat{t} = 50$, $y = 0$, HMF test case.

6.2.2   Test Case with Diagonal Mean Flow

Analogously to the previous subsection, a slice is defined at $x = y$ and a new, also dimensionless coordinate s, which lies at the slice $x = y$, with the same length scale, is introduced. On Figure 6.2.8 the same four acoustic variables are presented, as on Figure 6.2.1. Diagonal lines denote the slices at $x = y$ through which the acoustic fields are examined in the following figures.
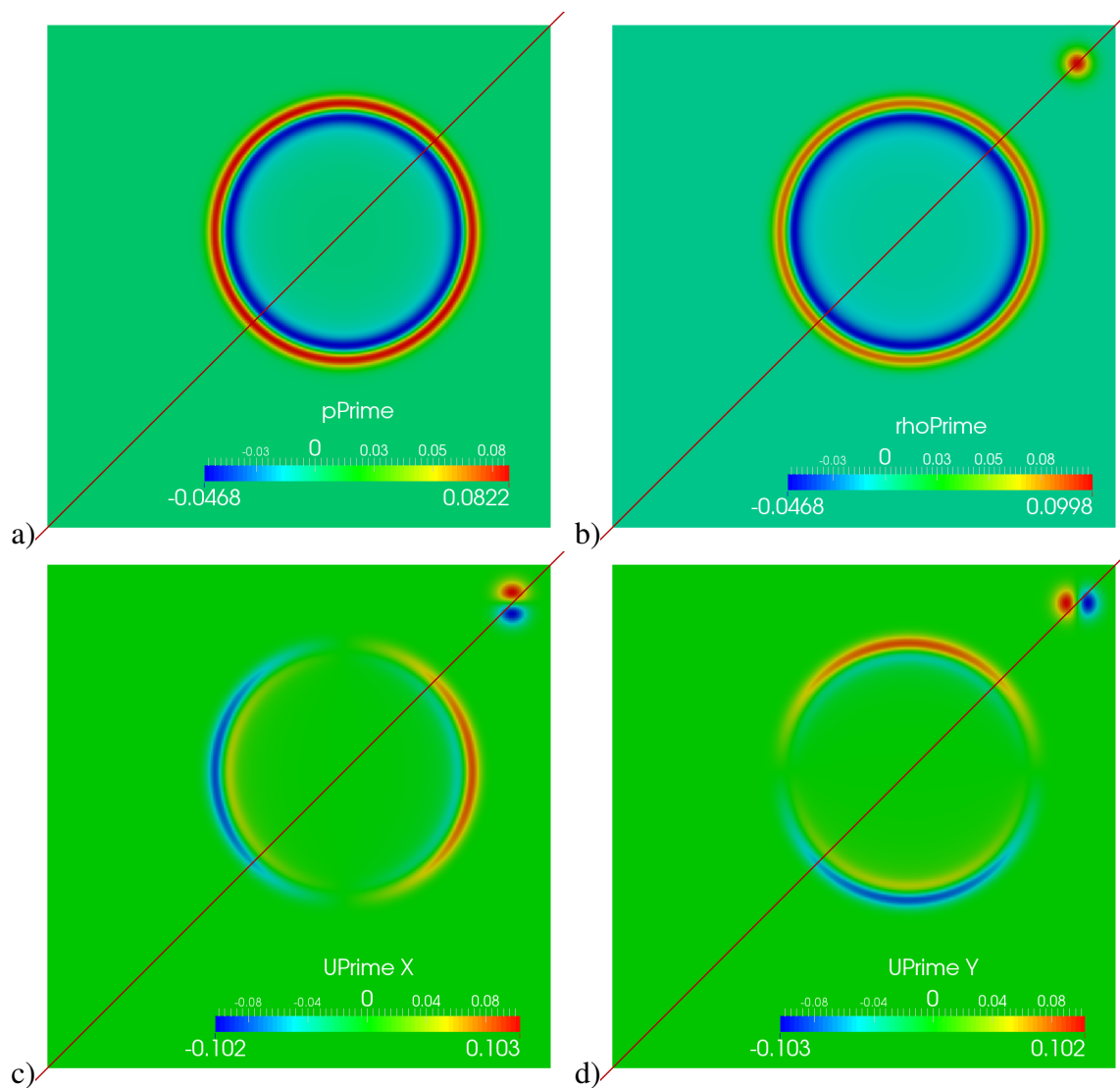
Figure 6.2.8: Acoustic fields a) $\hat{p}'$, b) $\hat{\rho}'$, c) $\hat{u}'$ and d) $\hat{v}'$ at time $\hat{t} = 50$ on the grid with 360 000 cells, DMF test case.
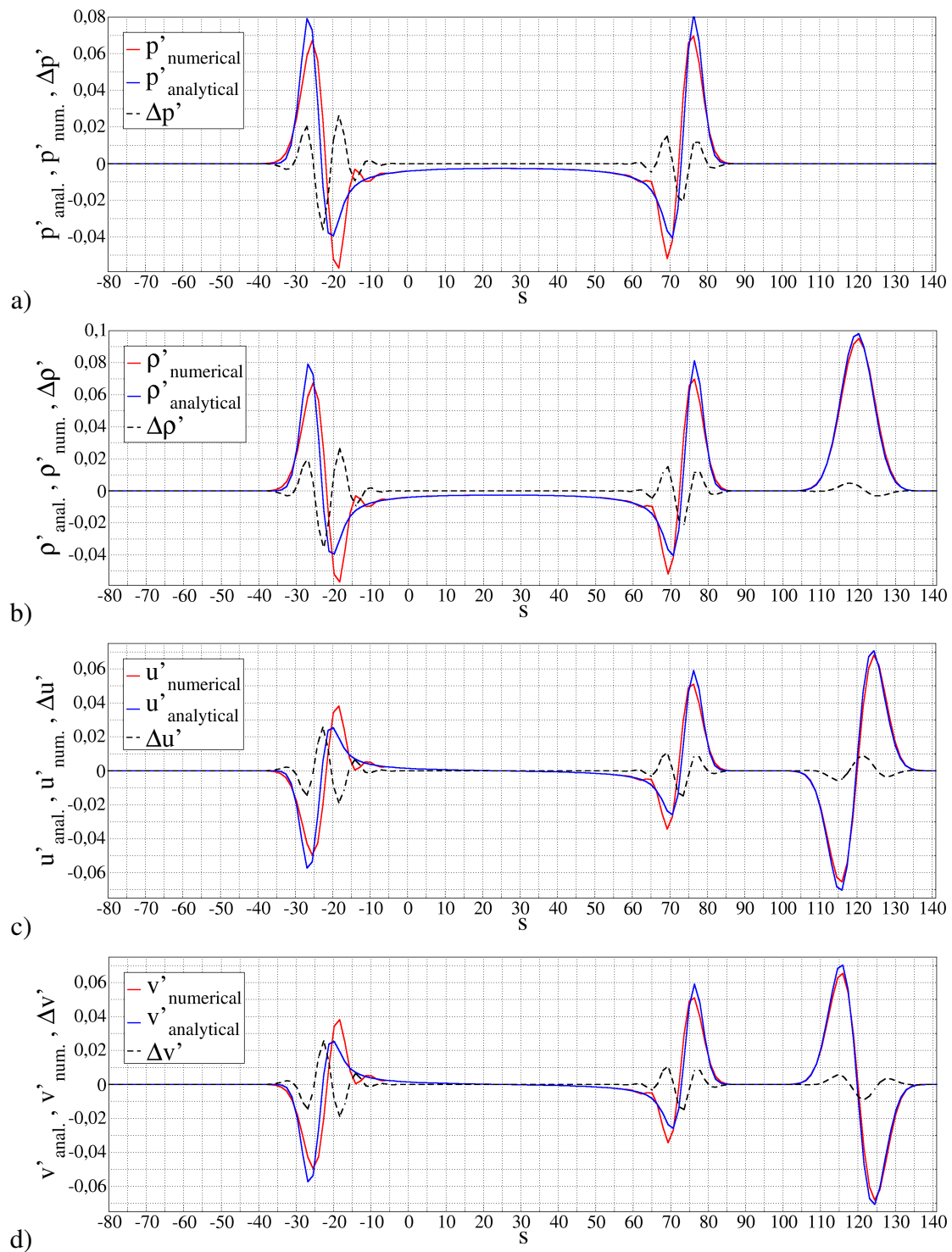
Figure 6.2.9: Acoustic variables: fluctuation of a) pressure $\hat{p}'$, b) density $\hat{\rho}'$ and velocity components c) $\hat{u}'$ and d) $\hat{v}'$ at time $\hat{t} = 50$, $x = y$, 40 000 cell grid, DMF test case.
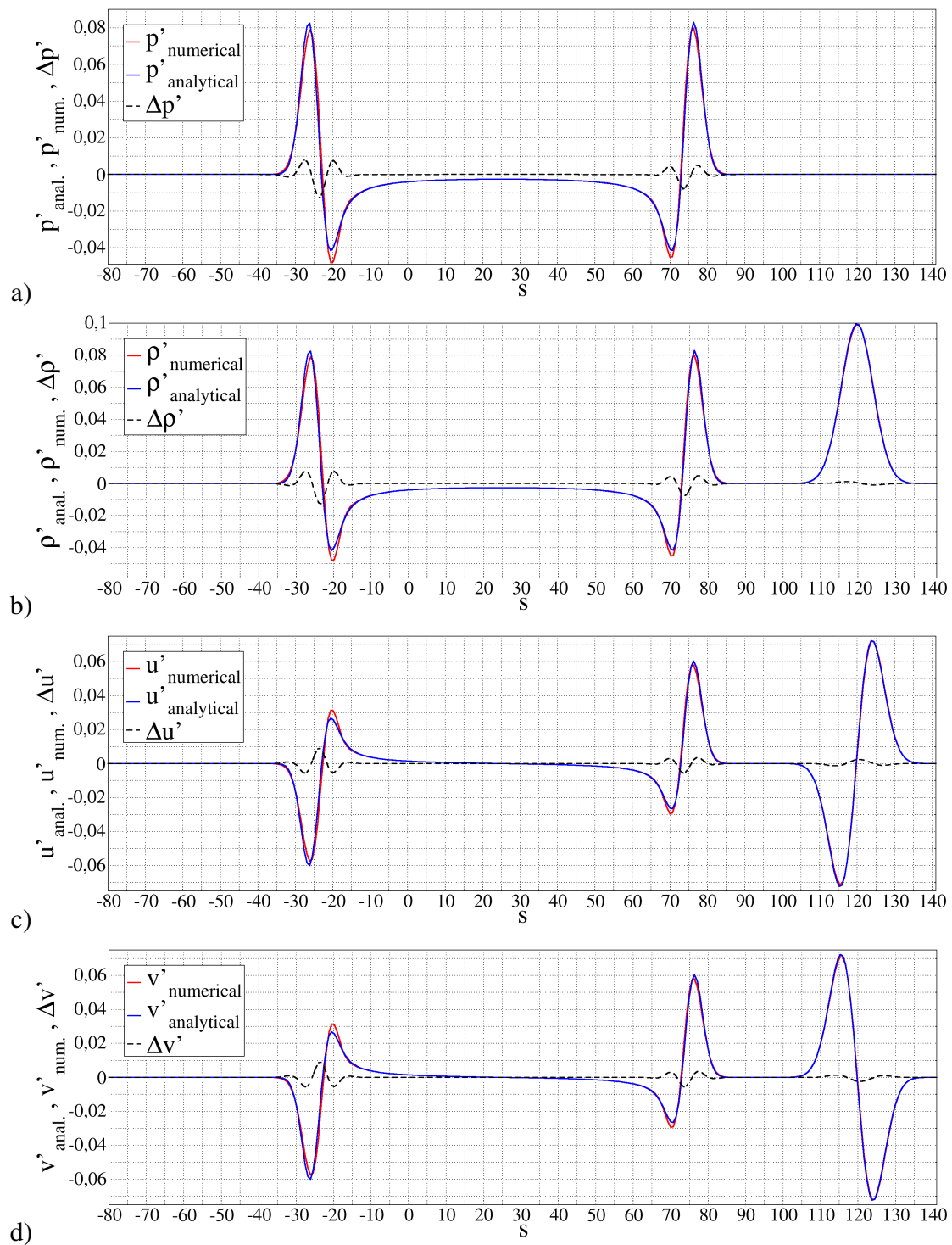
Figure 6.2.10: Acoustic variables: fluctuation of a) pressure $\hat{p}'$, b) density $\hat{\rho}'$ and velocity components c) $\hat{u}'$ and d) $\hat{v}'$ at time $\hat{t} = 50$, $x = y$, 160 000 cell grid, DMF test case.
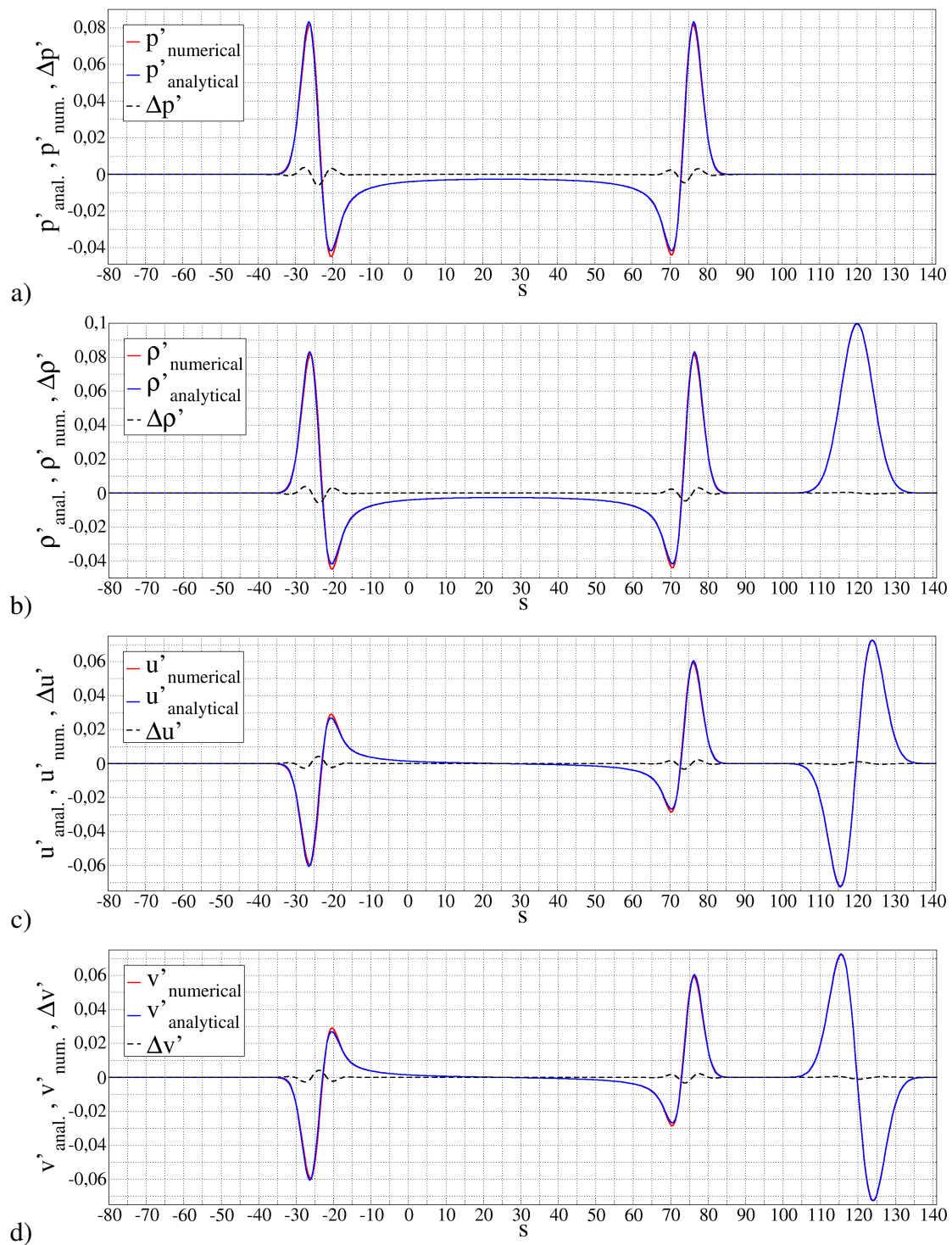
Figure 6.2.11: Acoustic variables: fluctuation of a) pressure $\hat{p}'$, b) density $\hat{\rho}'$ and velocity components c) $\hat{u}'$ and d) $\hat{v}'$ at time $\hat{t} = 50$, $x = y$, 360 000 cell grid, DMF test case.
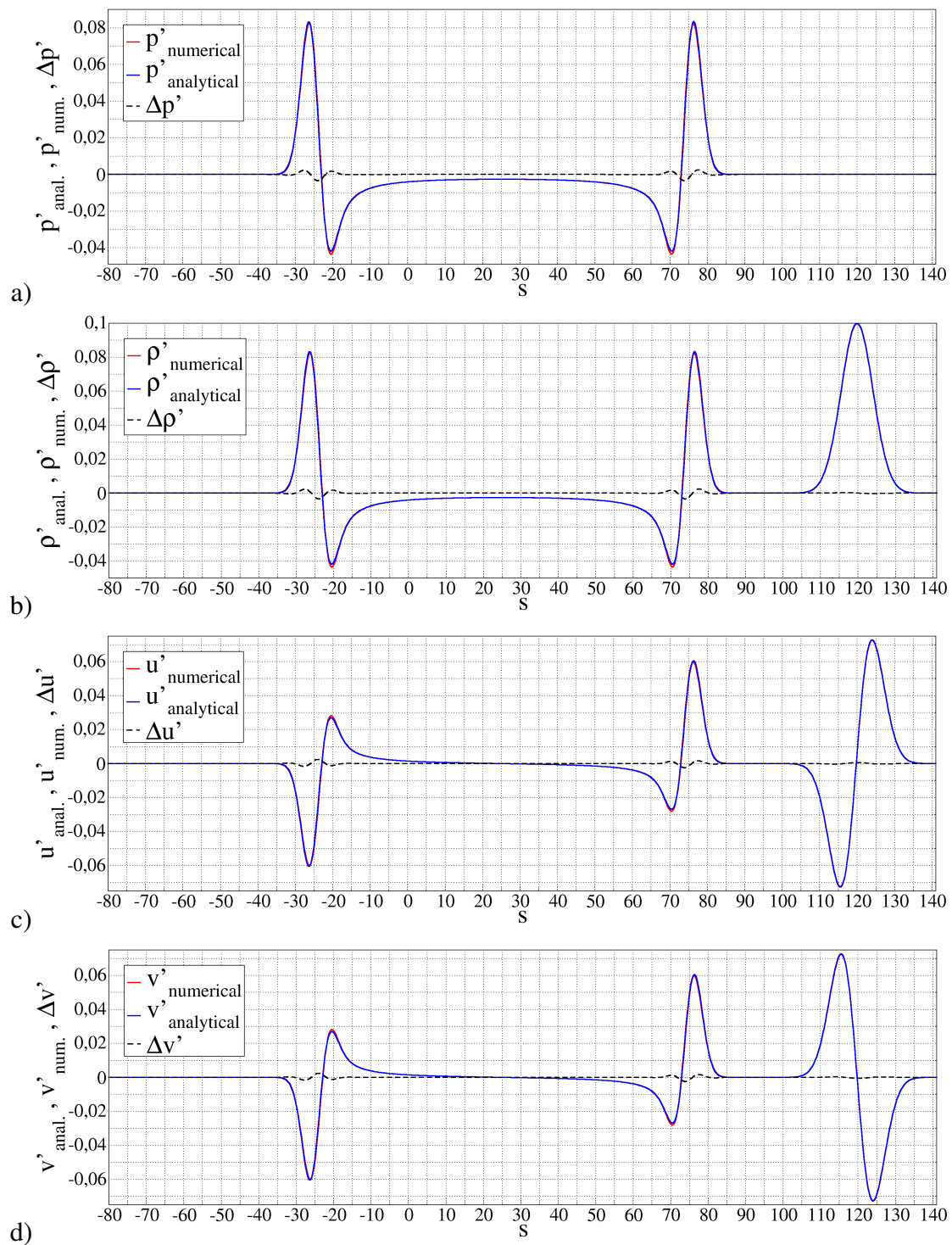
Figure 6.2.12: Acoustic variables: fluctuation of a) pressure $\hat{p}'$, b) density $\hat{\rho}'$ and velocity components c) $\hat{u}'$ and d) $\hat{v}'$ at time $\hat{t} = 50$, $x = y$, 640 000 cell grid, DMF test case.

Figure 6.2.13: Acoustic variables: fluctuation of a) pressure $\hat{p}'$, b) density $\hat{\rho}'$ and velocity components c) $\hat{u}'$ and d) $\hat{v}'$ at time $\hat{t} = 50$, $x = y$, 1 000 000 cell grid, DMF test case.

Figures 6.2.9, 6.2.10, 6.2.11, 6.2.12 and 6.2.13 show acoustic fields $\hat{p}'$, $\hat{\rho}'$, $\hat{u}'$ and $\hat{v}'$ on the slice $x = y$ for all grids. The acoustic fields have not been plotted on the entire range of the coordinate s, but only there where the waves exist, i.e. $-80 \leqslant s \leqslant 141$.

Following the analysis procedure as in previous subsection, qualitatively no difference has been observed. The only difference is noticed in the fact that the differences between analytical and numerical solutions diminish more quickly than the differences in test case with horizontal mean flow with increasing the grid resolution. This remark will be more closely examined in the Section 6.3.

6.2.3 Test Case with Reflective Wall

In this test case the dimensionless time has also been fixed at $\hat{t} = 50$ and the slice defined at $x = 25$. This slice passes through the center of the acoustic wavefront. The following figures show the pressure fluctuation field, $\hat{p}'$, and the component of velocity fluctuation field in y direction, $\hat{v}'$, both plotted at $x = 25$. Other acoustic fields are not shown because the density fluctuation field looks exactly like the pressure fluctuation field, whereas the other velocity fluctuation component is equal to zero at that slice.
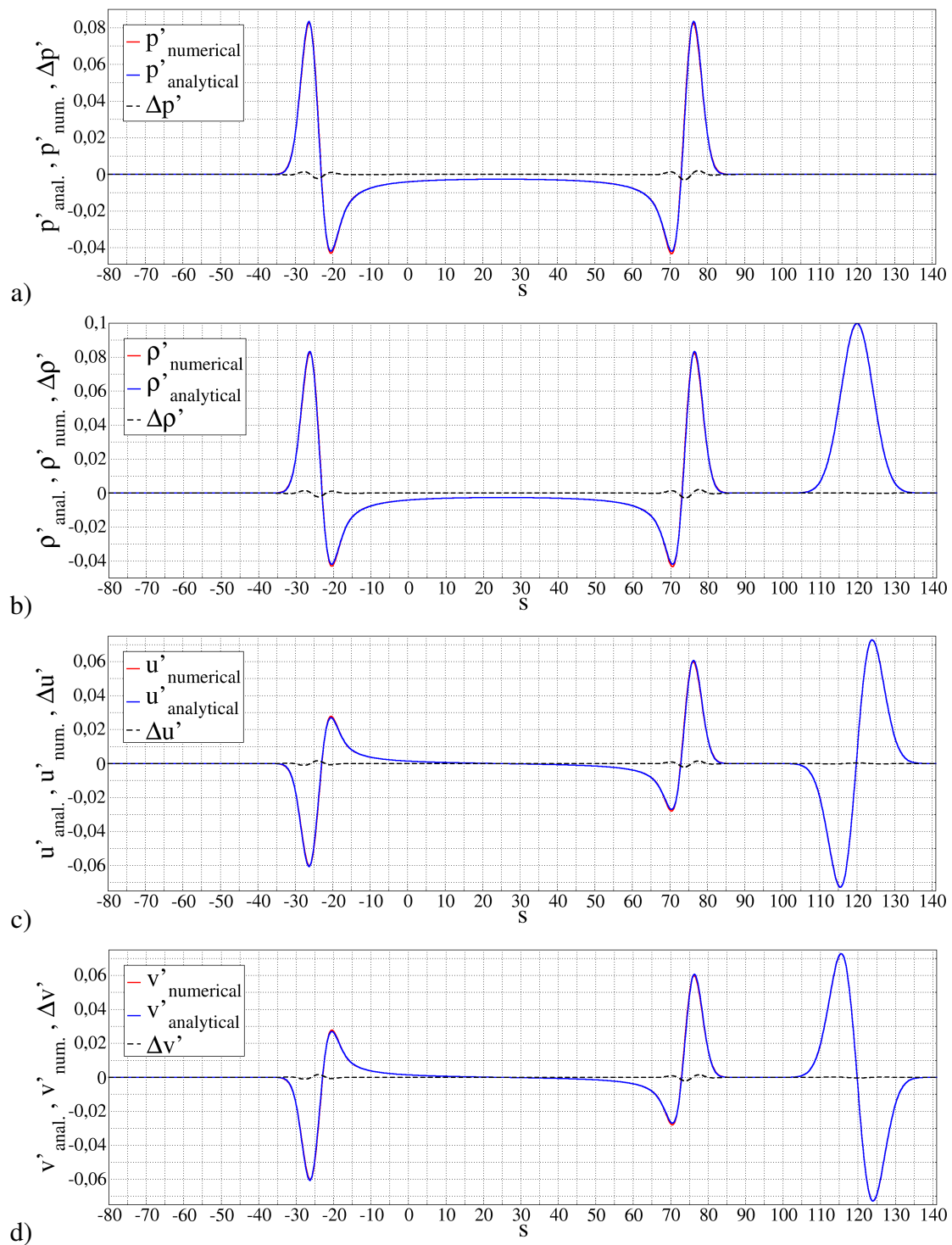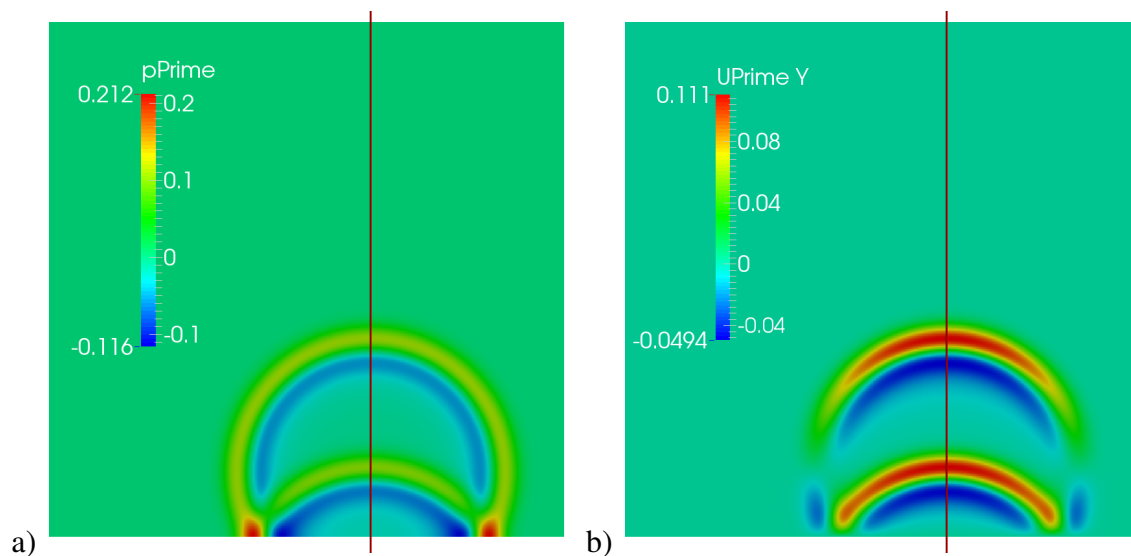

Figure 6.2.14: Acoustic fields a) $\hat{p}'$, b) $\hat{v}'$ at time $\hat{t} = 50$ on the grid with 360 000 cells, RW test case.
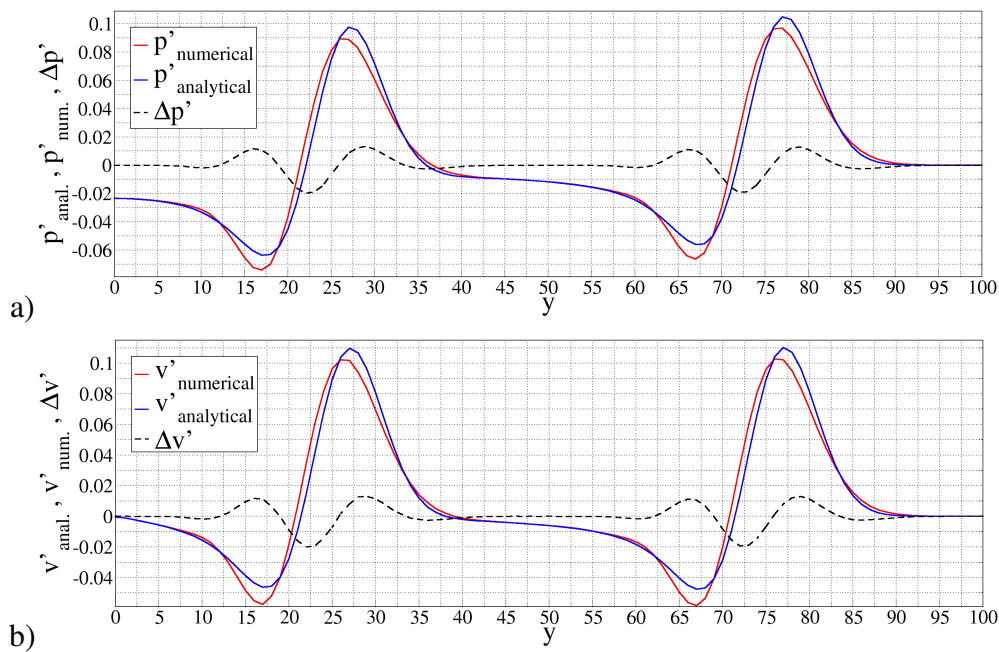
Figure 6.2.15: Acoustic variables: fluctuation of a) pressure $\hat{p}'$ and velocity component b) $\hat{v}'$ at time $\hat{t} = 50$, $x = 25$, 40 000 cell grid, RW test case.
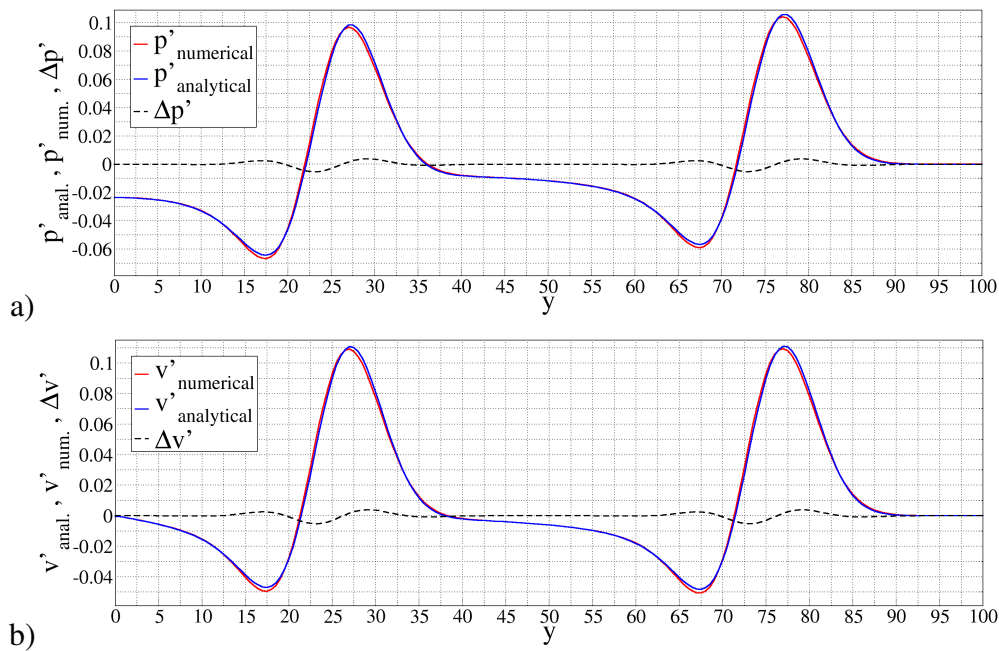
Figure 6.2.16: Acoustic variables: fluctuation of a) pressure $\hat{p}'$ and velocity component b) $\hat{v}'$ at time $\hat{t} = 50$, $x = 25$, 160 000 cell grid, RW test case.
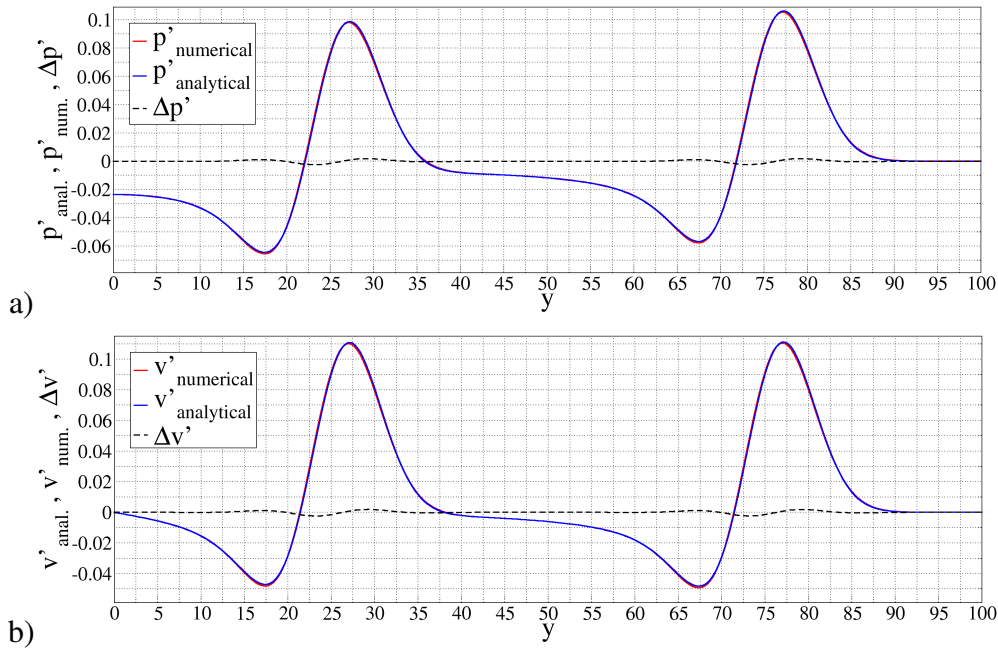
Figure 6.2.17: Acoustic variables: fluctuation of a) pressure $\hat{p}'$ and velocity component b) $\hat{v}'$ at time $\hat{t} = 50$, $x = 25$, 360 000 cell grid, RW test case.

Analysing the figures 6.2.15, 6.2.16 and 6.2.17 it can be noticed that the differences between analytical and numerical solutions diminish more quickly with grid refinement than those of test cases with horizontal and diagonal mean flow. The reason for that behaviour is in different half-width of the initial acoustic pulse than the ones of test cases HMF and DMF (this is also the case with initial vorticity and entropy pulses, see Section 6.2.1). Results for the grids with 640 000 and 1 000 000 cells are not shown here because the differences between analytical and numerical solutions for these grids are even smaller and they would not provide any additional information.

6.3   Grid Convergence Error Analysis

For test cases with horizontal and diagonal mean flow, the grid convergence analysis has been carried out for the pressure fluctuations $\hat{p}'$ in the upstream radiating acoustic wavefront, i.e. the left pressure wave on the slice at $y = 0$ (test case with horizontal mean flow) or the slice $x = y$ (test case with diagonal mean flow). This wave has been chosen because the deviation of the numerical solution from the analytical one is greater than the deviation in the upstream wavefront.

For the reflective wall test case, the grid convergence analysis has been made using $\hat{p}'$ in the reflected wave off a wall and non-reflected wave, in order to verify and validate the wave reflection. The data of $\hat{p}'$ has been extracted from the slice $x = 25$, as in the previous section.

As written in the previous section, only the error generated by the numerical dissipation will be analysed, i.e. only amplitude values (both positive and negative) will be taken into account.

6.3.1   Test Case with Horizontal Mean Flow

For the HMF test case the grid convergence analysis has been made using two reference variables: $\hat{p}'_{loc.max.}$ and $\Delta p'_{min-max}$, described in the following paragraph.

The first grid convergence analysis has been made by comparing the positive values of numerical and analytical pressure fluctuation amplitudes, $\hat{p}'_{loc.max.}$ (local maximums). The second analysis has been made by comparing the min-max values $\Delta p'_{min-max}$ (distances between negative and positive amplitudes) of numerical and analytical solutions for pressure fluctuation $\hat{p}'$.

The grid convergence analyses have been carried out for two grid combinations. The first combination involves the grids with 40 000, 160 000 and 640 000 cells, whereas the second combination involves three finest grids with resolutions of 360 000, 640 000 and 1 000 000 cells. One can notice that the grid doubling has been applied in the first combination, yielding refinement ratio $r = 2$.

Tables 6.1 and 6.2 contain values $\hat{p}'_{loc.max.}$ and $\Delta p'_{min-max}$ for the corresponding grids. The GCI_{32} is calculated using solutions for the coarse (subscript 3) and middle (subscript 2) grid, whereas the GCI_{21} is calculated using solutions for the middle (index 2) and fine (index 1) grid. The order of accuracy p_G has been calculated using the eq. (4.32) in the case of the coarse-

grid combination (Table 6.1, constant r) and using the eq. (4.31) in the case of the fine-grid combination (Table 6.2, varying r: $r_{32} = 1.333$, $r_{21} = 1.25$). For both tables the Richardson extrapolates are calculated in general form (eq. (4.29)) so the results could be comparable.

Grid name	Cell size	$\hat{p}'_{loc.max.}$	$\tilde{f}_{exact}$	$f_{anal.}$	GCI^{fine} (%)	$\frac{GCI_{32}}{r^p GCI_{21}}$	p_G
40K	1	0.05425	-		-	-	
160K	0.5	0.07256	0.08742	0.0835	$GCI_{32} = 25.62$	1.11	1.158
640K	0.25	0.08076			$GCI_{21} = 10.32$		
Grid name	Cell size	$\Delta p'_{min-max}$	$\tilde{f}_{exact}$	$f_{anal.}$	GCI^{fine} (%)	$\frac{GCI_{32}}{r^p GCI_{21}}$	p_G
40K	1	0.10517	-		-	-	
160K	0.5	0.12326	0.125907	0.1255	$GCI_{32} = 2.69$	1.019	2.965
640K	0.25	0.12557			$GCI_{21} = 0.34$		

Table 6.1: Grid convergence error analysis: coarse-grid combination, HMF test case.

| Grid name	Cell size	$\hat{p}'_{loc.max.}$	$\tilde{f}_{exact}$	$f_{anal.}$	GCI^{fine} (%)	$\frac{GCI_{32}}{r^p GCI_{21}}$	p_G
360K	0.333	0.078518	-		-	-	
640K	0.25	0.08076	0.083757	0.0835	$GCI_{32} = 4.73$	0.97	1.944
1M	0.2	0.081816			$GCI_{21} = 2.96$		
Grid name	Cell size	$\Delta p'_{min-max}$	$\tilde{f}_{exact}$	$f_{anal.}$	GCI^{fine} (%)	$\frac{GCI_{32}}{r^p GCI_{21}}$	p_G
360K	0.333	0.12545	-		-	-	
640K	0.25	0.12557	0.125724	0.1255	$GCI_{32} = 0.16$	0.938	1.969
1M	0.2	0.12562			$GCI_{21} = 0.101$		

Table 6.2: Grid convergence error analysis: fine-grid combination, HMF test case.

Figures 6.3.1 and 6.3.2 show the values $\hat{p}'_{loc.max.}$, $\Delta p'_{min-max}$, $\tilde{f}_{exact}$ (generalized Richardson extrapolates) and $f_{anal.}$ from the Tables 6.1 and 6.2, as well as the analytical solutions, where Δx denotes cell size. Note that solid or dashed lines, do not represent any data but only link the symbols that represent discrete data points, i.e. the values from tables. The solutions marked with a) refer to the coarse-grid combination, whereas the solutions marked with b) refer to the fine-grid combination. The green solid lines represent analytical solutions.

Using eq. (4.39) it is possible to examine whether the solutions are within the asymptotic range of convergence, which is reported in the column before the last one in tables 6.1 and 6.2. When the value $\frac{GCI_{32}}{r^p GCI_{21}}$ is close to one, the solutions are near the asymptotic range. The case with the greatest deviation is the one with coarse-grid combination with the reference variable $\hat{p}'_{loc.max.}$ and equals $\frac{GCI_{32}}{r^p GCI_{21}} = 1.11$. Even though the grid doubling (constant $r = 2$) was applied, the solutions are the farthest from the asymptotic range, compared to other solutions. Extrapolating the solutions (blue line on Figure 6.3.1), an approximation of the exact solution is obtained at $\Delta x \approx 0$ and deviates the most from the analytical solution in comparison with other generalized Richardson extrapolate. This could be caused because the middle grid (160K) in coarse-grid combinatin is still to coarse. Better result will show the standard Richardson extrapolate in the following text.

The Figure 6.3.2 shows that numerical solutions converge to the value that is slightly greater than the analytical solution, according to the generalized Richardson extrapolates. The fine-grid combination gives the extrapolated solution closer to the analytical value, compared to the solution of the coarse-grid combination. The solution obtained with 40K grid is not visible on the graph, due to large discrepancy of solutions.

It is possible to calculate standard Richardson extrapolates for the coarse-grid combination using (4.25), because the grid refinement ratio is $r = 2$. The Table 6.3 contains the values of standard Richardson extrapolates ($\tilde{f}_{exact}$) obtained using either $\hat{p}'_{loc.max.}$ or $\Delta p'_{min-max}$. Figures 6.3.3 and 6.3.4 show the vaules from the Table 6.3 graphically. If the generalized (blue diamond symbol) and standard (red diamond symbol) Richardson extrapolates of numerical solutions from the grids 160K and 640K are compared, it is clear that the standard extrapolate gives the value closer to the analytical solution. This is not the case with extrapolation of $\Delta p'_{min-max}$, shown in Figure 6.3.4, which could be caused by the fact that numerical solutions do not converge towards the analytical value. Standard Richardson extrapolates of numerical
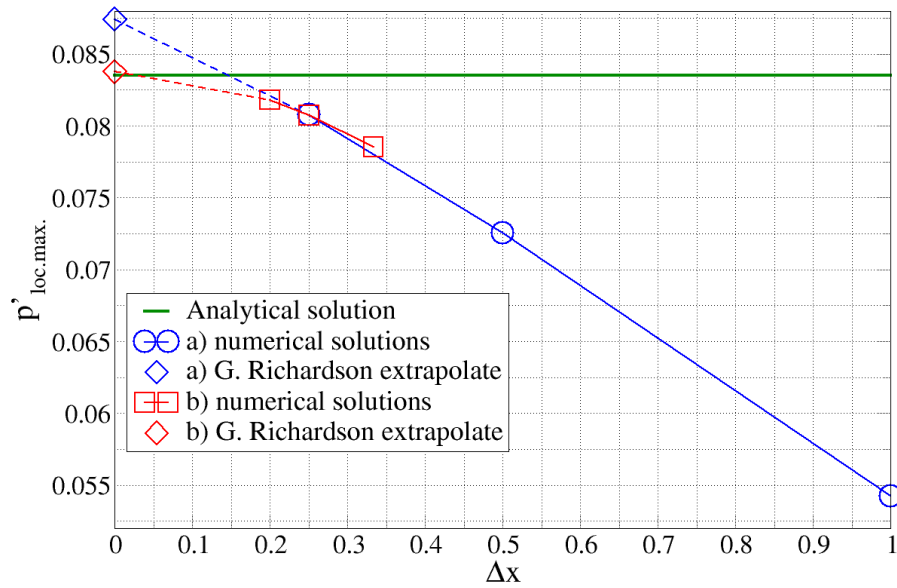
Figure 6.3.1: Grid Covergence Analysis for $\hat{p}'_{loc.max.}$; *a*) coarse-grid combination, *b*) fine-grid combination, HMF test case.
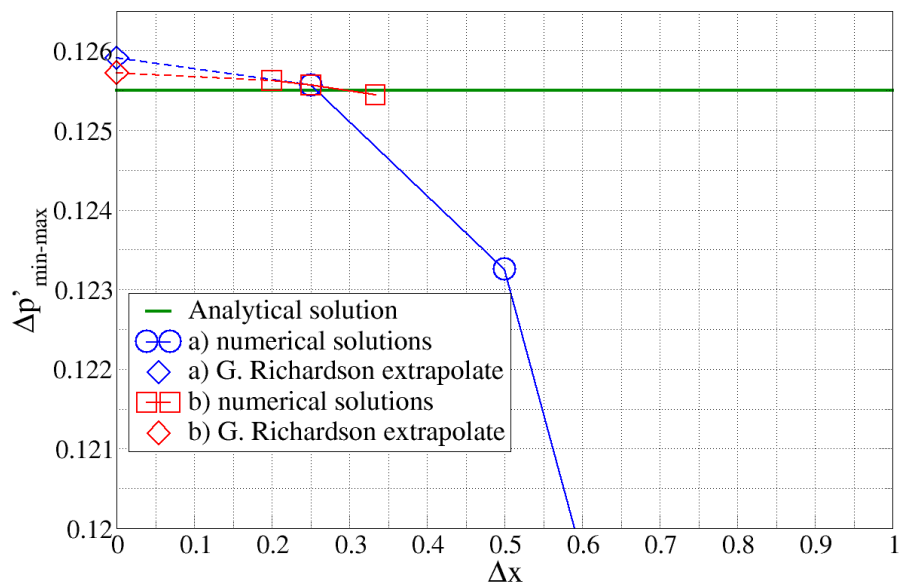
Figure 6.3.2: Grid Covergence Analysis for $\Delta p'_{min-max}$; *a*) coarse-grid combination, *b*) fine-grid combination, HMF test case.

Grid name	Cell size	$\tilde{f}_{exact}$ (using $\hat{p}'_{loc.max.}$)		$f_{anal.}$
40K	1	0.078658	-	0.0835
160K	0.5		0.083497	
640K	0.25		-	

Grid name	Cell size	$\tilde{f}_{exact}$ (using $\Delta p'_{min-max}$)		$f_{anal.}$
40K	1	0.129279	-	0.1255
160K	0.5		0.126338	
640K	0.25		-	

Table 6.3: Coarse-grid combination, standard Richardson extrapolates, HMF test case.

solutions for the grids 40K and 160K deviate the most, compared to ones obtained from finer grids.
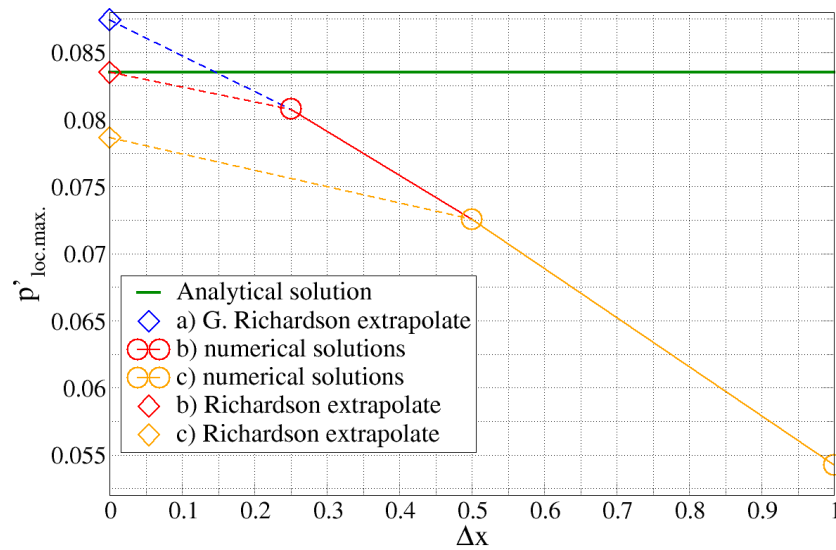
Figure 6.3.3: Grid Covergence for $\hat{p}'_{loc.max.}$, coarse-grid combination ($r = 2$), a) generalised Richardson extrapolate from middle and fine grid, b) middle and fine grid solutions and their standard Richardson extrapolate, c) coarse and middle grid solutions and their standard Richardson extrapolate, HMF test case.
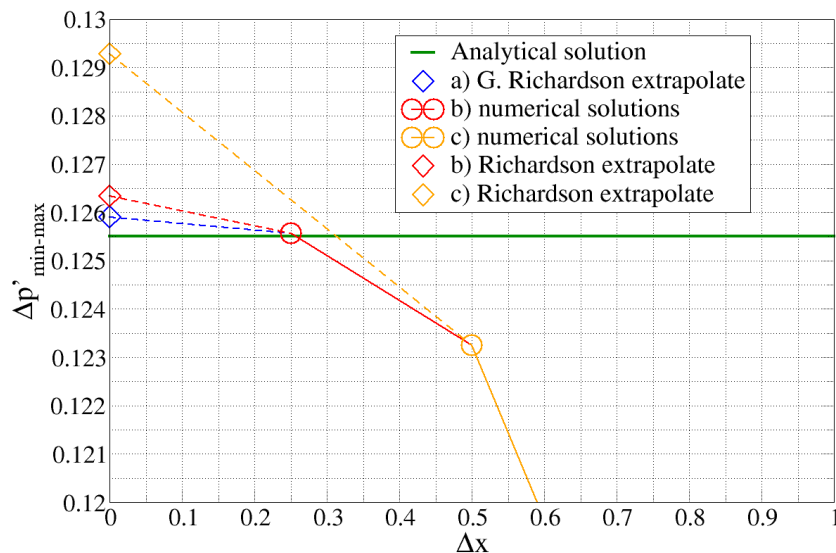
Figure 6.3.4: Grid Covergence for $\Delta p'_{min-max}$, coarse-grid combination ($r = 2$), a) generalised Richardson extrapolate from middle and fine grid, b) middle and fine grid solutions and their standard Richardson extrapolate, c) coarse and middle grid solutions and their standard Richardson extrapolate.

6.3.2   Test Case with Diagonal Mean Flow

For test cases DMF and RW the grid convergence analysis will be made only for the reference variable $\hat{p}'_{loc.max.}$ because the deviation from the analytical solution is greater than the one obtained using $\Delta p'_{min-max}$. Moreover, for the coarse-grid combination the values of $\Delta p'_{min-max}$ converge oscillatory and their examination would not give comparable results, due to different equations that would have to be used.

Taking the tables 6.4 and 6.5 into consideration, specifically their orders of accuracy, it is clear that the DMF test case (at that particular slice $x = y$) gives more accurate numerical solutions than the HMF test case (at the slice $y = 0$). Considering the fact that the solutions of test cases HMF and DMF are plotted on differently oriented slices, the results of the HMF test case have also been examined on a diagonal slice (with origin in $x = 25$, $y = 0$, i.e. center of acoustic wave). The difference between these solutions and the those of the DMF test case are negligibly small and are, therefore, not presented in Section 6.2.1. This fact implies that the difference between observed orders of accuracy for test cases HMF and DMF is not a consequence of different mean velocity direction, but of different direction of wave propagation (considering grid orientation).

As expected, the GCIs are lower compared to the corresponding grid-combination for the HMF test case. For both grid combinations the solutions are quite close to the asymptotic range of convergence. Figure 6.3.5 shows the values from tables 6.4 and 6.5 graphically.

As in previous subsection, the standard Richardson extrapolate for coarse-grid combination gives more accurate values than the generalised one. This is shown by the Table 6.6 and the Figure 6.3.6.

| Grid name	Cell size	$\hat{p}'_{loc.max.}$	$\tilde{f}_{exact}$	$f_{anal.}$	GCI^{fine} (%)	$\frac{GCI_{32}}{r^p GCI_{21}}$	p_G
40K	1	0.06717	-		-	-	
160K	0.5	0.07885		0.0835	GCI$_{32}$ = 8.32		1.689
			0.0841			1.04	
640K	0.25	0.082473			GCI$_{21}$ = 2.46		

Table 6.4: Grid convergence error analysis: coarse-grid combination, DMF test case.

Grid name	Cell size	$\hat{p}'_{loc.max.}$	$\tilde{f}_{exact}$	$f_{anal.}$	GCI^{fine} (%)	$\frac{GCI_{32}}{r^p GCI_{21}}$	p_G
360K	0.333	0.0813	-		-	-	
640K	0.25	0.08247	0.08356	0.0835	GCI$_{32}$ = 1.64	0.925	2.545
1M	0.2	0.08294			GCI$_{21}$ = 0.92		

Table 6.5: Grid convergence error analysis: fine-grid combination, DMF test case.

Grid name	Cell size	$\tilde{f}_{exact}$ (using $\hat{p}'_{loc.max.}$)	$f_{anal.}$
40K	1		-
160K	0.5	0.08274	
640K	0.25	0.08368	0.0835

Table 6.6: Grid convergence error analysis: coarse-grid combination, standard Richardson extrapolates, DMF test case.
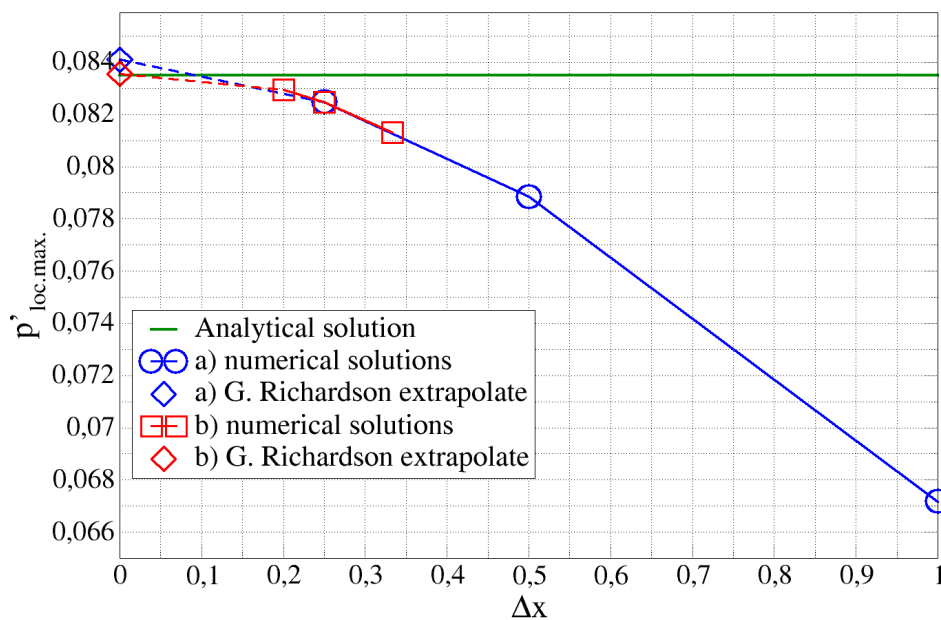
Figure 6.3.5: Grid Covergence for $\hat{p}'_{loc.max.}$, *a*) coarse-grid combination, *b*) fine-grid combination, DMF test case.
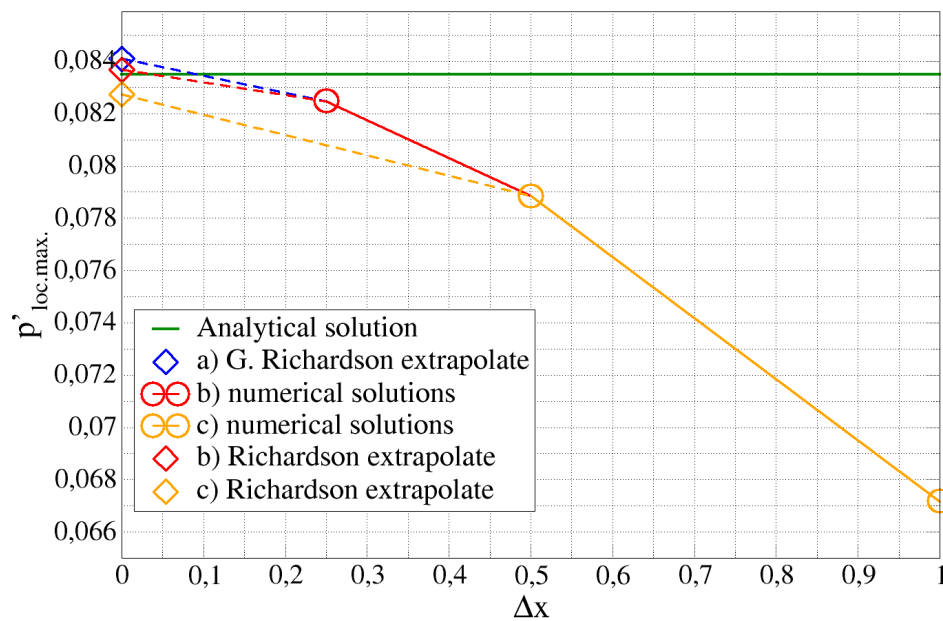
Figure 6.3.6: Grid Covergence for $\hat{p}'_{loc.max.}$, coarse-grid combination ($r = 2$), a) generalised Richardson extrapolate from middle and fine grid, b) middle and fine grid solutions and their standard Richardson extrapolate, c) coarse and middle grid solutions and their standard Richardson extrapolate, DMF test case.

6.3.3   Test Case with Reflective Wall

Reflective wall test case gives solutions which converge with the highest order of accuracy (see Table 6.7 and Table 6.8). As explained in previous section, the reason for the highest order of accuracy lies in the fact that the width of the initial acoustic pulse is larger in the RW test case, than in other cases, and the gradients of the acoustic field variables are, therefore, smaller in comparison with test cases HMF and DMF.

The $GCI_{21} = 0.45\%$ is the lowest among the GCIs of all test cases obtained using $\hat{p}'_{loc.max.}$. Therefore the fine-grid combination has not been analysed. $\frac{GCI_{32}}{r^p GCI_{21}}$ shows that the solutions are well within the asymptotic range. Table 6.9 and Figure 6.3.7 show that the standard Richardson extrapolate gives more accurate values than the generalised extrapolate, as is the case with test cases HMF and DMF.

Comparing the GCI values and the orders of accuracy between reflected and non-reflected wave (tables 6.7 and 6.8), it is obvious the accuracy of the reflected wave has not been lost.

| Grid name	Cell size	$\hat{p}'_{loc.max.}$	$\tilde{f}_{exact}$	$f_{anal.}$	GCI^{fine} (%)	$\frac{GCI_{32}}{r^p GCI_{21}}$	p_G
40K	1	0.09691	-		-	-	
160K	0.5	0.10429	0.10633	0.1064	$GCI_{32} = 2.45$	1.015	2.205
640K	0.25	0.10589			$GCI_{21} = 0.52$		

Table 6.7: Grid convergence error analysis: coarse-grid combination, non-reflected wave, RW test case.

Grid name	Cell size	$\hat{p}'_{loc.max.}$	$\tilde{f}_{exact}$	$f_{anal.}$	GCI^{fine} (%)	$\frac{GCI_{32}}{r^p GCI_{21}}$	p_G
40K	1	0.08836	-		-	-	
160K	0.5	0.09691	0.09884	0.0989	GCI$_{32}$ = 2.49	1.016	2.439
640K	0.25	0.098484			GCI$_{21}$ = 0.45		

Table 6.8: Grid convergence error analysis: coarse-grid combination, reflected wave, RW test case.

Grid name	Cell size	$\tilde{f}_{exact}$ (using $\hat{p}'_{loc.max.}$)	$f_{anal.}$
40K	1	-	
160K	0.5	0.09976	0.0989
640K	0.25	0.09901	
		-	

Table 6.9: Grid convergence error analysis: coarse-grid combination, standard Richardson extrapolates, RW test case.
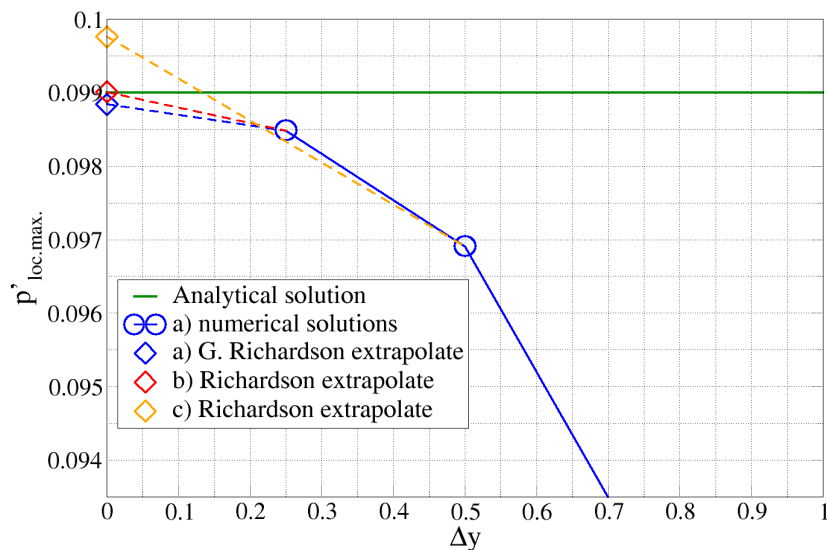
Figure 6.3.7: Grid Covergence for $\hat{p}'_{loc.max.}$, coarse-grid combination ($r = 2$), a) numerical solutions and generalised Richardson extrapolate from middle and fine grid, b) standard Richardson extrapolate for middle and fine grid solutions, c) standard Richardson extrapolate for coarse and middle grid solutions, RW test case.

6.4 Simulation of Noise Generated by a Mixing Layer

Following the SNGR procedure (described in Section 3.4), but in a simplified form, the simulation of a 2D mixing layer has been performed unsuccessfully, because it was unstable. The first subsection gives the geometry of computational domain, as well as the computational setup for the RANS simulation. In the second subsection the RANS solution and calculated fields of synthesized turbulent velocity and acoustic source are shown.

6.4.1 Geometry & Computational Setup

For this simulation the 2D rectangular domain was used, with dimensions 6×6 m. Geometry and boundary condition for the velocity are taken from the work of Billson et al. [24].

Figure 6.4.1 shows the computational domain with the inlet boundary condition for the mean velocity $\bar{u}$. At inlet boundary, mean velocity takes value U_1 in upper half of domain and corresponds to Mach number $M = 0.5$, and value U_2 in lower half of domain and corresponds to $M = 0.25$, representing as shear layer at $y = 0$. The velocity profile is defined as

$$U(y) = \frac{U_1 + U_2}{2} + \frac{U_1 - U_2}{2} \tanh\left(\frac{2y}{\delta_\omega(0)}\right), \tag{6.1}$$

where $\delta_\omega(0) = 0.02$ m is the initial shear layer thickness.

Figure 6.4.2 shows the grid used in the RANS simulation.

6.4.2 Synthesized Turbulence & Acoustic Sources

Figure 6.4.3 shows the mean velocity field obtained with RANS simulation.

The synthesized turbulent velocity field has been calculated in a simplified form:

$$u_t = \sqrt{\frac{2}{3}k}\mathbf{R}, \tag{6.2}$$

where u_t denotes synthesized turbulent velocity field, k turbulent kinetic energy and $\mathbf{R}$ the random vector, whose magnitude is $|\mathbf{R}| = 1$.

The third step of the SNGR method is to compute the non-homogeneous LEEs with source terms. In the case of LEEs used in this thesis, in the momentum equation (3.27) a single source term is introduced on the right-hand side:

$$S_{acoustic} = -\frac{\partial}{\partial x_j}\left(\bar{\rho} u'_{ti} u'_{tj} - \overline{\rho u'_{ti} u'_{tj}}\right), \tag{6.3}$$
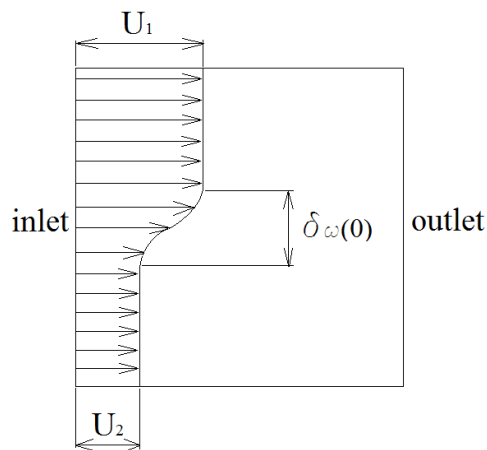
Figure 6.4.1: Computational domain with the velocity profile at inlet boundary.
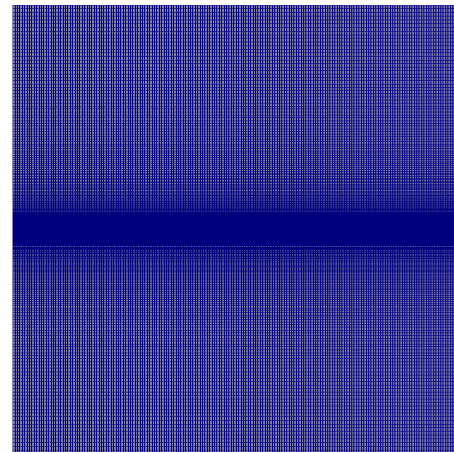
Figure 6.4.2: Finite volume grid with 114 944 cells.
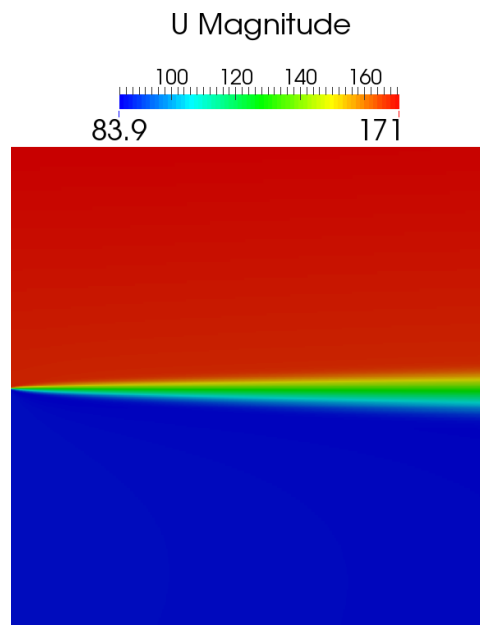
Figure 6.4.3: RANS solution of the mixing layer simulation (magnitude of the mean velocity $\bar{u}$ is shown).

as described in [24].

Figure 6.4.4 (a) shows the synthesized turbulent velocity field with random directions of velocities, whereas (b) shows the acoustic source field (6.3) calculated using turbulent velocity field.

Figure 6.4.4: (a) Synthesised turbulent velocity field with random directions, (b) acoustic source field $S_{acoustic}$.
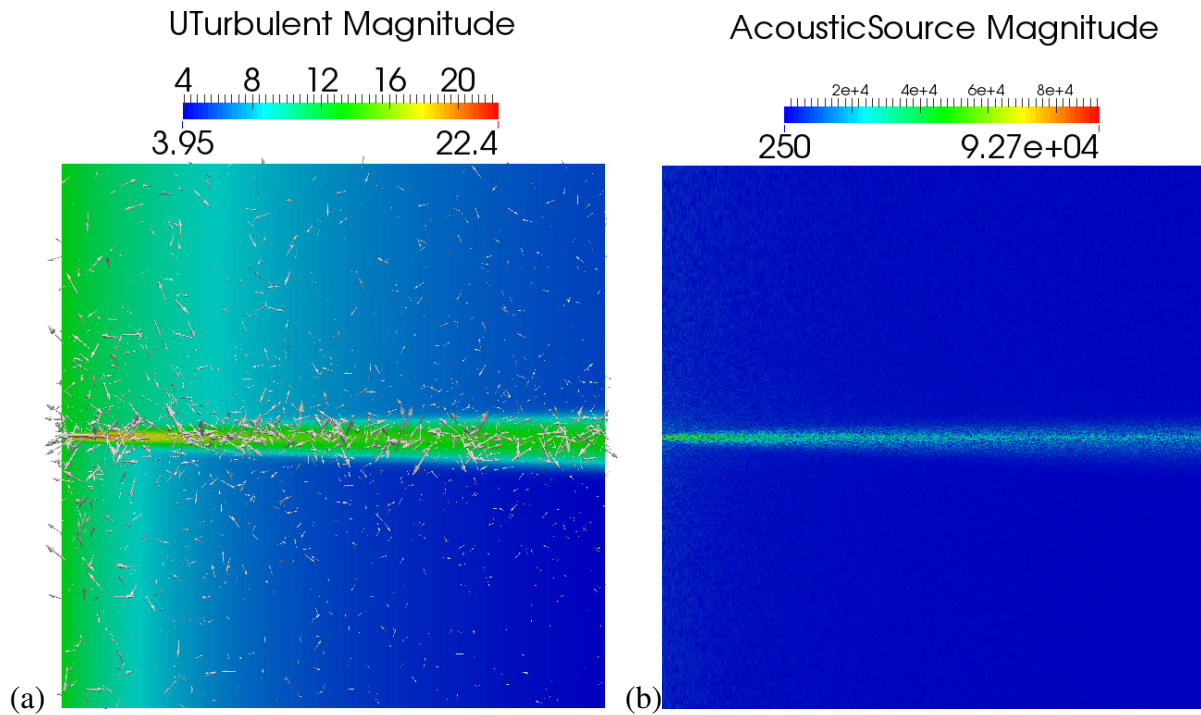
The acoustic solution obtained by the linearised Euler equations with the source term is not presented here because the simulation is unstable and the solutions diverge very quickly. This is caused by large magnitude of the acoustic source field, which appears to be unphysical and can be seen in the scale range in Figure 6.4.4 (b).

In the author's opinion, the most important role in generating unphysical source terms plays the rough method for calculating the turbulent velocity field, Equation (6.2). Another reason for generating unphysical acoustic source field could be a potential bug in the part of the code, which contains the non-homogeneous mean flow terms of the LEEs.

Chapter 7

Conclusion

In this thesis the implementation, verification and validation of the linearised Euler equations (LEEs), which govern the propagation of acoustic waves, were conducted. The LEEs were solved with Finite Volume Method (FVM), by using OpenFOAM-extend C++ software environment. The implemented system of LEEs is in the conservative form, which is suitable for finite volume discretisation.

Verification and validation of the LEE solver were conducted by using three test cases, given in [2] as Problems 1 and 2 in Category 3, and Problem 1 in Category 4. Validation was conducted with respect to analytical solutions, which are also provided in [2]. The test cases consist of the initial distribution of acoustic quantities, which represent the initial value problem, that needs to be solved numerically by the LEEs. By solving the LEEs and by comparing solutions to analytical ones, the propagation of the acoustic wave, as well as the wall and non-reflecting boundary conditions were verified and validated. The grid convergence study for all test cases was also conducted.

Results of the test cases were compared considering different time instants and different grid resolutions. Until the time when the acoustic, entropy and vorticity waves reach the open boundaries, the solutions of all field variables are in accordance with analytical solutions. Grid convergence error analysis has shown that the solutions of acoustic field variables converge towards the asymptotic numerical solutions, which are observed to be close to analytical solutions. It is concluded that the difference between observed orders of accuracy for test cases 1 and 2 is not a consequence of different mean velocity direction, but of different direction of wave propagation, if one considers the grid orientation.

For the test case 3, which examines the wall boundary conditions, the observed order of accuracy is highest among all test cases. It is, therefore, concluded that the initial distribution width of field variables with respect to available grid resolution plays an important role in numerical prediction of the acoustic field. Initial pulse width for the test case 3 was largest, compared to other test cases, so the observed order of accuracy was, accordingly, the highest. Considering the fact that both reflected and non-reflected were examined, it is concluded that the numerical prediction of the wave reflected off a wall is as accurate as the prediction of a non-reflected wave.

Comparing the acoustic fields for different time instants on the finest grid (1 000 000 cells), the solutions were presented both before and after the acoustic, entropy and vorticity waves reach the open boundary. After the waves leave the domain, a certain amount of the waves is reflected back and contaminates the solution. After several reflections, spurious waves grow in their amplitude due to their superposition. The spurious reflections occur because an inadequate von Neumann boundary condition was used, in the absence of a better one. Implementation of a better boundary condition, such as one of those presented in Section 3.3, remains a task for the future research.

The simulation of noise generated by the mixing layer was unsuccessfully conducted, due to its instability. In author's opinion, the reason could lie in rough method of predicting the turbulent velocity field, or in a potential bug in the part of the code, which is related to the non-homogeneous mean flow effects.

Finally, one can conclude that the implementation of the linearised Euler equations was successful. Results of the three test cases prove that the acoustic wave propagation in an uniform media can be accurately computed with the implemented solver, as well as the validity of the wall boundary condition.

Regarding the future research and the continuation to this thesis, the non-reflecting boundary condition should be implemented and tested in order to avoid the contamination of the solution by the spurious waves. A better method for the synthesis of the turbulent velocity field from RANS and the subgrid portion of LES, as well as its time dependence, should also be implemented and validated.

Bibliography

[1] C.A. Wagner, T. Hüttl, P. Sagaut: Large-Eddy Simulation for Acoustics, Cambridge University Press, 2007

[2] J.C. Hardin, J.R. Ristocelli, C.K.W. Tam: ICASE/LaRC Workshop on Benchmark Problems in Computational Aeroacoustics (CAA), National Aeronautics and Space Administration, Langley Research Center, 1995

[3] M.J. Lighthill: On Sound Generated Aerodynamically, I. General Theory, Proceedings of the Royal Society of London, Series A: Mathematical and Physical Sciences, Vol. A 211, pp. 564-587., 1952

[4] J.E. Ffowcs-Williams, D.L. Hawkings: Sound generation by turbulence and surfaces in arbitrary motion. Philos. Trans. R. Soc. Lond., Ser. A 264, 321-342, 1969

[5] P.G. Tucker: Unsteady Computational Fluid Dynamics in Aeronautics, Springer, 2014.

[6] C.P.A. Blom: Discontinuous Galerkin Method on Tetrahedral Elements for Aeroacoustics, University of Twente, Enschede, The Netherlands, 2003

[7] P.L. Johnson, J.M. Pent, H. Jasak, J.E. Portillo: Application of a Riemann Solver Unstructured Finite Volume Method to Combustion Instabilities, Journal of Propulsion and Power, Vol. 31 Issue: 3, pp.937-950, 2015

[8] A. Bayliss, E. Turkel: Far-field boundary condition for compressible flows, Journal of Computational Physics, 48:182-199, 1982

[9] F.Q. Hu, H.L. Atkins: A Discrete Analysis of Non-reflecting Boundary Conditions for Discontinuous Galerkin Method, AIAA Paper 2003-3301, 2003

[10] M.R. Visbal, D.V. Gaitonde: Very high-order spatially implicit schemes for computational acoustics on curvilinear meshes, Journal of Computational Acoustics, 9(4): 1259-1286, 2001

[11] J.P., Berenger: A perfectly matched layer for the absorption of electromagnetic waves, Journal of Computational Physics, 114:185-200, 1994

[12] F.Q. Hu: A stable, perfectly matched layer for linearized Euler equations in unsplit physical variables, Journal of Computational Physics, 173:455-480, 2001

[13] R.H. Kraichnan: Diffusion by a random velocity field, Journal of Computational Physics, 13(1):22-31, 1970

[14] C. Bailly, P. Lafon, S.M. Candel: A stochastic approach to compute noise generation and radiation of free turbulent flows, AIAA Paper 99-1872, 1999

[15] M. Billson: Computational Techniques for Turbulence Generated Noise, Thesis for the Degree of Doctor of Philosophy, Göteborg, Sweden, 2004.

[16] H. Jasak: Error Analysis and Estimation for the Finite Volume Method with Application to Fluid Flows, Degree of Doctor of Philosophy, Imperial College of Science, Technology and Medicine, London, June 1996

[17] J.H. Ferzinger, M. Perić: Computational Methods for Fluid Dynamics, Springer, Germany, 1997

[18] C.K.W. Tam, J.C.Webb: Dispersion-Relation-Preserving finite difference schemes for computational acoustics, Journal of Computational Physics, Vol. 107, pp. 262-281, 1993

[19] P.J. Roache: Perspective: A Method for Uniform Reporting of Grid Refinement Studies, Journal of Fluids Engineering, September 1994, Vol. 116, pp. 405-413

[20] L.F. Richardson: The Approximate Arithmetical Solution by Finite Differences of Physical Problems Involving Differential Equations with an Application to the Stresses in a Masonry Dam, Transactions of the Royal Society of London, Series A, Vol. 210, 1908, pp. 307-357.

[21] L.F. Richardson: The Deferred Approach to the Limit, Transactions of the Royal Society of London, Series A, Vol. 226, 1927, pp. 229-361.

[22] C.J. Roy: Grid Convergence Error Analysis for Mixed-Order Numerical Schemes, AIAA Journal Vol. 41, No. 4, April 2003, pp. 595-604.

[23] P.J. Roache: Quantification of Uncertainty in Computational Fluid Dynamics, Annual Review of Fluid Mechanics 1997. 29:123-60

[24] M. Billson, L.E. Eriksson, L. Davidson: Acoustic Source Terms for the Linearized Euler Equations in Conservative Form, AIAA Journal, April 2005, Vol. 43, No. 4, pp. 752-759

[25] `http://cfd.direct/openfoam/user-guide/fvschemes/`, 2016.

[26] `http://www.grc.nasa.gov/WWW/wind/valid/tutorial/spatconv.html`, 2016.

[27] `http://www.extend-project.de/`, 2016

[28] `http://www.drhodum.com/html/waves/sound.html`, 2016

[29] `http://www.diracdelta.co.uk/`, 2016

[30] `http://www.math.univ-montp2.fr/~mendez/PAPIERS/Mendez_IJA2013.pdf`, 2016